Titre: Title:	Additive Manufacturing of Complex Geometries using Continuous Fiber-Reinforced Thermoplastic Composites
Auteur: Author:	Mathieu Verville
Date:	2025
Type:	Mémoire ou thèse / Dissertation or Thesis
Référence: Citation:	Verville, M. (2025). Additive Manufacturing of Complex Geometries using Continuous Fiber-Reinforced Thermoplastic Composites [Mémoire de maîtrise, Polytechnique Montréal]. PolyPublie. https://publications.polymtl.ca/70337/

URL de PolyPublie: PolyPublie URL:	https://publications.polymtl.ca/70337/
Directeurs de recherche: Advisors:	Daniel Therriault
Programme: Program:	Génie mécanique

POLYTECHNIQUE MONTRÉAL
affiliée à l'Université de Montréal

Additive Manufacturing of Complex Geometries using Continuous Fiber-Reinforced Thermoplastic Composites

MATHIEU VERVILLE
Département de génie mécanique

Mémoire présenté en vue de l'obtention du diplôme de *Maîtrise ès sciences appliquées*
Génie mécanique

Octobre 2025

POLYTECHNIQUE MONTRÉAL
affiliée à l'Université de Montréal

Ce mémoire intitulé :

Additive Manufacturing of Complex Geometries using Continuous Fiber-Reinforced Thermoplastic Composites

présenté par **Mathieu VERVILLE**
en vue de l'obtention du diplôme de *Maîtrise ès sciences appliquées*
au jury d'examen constitué de :

Louis LABERGE-LEBEL, président
Daniel THERRIAULT, membre et directeur de recherche
Ilyass TABIAI, membre

ACKNOWLEDGEMENTS

I would like to thank my supervisor, Prof. Daniel Therriault, for his guidance, support, and the many opportunities he provided, as well as for the trust he placed in me over the last four years. I am truly proud of the work we accomplished together, and I am grateful for the enriching conference and teaching experiences he made possible. I am also thankful to Rouhollah Farahani and Kambiz Chizari, who were always ready to offer me their help and insight.

I want to thank all my colleagues as well, who became friends throughout my time at the LM^2, especially Loïc, Raphaël, Josua, Olivier, Negar, Alice, Dogan, Luca, Danick, Yannis, Ghita, Dorian, Étienne, Saeideh, Antoine, Ludivine, Vincent and Minh-Tam. They not only provided help whenever needed but also made my time with them truly memorable. A special thank you to the LM^2 alumni, Juliette and Jean-François, whose friendship and mentorship were invaluable when I first started at the lab. It was a real pleasure to work with all of you.

I am also grateful to Baptiste and Lohan for their precious help with the μCT and the g-code post-processor during their internships, and to our technician Adrien, who consistently went above and beyond to assist all of us in our projects and my lab management tasks.

My heartfelt thanks go to my mom, my dad, and my girlfriend, Luisa, for their unwavering support during my studies and for always being there for me. I could not have done it without you.

Finally, I want to acknowledge the insight and collaboration offered by my colleagues Jack Turicek and Prof. Jason Patrick at North Carolina State University (NCSU) during my project. I also acknowledge the CRSNG for their funding and my scholarship, as well as Dyze Design, for their collaboration and contribution to my project.

RÉSUMÉ

La fabrication additive (FA) est une famille de technologies de plus en plus utilisée afin de créer des géométries optimisées et plus légères, généralement impossibles à fabriquer par des méthodes conventionnelles. Cependant, les techniques existantes de FA présentent des limites. La FA métallique, malgré les hautes résistances et rigidités obtenues, est pénalisée par la haute densité des métaux. Les composites thermoplastiques renforcés de fibres courtes, bien que légers, assez rigides et recyclables, offrent une résistance mécanique limitée. Afin de remédier à ces lacunes, le développement de la FA de polymères renforcés de fibres continues (FA-PRFC) est une option prometteuse. Cette approche vise à combiner les avantages associés à la FA de formes complexes avec la haute résistance et la haute rigidité spécifiques de cette gamme de matériaux.

Ce mémoire présente donc le développement d'une infrastructure de FA de composites renforcés de fibres continues. Le système intègre un outil de co-extrusion à un système de FA robotique déjà développé au laboratoire de mécanique multi-échelle (LM^2), afin de réaliser une imprégnation *in-situ* des fibres. Cette approche vise à permettre l'utilisation de matières premières génériques et à réduire la dépendance aux matériaux préimprégnés propriétaires utilisés par la plupart des systèmes disponibles commercialement. L'efficacité de cette infrastructure a été validée avec deux combinaisons de matériaux : (1) de l'acide polylactique renforcé de fibres de verre continues (PLA-CGF) et (2) du PLA renforcé de fibres de carbone courtes et continues (PLA-SCCF).

Une analyse de la microstructure par microtomographie de pièces unidirectionnelles en PLA-SCCF a révélé une fraction volumique de fibres continues de 44 vol.% (i.e., environ 58 wt.%) ainsi que des taux de vides et de porosités de 0,4 vol.% et 7,9 vol.%, respectivement. Des tests mécaniques ont démontré une résistance à la traction de 854 MPa et une rigidité de 29,5 GPa dans la direction des fibres. Ces valeurs représentent une augmentation de 16× en résistance et de 6× en rigidité par rapport à un composite de PLA renforcé uniquement de fibres courtes (PLA-SCF). La résistance spécifique obtenue dans la direction des fibres est également 8× supérieure à celle des pièces issues de la FA métallique.

Pour démontrer la capacité de l'infrastructure de co-extrusion à fabriquer des géométries 3D complexes, un vase à paroi mince et un panneau sandwich multi-matériaux ont été imprimés. Leur fidélité géométrique a été mesurée et des écarts inférieurs à 1% des dimensions des pièces ont été obtenus pour les deux géométries. Les défauts observés, principalement dus à l'extrusion de matière non supportée sur une distance de 31 mm, se sont concentrés dans la

peau supérieure du panneau sandwich. Bien que 13× plus élevés que dans la peau inférieure, ils représentent tout de même une réduction de ∼42% par rapport aux valeurs rapportées dans la littérature pour des structures similaires fabriquées par FA.

Bien que des limites subsistent, notamment pour les structures non supportées sur de longues distances, la méthode développée démontre une capacité à fabriquer des pièces 3D complexes avec des propriétés spécifiques parmi les plus hautes rapportées pour la FA-PRFC jusqu'à présent. Ces résultats prometteurs pour un procédé d'imprégnation *in-situ* pourraient être appliqués à l'automatisation de la fabrication de pièces composites complexes, réduisant le besoin d'assemblage et offrant une plus grande liberté de conception dans les secteurs exigeants et nécessitant une réduction de la masse, comme l'aérospatiale ou l'automobile.

ABSTRACT

The use of additive manufacturing (AM) has been increasingly researched as a means to reduce material waste and enable the fabrication of optimized geometries, producing lightweight structures not achievable using conventional means of fabrication. Metallic AM provide excellent design freedom and high mechanical properties, but the high density of metals results in lower specific properties when compared to other material categories such as composites. Short fiber-reinforced thermoplastic composites, specifically, are recyclable and offer good specific stiffness. They are also compatible with fused filament fabrication, a widely used AM process able to manufacture complex geometries. They, however, provide limited strength due to the discontinuous nature of their reinforcements. Continuous fiber-reinforced thermoplastic composites AM (CFRP-AM) therefore, becomes an interesting solution, combining the capacity to produce complex architectures with high specific strengths and stiffness. While recent efforts have mainly been focused on improving the mechanical properties of geometries manufactured using these methods, the parts manufactured are usually small and 2D shapes that do not leverage the geometric complexity, justifying the use of AM. Few have demonstrated the capacity to produce complex 3D shapes, and the geometrical fidelity has not yet been quantified. Furthermore, current methods either rely on proprietary pre-impregnated material feedstock, limiting material choices and increasing the production costs, or use *in-situ* impregnation methods that still have to demonstrate their capacity to provide mechanical properties comparable to pre-impregnated alternatives.

In this thesis, we develop a CFRP-AM infrastructure able to print continuous fiber-reinforced thermoplastics using generic material feedstocks. For this purpose, a co-extrusion *in-situ* impregnation printhead is integrated into the 6-axis robotic AM infrastructure present at the laboratory for multi-scale mechanics (LM^2) and a CFRP-AM workflow is designed to automate the program generation. The infrastructure is then tested using 2 material combinations: (1) Continuous glass fiber-reinforced polylactic acid (PLA-CGF) and (2) Short and continuous carbon fiber-reinforced polylactic acid (PLA-SCCF).

The micro and meso-structures of PLA-SCCF unidirectional flat beams are then observed using micro-computerized tomography scans (μCT). The continuous fiber volume fraction is 44 vol.% ($\sim$58 wt.%) while voids and porosities represent 0.4 vol.% and 7.9 vol.%, respectively. The ultimate tensile strength and stiffness along the principal direction are measured to be 854 MPa and 29.5 GPa. These values represent a 16$\times$ and 6$\times$ increase over short fiber-reinforced PLA (PLA-SCF) manufactured via FFF, respectively. While the specific stiffness

is comparable to results reported for metallic AM, the specific strength in the fiber orientation is 8× higher.

To demonstrate the capacity to manufacture complex 3D geometries using the developed co-extrusion infrastructure, a curved thin-walled vase and a multi-material sandwich panel are made using the proposed method. Their geometrical fidelity is measured, and their deviations from the reference model are both <1% of the part dimensions. Defects are mainly located in the top skin of the sandwich panels, with a void volume fraction 13× higher than in the bottom skin. These defects are associated with the bridging of up to 31 mm present in this region (i.e., mid-air extrusion of an unsupported structure) and are a ∼42% decrease over reported values for AM sandwich panels.

While presenting certain limitations regarding bridging sections over long distances, the method developed shows a capacity to manufacture complex 3D geometries using generic continuous fiber-reinforced composite feedstocks. While transverse properties still need to be assessed, tensile results are promising for an *in-situ* impregnation AM methods and the specific properties achieved are among the highest reported for CFRP-AM thermoplastic composites until now. Similar manufacturing infrastructures could be used to automate the fabrication of composite parts with high geometric complexities, enabling more design freedom and reducing need for assembly. It could find applications in highly demanding sectors where light-weighting is a concern, such as the automotive and aero-spatial industries.

TABLE OF CONTENTS

LIST OF TABLES

LIST OF FIGURES

LIST OF SYMBOLS AND ACRONYMS

3D	Three-Dimensional
AFP	Automated Fiber Placement
AM	Additive Manufacturing
AWV	Angled, <1 width from tab, Various
β	Shear-Lag Parameter
BMD	Bound Metal Deposition
C2M	CAD To Mesh
CAD	Computer Aided Design
$CI_{90\%}$	90% Confidence Interval
$CI_{95\%}$	95% Confidence Interval
CFRP-AM	Continuous Fiber-Reinforced Polymer Additive Manufacturing
CFRPs	Continuous Fiber-Reinforced Polymers
DC	Direct Current
DFRPs	Discontinuous Fiber-Reinforced Polymers
DI	Degree Of Impregnation
DIW	Direct-Ink Writing
DMLS	Direct Metal Laser Sintering
DoF	Degrees Of Freedom
d	Diameter
d_f	Fiber Diameter
E	Tensile Modulus
$E(\phi)$	Modulus Along An Arbitrary Direction
E_1	Modulus Along The Fiber Direction
E_1'	Secondary Stiffness
E_{12}	In-Plane Shear Coupling Term
E_2	Transverse Modulus
E_{ccf}	Continuous Carbon Fiber Stiffness Along The Fiber Direction
E_f	Fibers Young's Modulus
E_m	Matrix Young's Modulus
E_{scf}	Short Carbon Fiber Stiffness Along The Fiber Direction
ϵ_1	Average Composite Strain
η_l	Length Correction Factor
FEM	Finite Element Modelling

FFF	Fused Filament Fabrication
G_m	Matrix Shear Modulus
GUI	Graphical User Interface
HTML	HyperText Markup Language
HS	Hardened Steel
HSS	High Speed Steel
ID	Inner Diameter
L_c	Critical Fiber Length
LM^2	Laboratory For Multi-Scale Mechanics
LPBF	Laser Powder Bed Fusion
LWV	Lateral, <1 width from tab, Various
l	Fiber Length
MIM	Metallic Injection Moulding
MEAM	Material-Extrusion Additive Manufacturing
μCT	Micro Computerized Tomography
NEMA	National Electrical Manufacturers Association
PEEK	Polyetheretherketone
PEI	Polyetherimide
PEI-CF	Short Carbon Fiber-Reinforced Polyetherimide
PEKK	Polyetherketoneketone
PLA	Polylactic Acid
PLA-CGF	Continuous Glass Fiber-Reinforced Polylactic Acid
PLA-SCCF	Short And Continuous Carbon Fiber-Reinforced Polylactic Acid
PLA-SCF	Short Carbon Fiber-Reinforced Polylactic Acid
PPA-CF	Short Carbon Fiber-Reinforced Polyphtalamide
PTFE	Polytetrafluoroethylene
ϕ	Average Fiber Angle
ϕ_{ccf}	Continuous Carbon Fibers Average Angle
ϕ_{scf}	Short Carbon Fibers Average Angle
R	Half Inter-Fiber Distance
RTM	Resin Transfer Moulding
SFRP-AM	Short Fiber-Reinforced Polymer Additive Manufacturing
SLM	Selective Laser Melting
SLS	Selective Laser Sintering
SMV	Longitudinal Splitting, Multiple Areas, Various
.STL	Standard Triangle Language

TCP	Tool Center Point
T_m	Melting Temperature
TiN	Titanium Nitride
TPU	Thermoplastic Polyurethane
θ_{blade}	Angle Between the Blade Edge And Movement
UV	Ultraviolet
UTS	Ultimate Tensile Strength
V_{ccf}	Continuous Carbon Fiber Volume Fraction
$V_{ccf,eff}$	Effective Continuous Carbon Fiber Volume Fraction
$V_{ccf,tow}$	Continuous Carbon Fiber Volume Fraction In Tow
V_f	Fiber Volume Fraction
V_m	Matrix Volume Fraction
$V_{m,tow}$	Matrix Volume Fraction In Tow
V_p	Porosity Volume Fraction
V_{scf}	Short Carbon Fiber Volume Fraction
V_v	Inter-Layer Voids Volume Fraction
σ_1	Tensile Strength Along The Fiber Direction
$\sigma_{1,f}$	Axial Stress In A Fiber
σ_f	Fiber Tensile Strength
σ_m	Matrix Tensile Strength
σ_{ccf}	Continuous Carbon Fiber Tensile Strength
σ_{scf}	Short Carbon Fiber Tensile Strength
τ_i	Interfacial Shear Strength

CHAPTER 1 INTRODUCTION

1.1 Project context

The growth of awareness concerning climate change has pushed engineers to aim for greener practices regarding manufacturing and design, and to innovate in sectors such as material sciences. In recent years, the use of composite materials has been investigated as a way to reduce weight in applications where each gram comes with an associated carbon footprint, such as the aeronautical and the automotive industries [1, 2]. Conventional manufacturing methods for composites, however, rely heavily on thermosetting polymer resins as the host matrix. These resins are hard to recycle and rely on the use of many consumables. Fiber-reinforced thermoplastic composites are an alternative that facilitates recycling and repair of the manufactured components, as well as reducing the need for unsustainable consumables [3].

Additive Manufacturing (AM) is a category of processes that fabricates three-dimensional (3D) geometries layer-by-layer. It reduces material waste and eliminates the need for expensive moulding equipment. It also allows the manufacturing of complex geometries otherwise hard to achieve using other popular manufacturing methods, such as injection moulding or machining [4]. Common uses of these new possibilities are the fabrication of topology optimized structures [5,6] or assemblies printed in a single manufacturing step (i.e., *print-in-place* components) [7, 8]. These optimized and fastener-free alternatives are usually lighter than conventionally manufactured components, further contributing to the reduction of carbon emissions.

Fused filament fabrication (FFF) has become a widely used process due to its low costs and high speeds when compared to other AM methods. It is also compatible with a wide range of neat thermoplastics [9], but is also capable of Short Fiber-Reinforced Polymer Additive Manufacturing (SFRP-AM) for improved mechanical properties compared with the neat polymers [10–14], especially the material stiffness. Although cheaper and faster than other AM methods, FFF has limitations regarding the geometric features possible to make, mainly regarding bridging areas (i.e., unsupported sections where material is printed in mid-air). FFF printed results usually present defects related to bridging in those regions, like visible sagging [15, 16] and increased porosity [17].

Continuous Fiber-Reinforced Polymer Additive Manufacturing (CFRP-AM) has been increasingly researched as a means to significantly increase the mechanical properties of parts made by AM [18–21]. Tailor-made pre-consolidated continuous fiber-reinforced 3D-printing

filaments have been extensively used [22–25], with efforts focused on improving mechanical properties by increasing the fiber content [26, 27] and the fiber impregnation [22, 28–30] or by reducing the voids [24]. For this approach, specialized equipment (e.g., pultrusion lines) is required to avoid the use of expansive proprietary materials (e.g., Markforged continuous carbon fiber) [31, 32], therefore limiting the material selection or increasing the material costs [33]. *In-situ* impregnation methods have been investigated to remedy this issue, such as co-extrusion AM [34–37]. While the material selection is increased and specialized material preparation equipment isn't required, these methods typically provide limited mechanical properties due to the low impregnation and fiber content achievable.

Although advances were made regarding the mechanical properties of composites made via AM, most solutions are currently limited to manufacturing small and flat beams (i.e., 2D or 2.5D) due to the lack of *in-situ* fiber cutting mechanism creating fiber discontinuities to enable travel movements. The need for complex *in-situ* impregnation systems is also limiting the possible printing orientations, forcing the use of simple tool paths similar to those used for automated fiber placement (AFP) [24]. The achievable geometric complexity is therefore greatly limited by those methods. Furthermore, to the best of our knowledge, the geometric fidelity (i.e., the deviation between the numerical model and the manufactured part) has not been evaluated nor quantified for CFRP-AM methods.

1.2 Research objectives

The need for AM methods capable of producing complex 3D shapes and offering high mechanical properties has been described. The specific material feedstock requirement has been identified as a limiting factor for CFRP-AM methods, and their geometric fidelity remains unquantified.

This project establishes the following three objectives :

- **O1 :** Develop a continuous fiber-reinforced composite additive manufacturing infrastructure compatible with non-specific reinforced thermoplastics material feedstock,
- **O2 :** Evaluate the tensile mechanical properties of flat unidirectional composite beams manufactured using the developed infrastructure, and
- **O3 :** Demonstrate the capacity of the developed infrastructure to manufacture complex geometries.

1.3 Thesis outline

This thesis is organized into five main chapters. Chapter 2 presents the literature review focusing on fiber-reinforced composites, the additive manufacturing of structural parts and the current state of the art of CFRP-AM. Chapter 3 defines the scope of the project, justifies the choices made during the development process of the proposed CFRP-AM infrastructure and describes the general approach used to achieve the three objectives. It also positions the paper presented in the research project. Chapter 4 presents in more detail the development process of the CFRP-AM infrastructure and the main results associated with O1. The scientific article submitted is then presented in Chapter 5, which includes a summary of the O1 results. It also presents the results of O2 and O3, related to the mechanical properties and geometrical characterization of demonstrator parts. Chapter 6 offers a summary of the different results obtained as well as the remaining challenges regarding CFRP-AM. It also offers a list of recommendations for future research on the topic.

CHAPTER 2 LITERATURE REVIEW

2.1 Composite Mechanics

Composite materials are a combination of two or more distinct materials designed to achieve properties superior to those of the individual constituents. Fiber-reinforced polymers are among the most used composite categories due to their high specific mechanical properties (i.e., density-normalized, such as strength-to-density ratio or stiffness-to-density ratio), tunable properties, and capacity to produce complex geometries. These materials combine high-performance reinforcing fibers (e.g., glass, carbon, kevlar, nylon, flax) with a ductile polymer matrix, enabling efficient load transfer while retaining some deformability and damage tolerance [38,39]. In particular, fiber-reinforced thermoplastics possess unique advantages such as improved impact resistance over thermosetting alternatives, reformability and recyclability [1–3]. They are also compatible with advanced manufacturing methods like AFP and additive manufacturing.

The mechanical behaviour of these composites depends on the individual properties of the fibers and matrix, but also on the volumetric ratio, fiber geometry and orientation, and interfacial properties. One of the most important parameters is the fiber volume fraction (V_f) because it significantly influences the strength and stiffness and the failure mechanisms [39, 40]. An increase of V_f means the composite behaviour becomes more fiber-dominated, improving mechanical performance in the directions of the fibers, but often reducing toughness, manufacturability and transverse properties (i.e., where loading is perpendicular to the fiber direction).

2.1.1 Continuous Fiber-Reinforced Polymers

Continuous fiber-reinforced polymers (CFRPs) are composites where the fibers are typically the full length of the component. It enables efficient load transfer along the fiber direction through the whole part, resulting in composites with outstanding strength and stiffness in the fiber direction. CFRPs are widely used in aerospace, automotive, and structural applications where very high performance-to-weight ratios are critical [39]. They can be added as individual fiber tows in continuous processes like melt impregnation, pultrusion, or filament winding [39]. CFRPs are also often woven into textiles and stacked in different laminate configurations that are used as a reinforcement during manufacturing using methods such as vacuum bagging, resin transfer moulding (RTM), autoclave processing, or compression

moulding [39]. Despite their high-performance potential in the fiber direction, CFRPs are highly anisotropic (i.e., their properties vary in different directions). To mitigate this issue, quasi-isotropic laminates are often used. These stacking configurations (e.g., [0/60/-60]° and [0/±45/90]° laminate stacking sequences) vary the fiber orientation every layer to obtain apparent in-plane elastic properties that are independent from the orientation (i.e., 2D isotropy) [39]. They, however, offer reduced performance when compared to aligned stacking sequences (e.g., unidirectional [0]°, symmetric [0/90/0]°) if the loading conditions are well known (e.g., uniaxial loading, simple bending). To further improve the strength-to-weight and stiffness-to-weight ratios of components, advanced manufacturing methods like tailored fiber placement, AFP, or AM can be used to precisely align the fiber paths with the loading conditions.

Mechanical properties of unidirectional CFRPs can be estimated using micro-mechanical models such as the rule of mixture [39]. For axial loading along the fiber direction, the modulus along the fiber direction (E_1) is defined as :

$$E_1 = V_f \cdot E_f + V_m \cdot E_m, \tag{2.1}$$

with E_f and E_m the Young's modulus of the fibers and matrix, respectively, and V_m the matrix volume fraction. This equation assumes perfect bonding and uniform strain distribution across the phases.

Similarly, the tensile strength along the fiber direction (σ_1) can be estimated using a rule-of-mixture [39] :

$$\sigma_1 = V_f \cdot \sigma_f + V_m \cdot \sigma_m, \tag{2.2}$$

with σ_f and σ_m the tensile strengths of the fiber and matrix, respectively. The Equation 2.2 also assumes perfect bonding, uniform strain distribution and fibers failing first. Since fibers have much lower strain at break than the matrix, and the strain is being considered uniform, they typically break first.

Due to the more complex stress transfer mechanisms, the transverse modulus (E_2) requires more advanced models such as the semi-empirical inverse rule of mixtures [39] :

$$E_2 = \left(\frac{V_f}{E_f} + \frac{V_m}{E_m} \right)^{-1}. \tag{2.3}$$

When fibers are not aligned or perpendicular to the loading direction, the mechanical prop-

erties become orientation-dependent. The modulus along an arbitrary direction relative to the fiber direction ($E(\phi)$) can be estimated using the Tsai–Pagano approximation [41] :

$$E(\phi) = E_1 \cdot \cos^4 \phi + 4 \cdot E_{12} \cdot \sin^2 \phi \cdot \cos^2 \phi + E_2 \cdot \sin^4 \phi, \tag{2.4}$$

where E_{12} is a coupling term related to in-plane shear. For small ϕ angles, the modulus can estimated using the 2D transformation of Eshelby's stiffness tensor [39] :

$$E(\phi) = V_f \cdot E_f \cdot \cos^4 \phi + V_m \cdot E_m, \tag{2.5}$$

Using the projected axial stress, a similar expression can be applied for the tensile stress along an arbitrary direction [39] :

$$\sigma(\phi) = V_f \cdot \sigma_f \cdot \cos^2 \phi + V_m \cdot \sigma_m, \tag{2.6}$$

These orientation-dependent models are important for laminates or process-induced misalignment, but also curved composite paths, such as the ones present in advanced manufacturing methods. CFRPs require precise manufacturing and extensive quality control, especially when using novel manufacturing methods for which micro-structure characterization and defects identification are crucial. The CFRP's sensitivity to defects like voids and micro-cracks can otherwise lead to delamination and catastrophic failure [39].

2.1.2 Discontinuous Fiber-Reinforced Polymers

Unlike CFRP, which incorporates fibers unbroken through the whole part, discontinuous fiber-reinforced polymers (DFRPs) instead include shorter fibers dispersed within the polymer matrix. While offering reduced mechanical properties when compared with CFRPs, they significantly improve the processability and are compatible with most conventional processing techniques (e.g., injection moulding, extrusion, additive manufacturing). They can also exhibit 3D apparent isotropic properties when using random fiber distribution, as opposed to the in-plane 2D isotropy of quasi-isotropic laminates.

However, DFRPs offer less efficient load transfer due to fiber discontinuity. The load is transferred to the fibers through shear stress along the fiber-matrix interface, but cannot be carried continuously by the fibers across the length of the part. The matrix, therefore, plays a significant role by carrying load locally between fibers, resulting in matrix-driven properties [40]. For fibers to carry their maximum tensile loads and permit complete stress

transfer from the matrix, their length must exceed a critical value. The critical fiber length (L_c) is defined by:

$$L_c = \frac{\sigma_f \cdot d}{2\tau_i}, \tag{2.7}$$

with d the fiber diameter and τ_i the interfacial shear strength between the fiber and the matrix [40].

Stress distribution in short fibers is often modelled using the Cox shear-lag model [39, 42]. By assuming that stress builds up along the fiber through shear deformation in the matrix, the axial stress in a fiber ($\sigma_{1,f}(x)$) at a position x is given by :

$$\sigma_{1,f}(x) = E_f \cdot \epsilon_1 \cdot \left(1 - \frac{\cosh(\beta \cdot x)}{\cosh(\beta \cdot l/2)}\right), \tag{2.8}$$

with ϵ_1 the average composite strain, l the fiber length and β a shear-lag parameter depending on the fiber and matrix modulus and geometry. From this model, the longitudinal modulus of DFRP composite can be derived and is defined as [39, 42, 43] :

$$E_1 = V_f \cdot E_f \cdot \eta_l + V_m \cdot E_m, \tag{2.9}$$

with η_l a length correction factor defined as :

$$\eta_l = 1 - \frac{\tanh(\beta \cdot l/2)}{\beta \cdot l/2}. \tag{2.10}$$

DFRPs' anisotropy and mechanical properties are also strongly influenced by fiber orientation. If the orientation distribution is known, Mori–Tanaka homogenization can be applied [44]. It uses Eshelby's solution to calculate the strain concentration tensor of individual inclusions and integrates over the orientation distribution function, enabling the prediction of the effective modulus for composites with randomly oriented fibers. For fiber distributions partially aligned with the loading direction, Cox's micro-mechanical model [42] can be extended using orientation averaging techniques based on Eshelby's theory [43]. In this scenario, a simpler modified rule of mixture can be used to estimate the longitudinal modulus :

$$E_1 = V_f \cdot E_f \cdot \eta_l \cdot \cos^4 \bar{\phi} + V_m \cdot E_m, \tag{2.11}$$

with $\bar{\phi}$ the average fiber angle.

These modified rules of mixtures are particularly important in processes like extrusion-based additive manufacturing, where the short fibers are partially aligned during the extrusion process [43].

2.2 Additive manufacturing of structural parts

AM offers new opportunities regarding the manufacturing of structural components, making possible the fabrication of high complexity geometries which are impossible to manufacture otherwise (e.g., using moulding or machining) [4]. These new possibilities include structures resulting from topological optimization or generative design, which are made of organic shapes and fine details hard to reproduce otherwise. These complex optimized structures have been largely researched as a means of reducing the weight of structures without impacting their load-bearing functions [5,6]. Other possibilities include the fabrication of otherwise assembled structures in a single manufacturing step, reducing the production costs, removing the need for failable fasteners or binders and enabling multifunctional structures (e.g., noise reducing sandwich panels [12, 45], noise reducing abradable layers [46], shape morphing structures [47]). The two most common 3D printable material categories used for these advanced load-bearing structures are metals and polymer composites, detailed in Sections 2.2.1 and 2.2.2 respectively.

2.2.1 Metallic AM

The most common metallic additive manufacturing method is Laser Powder Bed Fusion (LPBF) [48]. Figure 2.1a presents a schematic of the LPBF process. A metallic powder is spread on a bed using a roller to form a thin layer that is either sintered, Direct Metal Laser Sintering (DMLS), or melted, Selective Laser Melting (SLM), using a laser, solidifying regions of interest. The roller then adds successive layers that are sequentially sintered or melted, eventually resulting in a solid 3D part [49, 50]. Components produced using these methods usually exhibit near isotropic properties [51], making them a good AM option for applications where multi-axial loads are applied. Parts being made of metals, mechanical properties are also among the highest achievable using AM (e.g., tensile strength between 240 MPa [52] and 630 MPa [53]). Figure 2.1b shows a part manufactured by LPBF. By forming a solid part in a densely packed powder, both methods can also achieve high-quality overhanging (i.e., surfaces angled relative to the normal of the build direction) and bridging (i.e., printing over unsupported areas) features without requiring supporting structures [51].

The surface finish is, however, rougher than other AM methods due to the powder-based nature of the process [49–51]. Furthermore, DMLS and SLM can only produce monolithic volumes (i.e., entirely filled with solid material, with an infill of 100%) since partial sintering or melting of the inside regions would result in trapped powder.

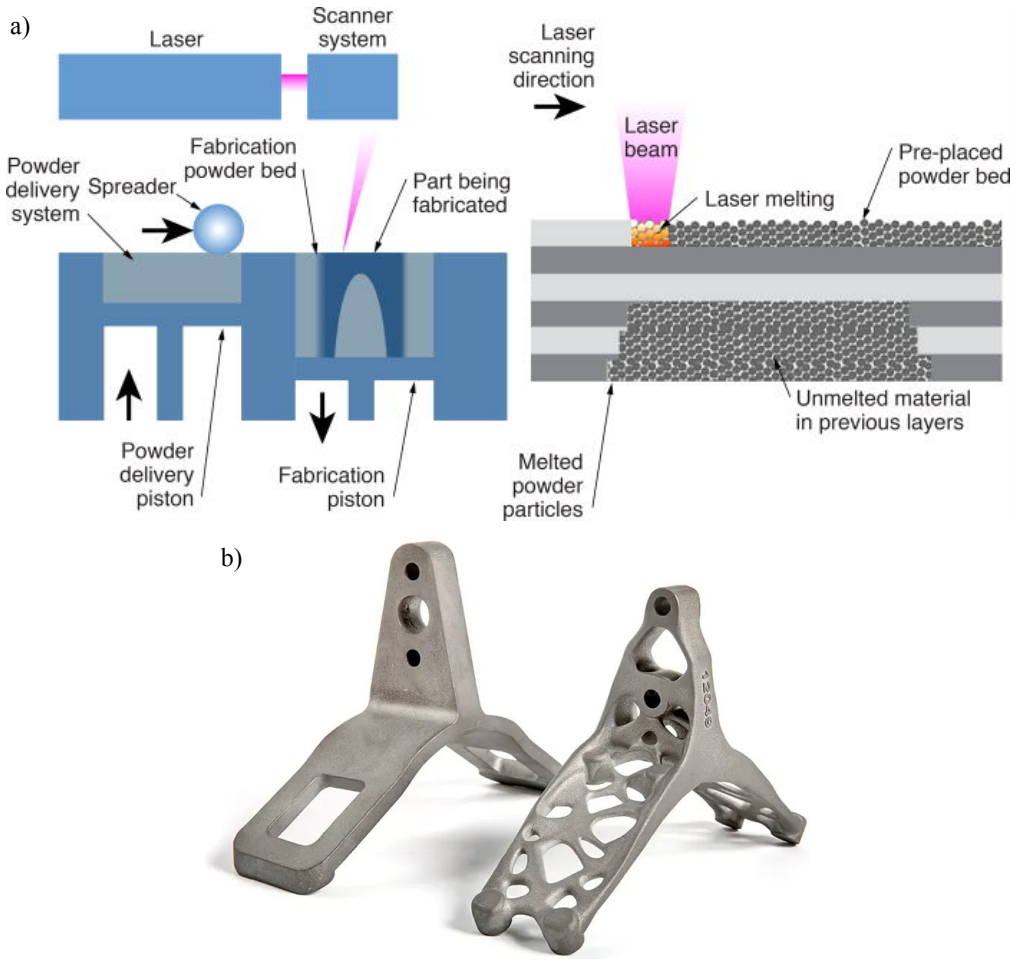

Figure 2.1 **LPBF of metallic parts.** a) Schematic of the LPBF working principle [54]. b) Photograph of a metallic LPBF printed bracket and its topologically optimized counterpart [55]

Bound Metal Deposition (BMD), also referred to as FFF-based metallic AM, is a more affordable alternative to laser-based AM [56]. Figure 2.2a presents a schematic of the various steps of this process. It uses metallic injection moulding (MIM) material feedstocks, composed of metallic powders bound using a thermoplastic matrix that can be extruded through a heated nozzle and deposited on a build platform layer-by-layer to form a 3D volume. The resulting part, called *green part*, must then be placed in a solvent bath to partially remove the binder, leaving a *brown part* of partially bound metallic particles. This *brown part* is then

fully debinded and sintered using a kiln or an oven, resulting in a final solid part. Figure 2.2b shows a part after the printing and sintering steps. Mechanical post-processing, such as machining and polishing, is often also required to achieve the desired surface finish and tolerances. Although cheaper, BMD produce parts exhibiting lower mechanical properties than their DMLS and SLM counterparts [57]. They also suffer from part shrinkage during the final sintering step, reducing the geometrical fidelity of the parts manufactured [58, 59], and the surface finish is usually worse than that obtained by laser-based methods. The process also carries the overhang and bridging limitations associated with FFF [56, 57]. However, since this method does not use a powder bed, it can manufacture hollow geometries (i.e., with an infill lower than 100% [60], enabling the manufacturing of hollow structures such as sandwich panels.

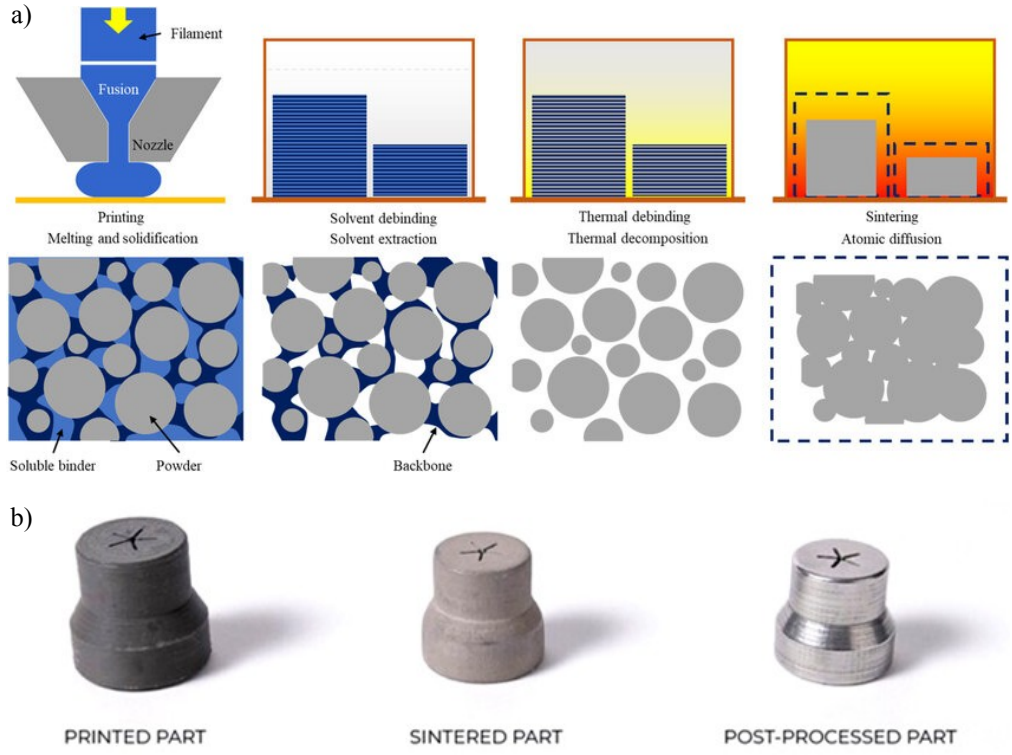

Figure 2.2 **Bound Metal Deposition.** a) Schematic of the BMD printing and post-processing steps [61]. b) Photograph of a stainless steel component after BMD printing, sintering and mechanical post-processing [62]

2.2.2 SFRP-AM

Although exhibiting exceptional mechanical properties, metals also possess high densities, limiting their use in applications where mass reduction and total volume are a concern (e.g., in

aeronautical or space industries). Composites, especially fiber-reinforced polymer composites, have been increasingly researched as an AM material. Their high specific properties combined with the advantages of AM would make them ideal for fabricating lightweight load-bearing structures [38].

Selective Laser Sintering (SLS) is an LPBF method used to sinter thermoplastic powders and short fiber-reinforced thermoplastic composite powders [63]. Its working principle is virtually the same as the one described for DMLS in Section 2.2.1. Figure 2.3a shows a composite component made by SLS. Parts manufactured using this method present the same geometric characteristics as metallic SLS (e.g., complex geometries with many overhanging features and rough surface finish), but possess the strength of short fiber-reinforced thermoplastics (e.g., tensile strength between 65 MPa [64] and 117 MPa [65]). The reduced laser power required to sinter polymers also makes polymer SLS much cheaper compared to metallic SLS and SLM.

Material-Extrusion Additive Manufacturing (MEAM), most commonly FFF, is the most common form of composite AM. Figure 2.3b presents a schematic of the FFF working principle. It typically uses a slicing software to convert a 3D shape into a stacking of thin layers. A thermoplastic or short fiber-reinforced thermoplastic filament is heated and melted, and then extruded through a nozzle and deposited in fine layers to gradually build the part [9]. Contrary to FFF-based metallic AM, and because no ulterior debinding and sintering steps are required, parts manufactured using this method do not significantly shrink. Not being a powder-based process, parts manufactured also don't exhibit the rough surface finish associated with laser-based and FFF-based metallic parts. Figure 2.3c shows a component made using this method. Cheap and simple when compared to other methods, it can produce high-fidelity composite components. While neat polymer FFF often produce a smoother surface finish, the addition of short fibers usually results in a rougher finish. Like its metallic counterpart, it is also limited for printing features like overhangs and bridging [15–17]. Due to the nature of short fiber-reinforced composites, the mechanical properties (e.g., tensile strength of 93 MPa [66] for high-performance short carbon fiber-reinforced polyetherimide (PEI-CF)) are comparable to those achievable by using SLS of polymers and aren't suitable for applications demanding ultra-high strength.

2.2.3 CFRP-AM

CFRP-AM is a different branch of MEAM aiming to keep the same advantages as FFF while increasing the mechanical properties by orders of magnitude. Composed of several sub-branches, this category of processes focuses on the addition of continuous fiber reinforce-

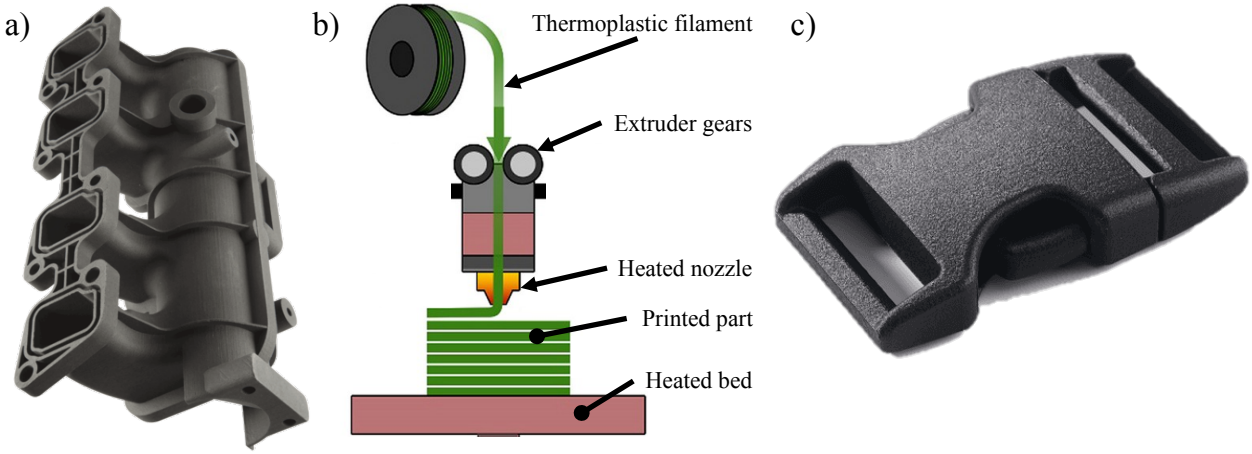

Figure 2.3 **AM of polymer composites.** a) Photograph of a PA12-CF component made by SLS [67]. b) Schematic of the FFF process used for thermoplastic and composite parts [68]. c) Photograph of a short carbon fiber-reinforced high temperature polyamide (PAHT-CF) clip made by FFF [69]

ments to polymer extrusion AM methods, eliminating the limitations associated with the discontinuous nature of FFF-compatible reinforcements.

State of the art in CFRP-AM

There are two main CFRP-AM categories: methods using pre-impregnated towpreg filaments and methods using dry fiber tows that are impregnated during the printing process. Requiring only a small modification to an FFF printer (i.e., changing the nozzle and extruder gears), the simple extrusion of pre-impregnated towpreg filaments is the most common method in the literature [27, 31, 32, 70–74]. Presented in Figure 2.4a, a continuous fiber-reinforced thermoplastic towpreg filament is pushed through a heated nozzle to be extruded and stacked on the printing bed. Further modifications to FFF printers can also include *in-situ* fiber cutting mechanisms to increase the geometric complexity achievable (e.g., enabling travel movement, sudden changes in printing direction, integration with other AM methods). Due to the typically good impregnation of towpreg filaments, the mechanical properties reached are among the best for CFRP-AM results (e.g., tensile strength between 193 MPa [31] and 986 MPa [32]).

Figure 2.4b shows the co-extrusion (i.e., simultaneous extrusion through a single nozzle) of a pre-impregnated towpreg filament and a neat polymer matrix filament. Aiming to improve the printability of the composite and manufacture even more complex geometries, this approach also reduces the fiber content of the final composite by adding neat matrix and

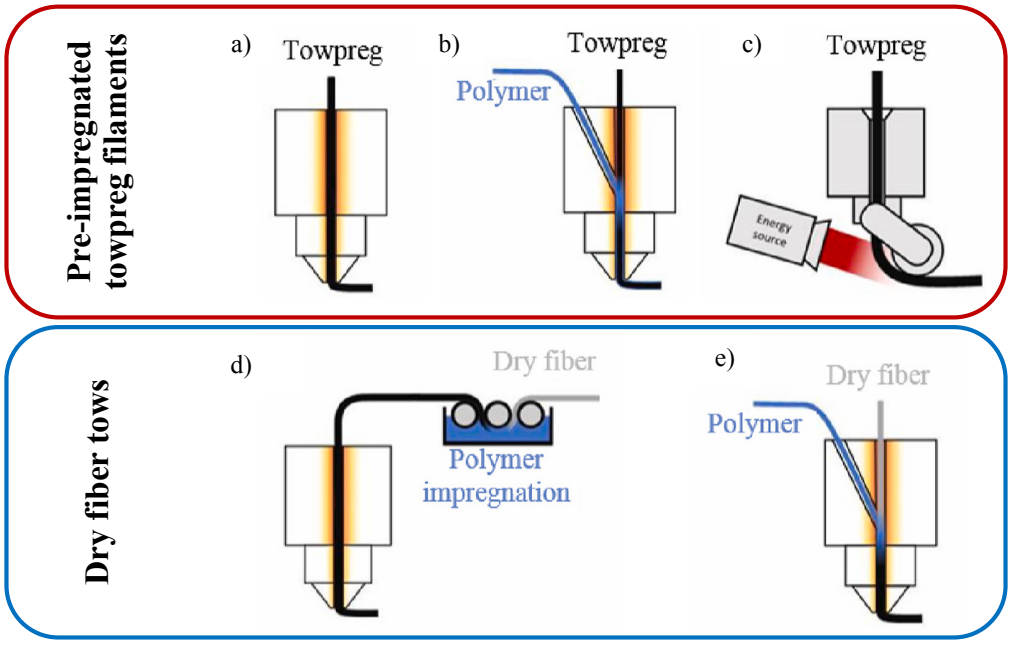

Figure 2.4 **Schematics of the main towpreg (red) and dry fiber tows (blue) CFRP-AM methods present in the literature [21].** a) Extrusion of pre-impregnated towpreg filaments. b) Co-extrusion of pre-impregnated towpreg filaments and polymer matrix. c) *In-situ* impregnation of pre-impregnated towpreg filaments. d) Extrusion of inline impregnated dry fiber tows and polymer matrix. e) Co-extrusion of *in-situ* impregnated dry fiber tows and polymer matrix filaments

often creating matrix-rich regions. Figure 2.4c presents the addition of *in-situ* impregnation mechanisms such as rollers similar to AFP systems [24]. These additions aim to reduce the de-consolidation happening when the heated composite is extruded, improving the resulting mechanical properties (e.g., flexural strength of 584 MPa [24]). The matrix being viscous when exiting the nozzle, the continuous fiber tows often de-consolidate, leading to the creation of voids in the final parts [28, 75].

Instead of towpreg filaments, the second category of methods uses dry fiber tows as reinforcement. Dry fibers are being used in different industry sectors; their use allows for a much greater material selection for the fibers (e.g., glass, carbon, flax), but also for the matrix, which can be selected independently. Figure 2.4d presents the extrusion of composites using inline impregnation. This method requires complex and large components (i.e., similar to continuous melt impregnation or pultrusion) that impregnate the fibers with the matrix before their extrusion. This approach offers results similar to those achieved using towpreg methods (e.g., tensile strength of 736 MPa [29]), but the inline impregnation devices limit the printhead freedom, often leading to the use of a static printhead printing on a moving

build platform [29,76]. While functional for simple parts, it typically leads to more vibration-induced defects, excludes the possibility of using more degrees of freedom (i.e., using a 6-axis robot for non-planar AM [24,77–79]) and limits the build volume that can be achieved.

Other research groups have rather focused on the co-extrusion of *in-situ* impregnated dry fiber tows. Figure 2.4e presents a general schematic of this approach. While different *in-situ* impregnation strategies have been investigated, they all combine the polymer matrix and the fiber tows in the printhead before being co-extruded. The most fundamental approach is to simply have a chamber in the heated nozzle where both the polymer filament and the continuous fibers are fed to be co-extruded [30,34,36,37,80]. These methods exclusively rely on the pressure created by the nozzle tip to push the matrix into the fiber tows [37], often resulting in limited impregnation and lower mechanical performance (e.g., tensile strength of only 191 MPa [37]). Others have tried feeding the polymer matrix from multiple angles to improve the impregnation in all printing directions [81], or to use different polymer matrices to vary the properties *in-situ* [82,83]. To further improve the impregnation and increase the mechanical properties, the use of melt impregnation-inspired pins inside the chamber has also been tried [35].

Still a relatively recent concept, most CFRP-AM systems are currently at the research stage. Figure 2.5a presents an example of towpreg-based *in-situ* impregnation. It uses a roller that needs to be positioned after the extruder, which means the whole printhead needs to be able to turn on itself to produce curved features. The distance between the extruder and roller also limits the minimum radius achievable. The increased size and complexity of the printhead often requires 6-axis robots instead of simpler cartesian FFF printers [24,79], and reduces the geometries possible to manufacture by requiring simpler tool paths. Towpreg-based methods heavily rely on expansive commercial 3D printing towpreg filaments, usually part of proprietary machine ecosystems [33,84]. This limits the material choice and increases the costs of production for industrial applications. To remedy this issue, research groups have focused on the in-house manufacturing of pre-impregnated 3D printing filaments [22,23,85] like the one presented in Figure 2.5b. The setup uses a single die pultrusion-inspired approach to produce towpreg filaments in-house before feeding them to a simple towpreg extrusion machine. While eliminating the reliance on commercial towpreg filaments, it requires complex and expansive manufacturing lines adapted to this specific application. This requirement mitigates the manufacturing simplicity, making the use of towpregs so common. Figure 2.5c presents an in-line impregnation system developed to achieve a good impregnation while eliminating the need to produce towpreg filaments before the AM. However, the resulting printhead being more complex than simple extrusion devices made the design rely on a moving build platform instead of a moving printhead, significantly reducing the build volume and

scalability of the concept. Figure 2.5d presents the schematic of an *in-situ* impregnation co-extrusion printhead, to which pins inspired by the melt impregnation process were added to improve impregnation. The fibers are passing through a molten matrix reservoir where the pins are located, and tension in the fibers creates the pressure required to improve the fiber impregnation. The pin concept demonstrates mechanical improvements over other *in-situ* methods (e.g., tensile strength of 311 MPa [35]). Inline and *in-situ* impregnation methods are mainly designed as continuous processes, which makes the integration of automated cutting mechanisms difficult. For this reason, the parts manufactured using these methods are usually simple flat beams printed in a single continuous movement, thus limiting the geometries possible to fabricate.

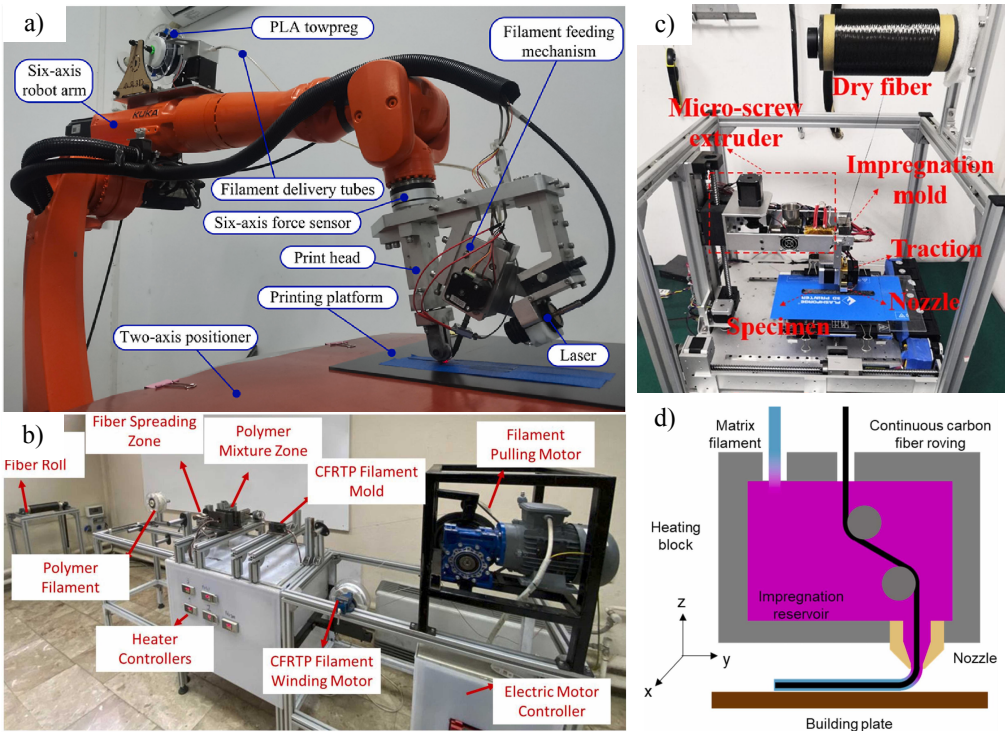

Figure 2.5 **Specific examples of CFRP-AM methods presented in the literature.** a) Photograph of a 6-axis robot using an AFP-inspired roller for *in-situ* impregnation of a towpreg filament, showing the complexity of the toolhead [24]. b) Photograph of a pre-impregnated towpreg filaments making line showing its size and complexity [86]. c) Photograph of a micro-screw extrusion for inline impregnation using a moving build platform [29]. d) Schematic of *in-situ* co-extrusion assisted by a melt impregnation inspired pin system [35]

While still mainly present in research facilities, some commercial machines offer CFRP-AM capabilities. The Markforged Mark Two, shown in Figure 2.6a, is by far the most common commercial 3D printer using the towpreg extrusion process. It possesses a small printing bed that moves vertically and a dual nozzle printhead that either extrudes continuous fibers or

matrix filaments. While being among the first commercial CFRP-AM machines, it is limited to Markforged proprietary materials and only offers a build volume of 320×132×154 mm. It also relies on short fiber-reinforced FFF for most of the part, reinforcing locally with continuous towpreg filaments and resulting in lower continuous fiber volume fractions (e.g., global V_f of only 10.8 vol.%, with neat matrix layers between every fiber layer [31]). Figure 2.6b presents the Anisoprint Composer A4 machine, based on the co-extrusion of thermosetting towpreg continuous fibers. Its general components are similar to the Markforged machine, but the second nozzle used to print continuous fibers combines them with the thermoplastic filament before extrusion. The Anisoprint machines also use proprietary materials exclusively, but their materials contain a thermosetting pre-impregnation matrix, which reduces the recyclability of the produced composite. Although reaching high local fiber volume fractions of up to 65 vol.% [87], they rely on the use of neat FFF as well, reducing the global V_f. Others, such as the commercial system developed by Continuous Composites presented in Figure 2.6c, have integrated the large and complex in-line impregnation system into a robotic motion system. Their technology uses a non-recyclable ultraviolet (UV) curable resin matrix rather than a thermoplastic one. The printhead being bulky and heavy, they also require a high payload capacity 7-axis industrial robot to carry the system, significantly increasing the costs and limiting the geometric precision achievable. To the best of the authors knowledge, while commercially available, this much larger system is custom-made for the client's needs and is currently only found in a few specific research facilities.

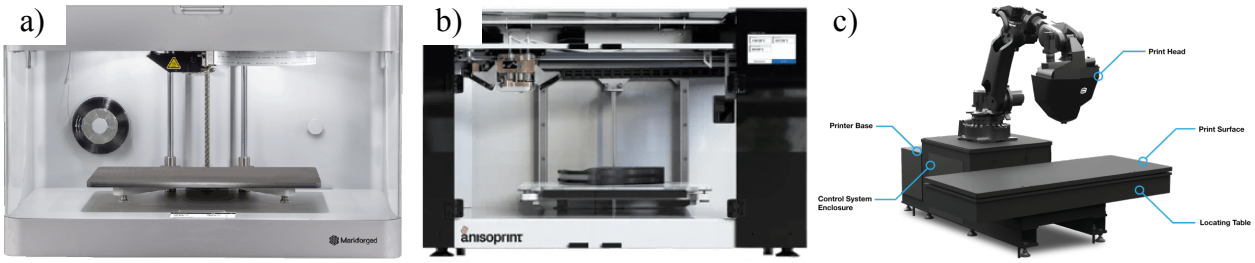

Figure 2.6 **Commercially available CFRP-AM machines.** a) Photograph of the towpreg extrusion based Markforged Mark Two machine [88]. b) Photograph of the towpreg co-extrusion based Anisoprint Composer A4 machine [84]. c) Schematic of the Continuous Composite UV curable thermosetting CFRP-AM system [89]

Current limitations

Although providing limited material choices, towpreg-based CFRP-AM significantly increases the mechanical performance of manufactured composites (e.g., up to 8.4× increase over specimens manufactured via SLS). By comparison, *in-situ* CFRP-AM has shown limited

improvement over other AM methods (e.g., 2.7× increase for samples manufactured using pin-assisted *in-situ* impregnation). While *in-situ* methods are the most limited due to the challenges regarding the integration of cutting mechanisms, both CFRP-AM categories have not currently demonstrated the capacity to produce complex 3D shapes. Figure 2.7a presents a small single-walled curved structure manufactured using towpreg *in-situ* impregnation. Although including in-plane curves, the method can only manufacture vertical walls like the ones visible in Figure 2.7 and is unable to produce overhangs or bridging features. Like most infrastructures developed for research, the system used in this study doesn't have a cutting mechanism, forcing it to print a single continuous path through the whole printed volume. Figure 2.7b presents the methodology often used to manufacture small and flat tensile samples. A flat oblong shape is first printed in a single continuous movement. Cutting the printed part in post-processing is then required to produce the samples. This example illustrates well the limitations currently associated with CFRP-AM methods. Even for towpreg methods such as the ones often used in research, the manufactured geometries are still small and very simple when compared to the complex shapes presented in Sections 2.2.1 and 2.2.2. The need to cut the parts after manufacturing demonstrates the limitations of most current CFRP-AM methods and shows that while improvements were made regarding the mechanical performance, the manufacturing freedom offered by other AM methods has yet to be demonstrated.

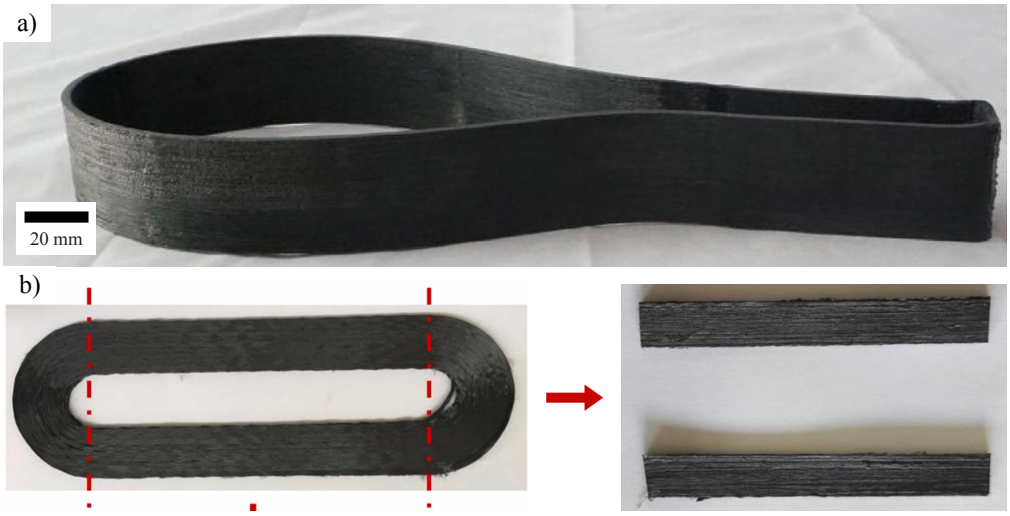

Figure 2.7 **Parts manufactured via CFRP-AM from the literature.** a) Photograph of a vertical single-walled shape manufactured using *in-situ* impregnation of a towpreg filament [24]. b) Sample manufacturing strategy for infrastructures without *in-situ* cutting mechanisms, where a flat oblong shape is printed, then cut into two samples in post-processing [86]

While commercial systems offer overall improved geometrical complexities compared to sys-

tems developed for research, they rely on a combination with FFF to make the complex sections and only reinforce the printed parts locally. Figure 2.8a shows a bracket manufactured using a Markforged machine. While the overall contour is more complex, most of the part is made of a neat polymer matrix. Continuous fibers are only present along the perimeter and do not show variations through the thickness. Figure 2.8b presents a schematic of the reinforcement strategy used by Markforged machines over multiple layers. The machine requires the addition of neat matrix layers between every reinforced layer, which significantly reduces the overall V_f possible and forces the presence of many large matrix-rich regions. Figure 2.8b also highlights the fact that the outer perimeter as well as the top and bottom surfaces are made of neat matrix, resulting in a weaker zone further away from the neutral plane for structures in bending. Figure 2.8c presents a close-up of a component manufactured using the Anisoprint machine, which also features a flat profile uniform through the thickness. For both infill strategies presented, the absence of cuts between each printing path induces defects. There is also a mismatch between the fibers and the part geometry. The fact that only the FFF printed outer shell follows the desired geometry and not the continuous fiber reinforcements shows the reliance of the Anisoprint machine on the secondary FFF process.

Table 2.1 presents a summary of the state of the art in AM of structural components. It presents both the advantages and limitations of the main technologies discussed for metallic AM, SFRP-AM and CFRP-AM.

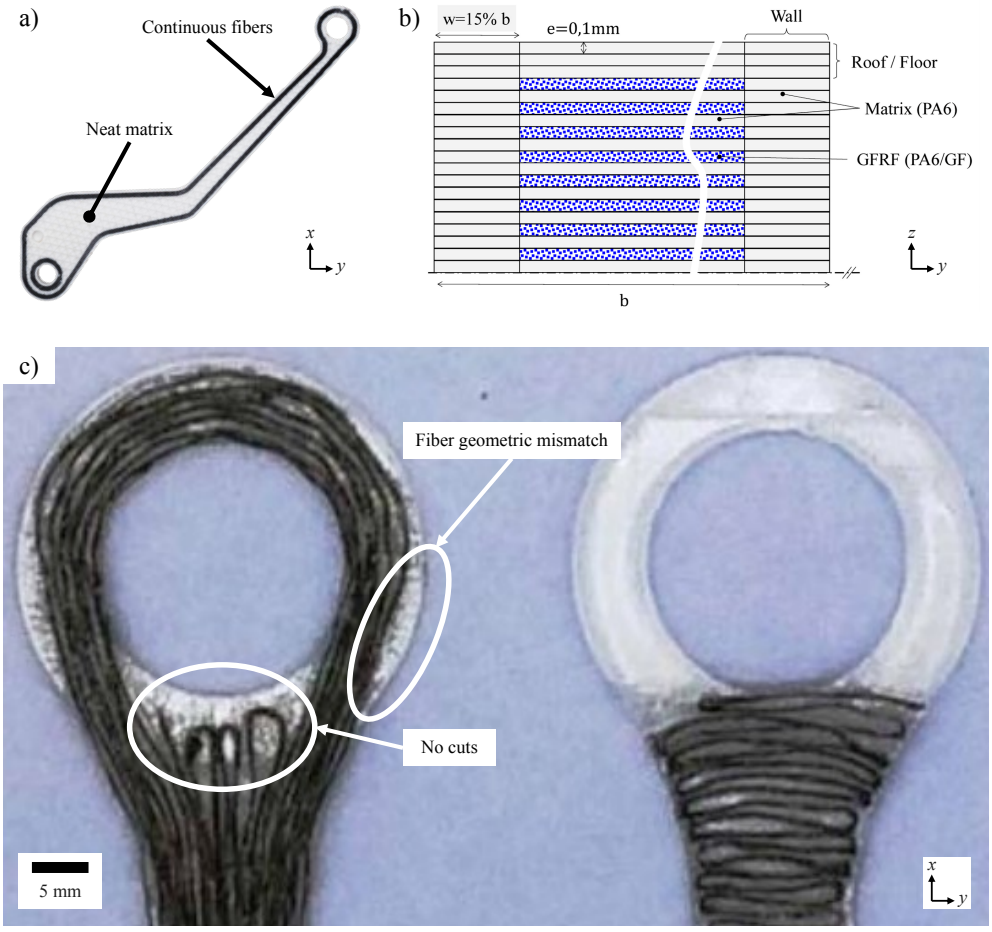

Figure 2.8 **Parts manufactured via commercial CFRP-AM.** a) Photograph of a flat component manufactured using a Markforged machine, showing the local continuous reinforcements on the outer perimeter [33]. b) Schematic of the Markforged continuous reinforcements strategy over multiple layers, showing why the global V_f is lower [31]. c) Photograph of a flat component manufactured using an Anisoprint machine, showing the absence of fiber cuts and the mismatch between the fiber path and the part geometry [90]

Table 2.1 Summary of the state of the art for the AM of structural parts

	Technology	Advantages	Limitations
Metallic AM	LPBF (SLM & DMLS)	• Very high stiffness & strength • Isotropic properties • Geometric freedom	• High structural weight • Expensive
	BMD (FFF-based)	• High stiffness & strength • Quasi-isotropic properties • More economical than LPBF	• High structural weight • Shrinkage during sintering • Limited overhangs & bridging
SFRP-AM	SLS	• Higher stiffness than neat polymers • Quasi-isotropic properties • Low structural weight • Geometric freedom	• Low strength • Expensive
	FFF	• Higher stiffness than neat polymers • Low structural weight • Economical	• Low strength • Anisotropic properties • Limited overhangs & bridging
CFRP-AM	Towpreg based	• Highest stiffness & strength • Printing process simplicity • Low structural weight	• Anisotropic properties • Limited geometric freedom • Limited material choices • Expensive feedstock
	In-line impregnation	• Very high stiffness & strength • Material choice freedom • Low structural weight	• Anisotropic properties • Very limited geometric freedom • Required bulky tooling restricting motion systems
	In-situ impregnation co-extrusion	• High stiffness & strength • Material choice freedom • Low structural weight	• Anisotropic properties • Very limited geometric freedom • No cutting mechanisms • Limited impregnation

2.3 Current robotic AM infrastructure

2.3.1 Infrastructure components

The laboratory for multi-scale mechanics (LM^2) recently developed a tailor-made 6-axis robot infrastructure used for AM of composites, mainly via FFF and direct-ink writing (DIW) methods. Presented in Figure 2.9, the general LM^2 robotic AM infrastructure is shared by many ongoing projects and is mainly composed of the industrial robot (FANUC M20iB/25, FANUC Canada Ltd., Canada), its motion controller (R30iB Plus, FANUC, Canada), the custom large area heated bed and the printheads. The robot and its controller act as a motion system which moves the printheads but aren't able to directly control them. For this reason, a secondary printhead controller is used, changing according to each project's printhead requirements.

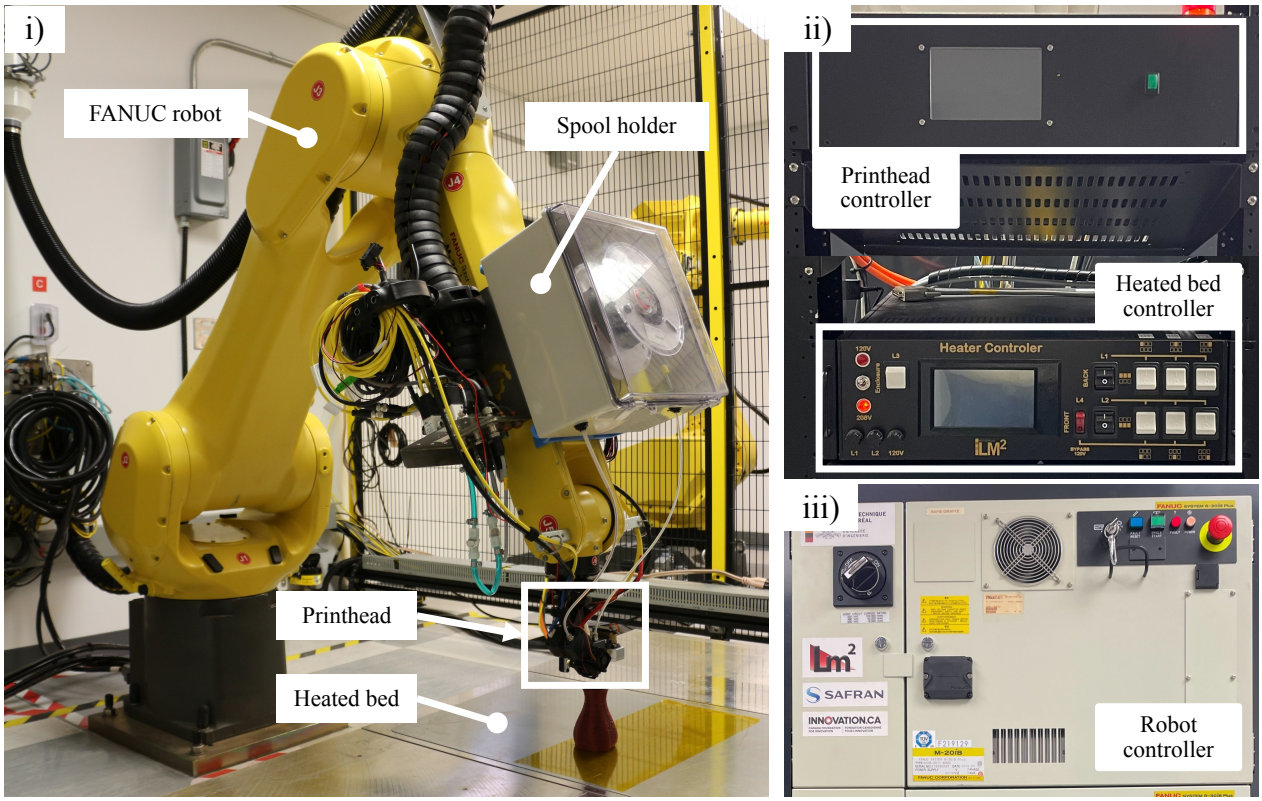

Figure 2.9 **Photograph of the general LM^2 robotic AM infrastructure**, composed of (i) an industrial robot using a printhead on the heated bed, (ii) a printhead controller and a heated bed controller, and (iii) a R30iB Plus robot motion controller connected to the industrial robot

The printing bed is composed of three large aluminum plates that are positioned together to form a single large surface. They are covered by a single steel sheet maintained in place by

magnets. This sheet can be changed between projects depending on the substrate needed. The bed is heated by six resistive heaters individually controlled by a Duet3D mainboard (Duet 3 6HC, Duet3D, UK).

2.3.2 Printing workflow

Among other uses (e.g., DIW, optical 3D scanning of large parts), the pre-existing robotic AM infrastructure was designed to work with conventional FFF printheads. Figure 2.10 presents the pre-existing workflow used for FFF printing with the LM^2 robotic AM infrastructure. The desired 3D geometries are first converted to meshes and imported as standard triangle language (.stl) files into a commercial slicing software (Simplify 3D, version 4.1.2). This software then slices the geometry into discrete layers and generates a printing path to manufacture it based on the user's inputs. It is then exported as a G-code file (i.e., machine instructions common for commercial cartesian 3D printer) including both the specific machine movements required to make the part (i.e., XYZ positions controlling cartesian motion systems) and the printing instructions (e.g., extrusion commands, heating temperatures, cooling fan speeds). This file is then imported into a robotic simulation software (RoboDK, ver. 5.4.1), which reads the motion instructions and solves the inverse kinematic problem, correlating the cartesian positions with their respective joint positions required to control a 6-axis robot. Because the robot controller cannot interpret G-code instructions, the resulting robot positions are added to *Karel* (.ls) programs (i.e., FANUC proprietary file format) [12]. A custom Python post-processor also identifies the printing instructions from the G-code and includes them as character strings outputs in the *Karel* programs. The robot controller then sends the strings in real time to the printhead controller, which is programmed to interpret and execute them. The robotic simulation and robot controller workflow was mainly done by the former PhD student, Jean-François Chauvette [45], while the work on the universal printhead controller was done by former M.Sc. student, Paul Gregorio [91]. Although functional for previous projects, the current infrastructure and workflow are not suitable for CFRP-AM without modifications.

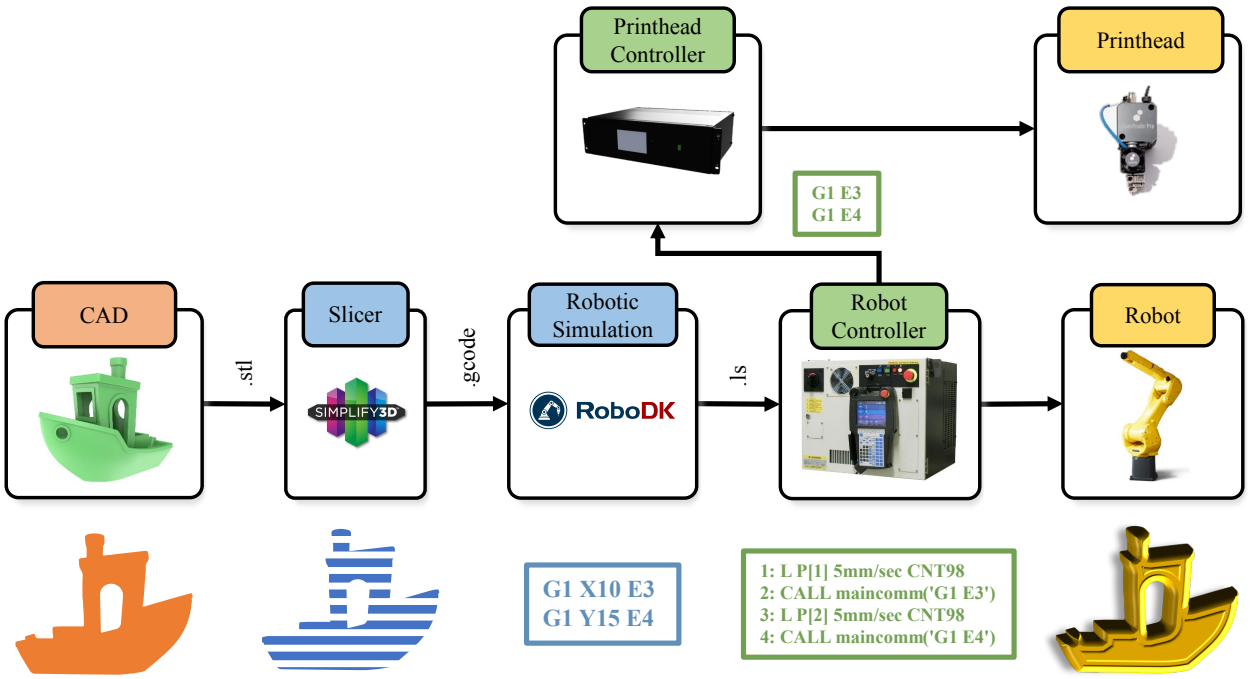

Figure 2.10 **Printing workflow for FFF using the robotic AM infrastructure.** Adapted from Paul Gregorio [91]

CHAPTER 3 SCOPE AND METHODOLOGY

3.1 Scope and problem definition

The LM^2 has worked extensively on SFRP-AM using the FFF method. One of the research topics explored is the use of a 6-axis industrial FANUC robot as a large-scale AM platform. Non-planar slicing algorithms and infrastructures were also developed to use the additional degrees of freedom (DoF) available on the robot to control the orientation of fiber reinforcements of FFF-manufactured components (i.e., 6 DoF on the robot as opposed to 3 DoF on a cartesian 3D printer) and enable conformal 3D printing on curved surfaces.

However, the mechanical properties of SFRPs, mainly their strength, are much lower than those of other material classes like metals and CFRPs. The use of CFRP-AM could help achieve significantly higher mechanical properties, but the shape complexity is currently heavily limited, especially when compared to more mature manufacturing methods like FFF. The requirement for proprietary materials also limits the use of commercially available CFRP-AM machines. The need for manufacturing methods capable of producing high complexity geometries using non-specific materials while retaining the ultra-high mechanical properties of CFRPs therefore arises.

3.1.1 Objective 1: Develop a continuous fiber-reinforced composite additive manufacturing infrastructure compatible with non-specific reinforced thermoplastics material feedstock

CFRPs being even more anisotropic than their SFRPs counterparts, the possibility of combining the advancements made to non-planar AM with the outcome of this project would contribute to better orient the fibers along the directions in which the external mechanical loadings are most important [77, 92, 93]. To facilitate the long-term vision of non-planar CFRP-AM, this project aims to integrate a CFRP-AM printhead to the robot.

To do so, the FANUC robot was equipped with a continuous fiber co-extrusion printhead prototype made by Dyze Design. The reliance on proprietary materials being one of the limiting factors of current commercial CFRP-AM machines, the co-extrusion printhead was chosen for its capacity to use non-specific materials. The infrastructure was first tested using neat polylactic acid (PLA) filaments and continuous glass fiber tows. The co-extruded continuous glass fiber-reinforced PLA composite is defined as PLA-CGF. The capacity to use different materials was then validated by using continuous carbon fiber tows and a short

carbon fiber-reinforced PLA filament, aiming to produce a multi-scale co-extruded composite defined as PLA-SCCF. This second material combination was used for the rest of the project and is the object of O2 and O3.

3.1.2 Objective 2: Evaluate the tensile mechanical properties of flat unidirectional composite beams manufactured using the developed infrastructure

The motivation to implement CFRP-AM on the robot instead of SFRP-AM mainly comes from their typically much higher mechanical properties. The ultimate tensile strength and stiffness along the principal direction were therefore tested for flat unidirectional beams manufactured in PLA-SCCF. The results were compared to the mechanical properties of short carbon fiber-reinforced PLA dogbones manufactured via FFF. To situate the composite in regard to other AM methods available, the PLA-SCCF mechanical properties were also compared to other CFRP-AM methods, as well as SLM 3D printed metals.

3.1.3 Objective 3: Demonstrate the capacity of the developed infrastructure to manufacture complex geometries

Two main demonstrators were used to evaluate the capacity of producing complex geometries using the developed infrastructure. The first one is a single-walled vase designed to include overhangs, which are known to be hard to print [15,16,79]. The printed vase is scanned using an optical 3D scanner, and the resulting point cloud is compared to the reference computer-aided design (CAD) model to quantify the geometrical fidelity. Optical microscopy is also used to identify printing defects on the outer surface of the vase.

The second demonstrator is a sandwich panel composed of co-extruded PLA-SCCF skins and a mono-extruded core (i.e., simple extrusion of the polymer matrix using the printhead, similar to FFF). This demonstrator is manufactured in a single manufacturing step to showcase the capacity of switching between different extrusion modes and to highlight the possibilities offered by the co-extrusion approach. Optical microscopy and a micro-computerized tomography (μCT) scan were used to identify surface defects and the internal voids and defects. The μCT scan was also used to produce a surface mesh of the sandwich panel and compare it to the reference CAD model to evaluate its geometrical fidelity.

3.2 Relation to submitted paper

Chapter 4 provides a detailed description of the proposed infrastructure and O1 results. Chapter 5 presents the article, which summarizes this infrastructure and explains the print-

ing workflow used throughout the project. It also details the printing parameters used for the samples produced for O2 and O3, as well as the specific methodology used for the testing conducted. The article then discusses the mechanical properties and geometric fidelity achieved for O2 and O3. It was submitted to the *Composites Part B: Engineering* journal on September 22nd, 2025.

CHAPTER 4 DEVELOPMENT OF A CO-EXTRUSION INFRASTRUCTURE COMPATIBLE WITH NON-SPECIFIC MATERIAL FEEDSTOCK

4.1 CFRP-AM infrastructure

4.1.1 Co-extrusion infrastructure

Two main strategies were identified to enable CFRP-AM using the FANUC robot: a tailor-made printhead developed and manufactured specifically for our systems, or a commercially available printhead that would be integrated into the robot infrastructure. To reduce the design and manufacturing time, we chose to integrate a preexisting printhead into the robot infrastructures, leaving time and resources to O2 and O3. Most commercially available printheads were, however, designed to exclusively function on specific machines (e.g., Markforged Mark 2 printer or Anisoprint Composer A4 printer), making them difficult to integrate into the robot infrastructure. These printheads are also designed to use their respective proprietary material feedstocks only, significantly limiting the research possibilities. A co-extrusion prototype made by Dyze Design (i.e., a Montreal-based printhead manufacturer) and designed to combine generic thermoplastic polyurethane (TPU) coated continuous fiber tows with 1.75 mm FFF thermoplastic filaments was identified as an exception to these limitations. The Dyze Design printhead prototype was used for this project.

Figure 4.1a shows the printhead prototype provided by Dyze Design, which features a single heated nozzle, two individual extruders and a cutting mechanism. This universal configuration featured holes for fastening to a motion system and cables coming out of the motors, heaters and thermocouples, which needed to be implemented into the adapted additive manufacturing infrastructure. While some parts of the infrastructure presented in Section 2.3, such as the heated bed, could be used as-is, most of them required modifications (e.g., the printhead controllers and material feeding systems were not compatible with co-extrusion). The wiring for the power and control of the printhead also needed to be made entirely. Since conventional slicing software are made to work with single extrusion processes for FFF machines, custom post-processing software also needs to be developed to include cutting instructions and manage multiple simultaneous extrusions.

Figure 4.1b shows the adapted robotic infrastructure, with an adapter between the robot and the printhead that was designed to hold the printhead at a 90° angle, positioning the robot above the heated bed in the configuration offering the most freedom of motion. To maintain

its stiffness despite the heat released by the bed and enable rapid prototyping of multiple iterations, the adapter was 3D printed in short carbon fiber-reinforced polyphthalamide (PPA-CF, Bambu lab, China) using a desktop FFF printer (X1E, Bambu lab, China).

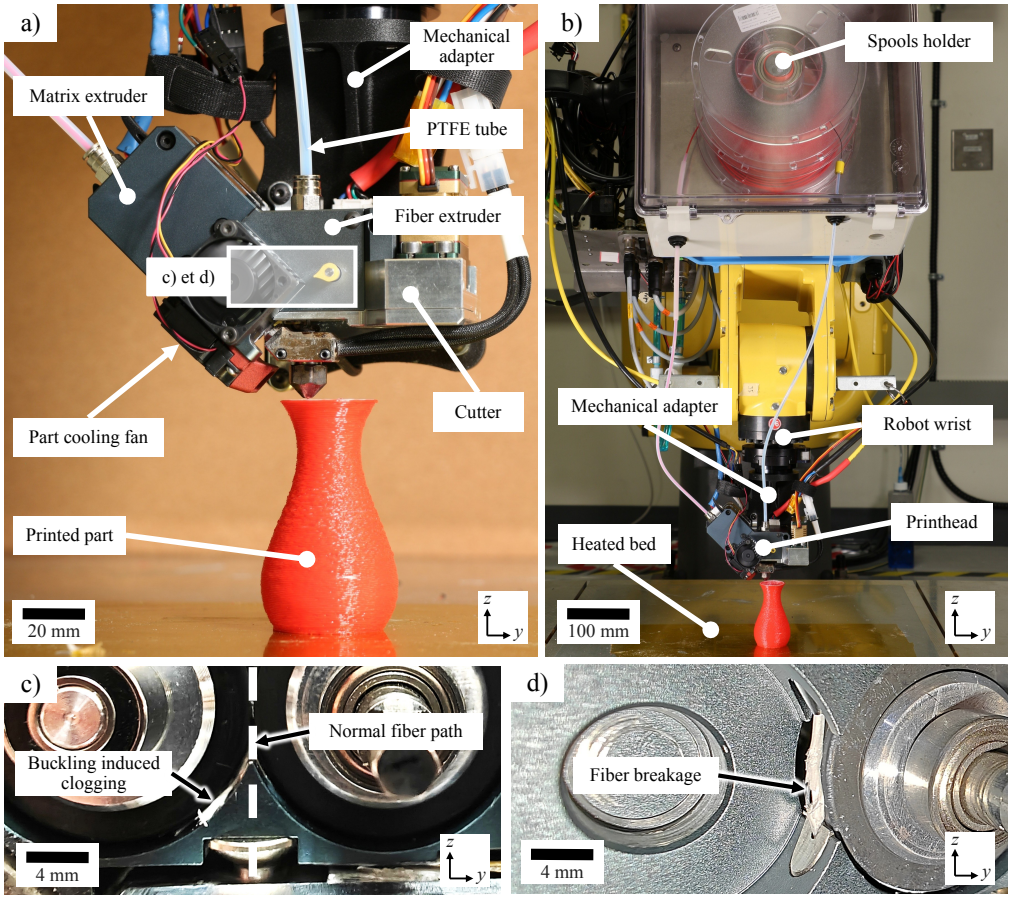

Figure 4.1 **Co-extrusion infrastructure components.** a) Close-up view of the co-extrusion printhead. b) Photograph of the co-extrusion robotic infrastructure. c) Photograph of the clogged printhead resulting from the buckling issue. d) Photograph of a broken fiber tow which caused a failed print. To properly show the fiber tow, one of the extruder gears was removed for the picture

While functional for basic extrusion, improvements needed to be made to the printhead to improve printing quality and remedy issues encountered during preliminary printing tests. Table 4.1 presents a summary of issues encountered and solutions implemented. Although initially able to manufacture simple flat structures, the first attempts to make 3D structures were unsuccessful. Unsupported features like overhangs and bridging sections needed to be extruded extremely slowly (i.e., slower than ∼120 mm/min) to allow sufficient cooling of the matrix; otherwise, this would result in excessive sagging defects and poor dimensional stability. To adjust the cooling rate during printing, a cooling fan was added, and a cover

was designed and 3D printed to directly blow air at the nozzle exit.

Preliminary tests also identified frequent clogging as a main issue, often leading to printing failure. Figure 4.1c shows the clogging inside the printhead, where the fiber tow deviated from its normal path. These clogs were due to excessively tight tolerances between the fiber tows and the capillary tube leading them to the nozzle. The molten TPU coating accumulated between the fibers and the inner wall of the tube, resulting in increased friction, which placed the fiber tows in compression and led to local fiber buckling in the printhead. Once buckled, the fiber tows departed from their normal path and became rolled up around the extruder gears, causing the clogging. Larger capillary tube inner diameters of 0.052 in (1.32 mm) were found to prevent the TPU accumulations and fiber buckling.

Table 4.1 Summary of the co-extrusion issues fixed and the respective modifications or additions made to the infrastructure

Issues observed	**Related component**	**Modifications & Additions**
Sagging and poor dimensional stability	Part cooling fan	Part cooling fan integrated and cover designed
Frequent clogging	Fiber capillary tube	Fiber tow specific tube sets with larger ID
Inconsistent extruded fiber lengths	Fiber extruder gears	Gears material changed and pressure between gears increased
Fiber resistance exceeding the extruder pulling capacity	Spools holder	Low friction spools holder designed
Premature edge wear	Fiber cutting blade	TiN coated HSS blades with reduced blade angle manufactured

During further testing, it was discovered that the extruded fiber length was inconsistent. Not always matching the associated displacement, it was a source of defects, often leading to print failure. If the extruded fibers are much shorter than the travelled distance, it leads to tension buildup resulting in *in-situ* fiber breakage. Figure 4.1d shows an example of a broken fiber tow caused by this issue. While still in its normal path, the fiber tow showed present significant

damage, which caused the extrusion to cease. This issue was caused by occasional slipping between the rubber extrusion gears and the fiber tows. First, the pressure between the rubber gears (Buna-N, McMaster Carr., USA) of the fiber extruder was increased by changing their outer diameter. Their material was also changed (Fluoroelastomer, Viton, USA) to increase friction with the fibers. While reducing the fiber slipping frequency, occasional defects were still present due to excessive friction in the spool holding system, causing the tension in the fibers entering the printhead to exceed the pulling capacity of the extruder. To remedy this issue, a low-friction spool holding system was designed. Two spools (i.e., one for the fibers and one for the matrix filament) are mounted on ball bearings and separated by a thrust ball bearing to reduce the friction regardless of the orientation. The fibers are then fed to the printhead through a low-friction polytetrafluoroethylene (PTFE) tube.

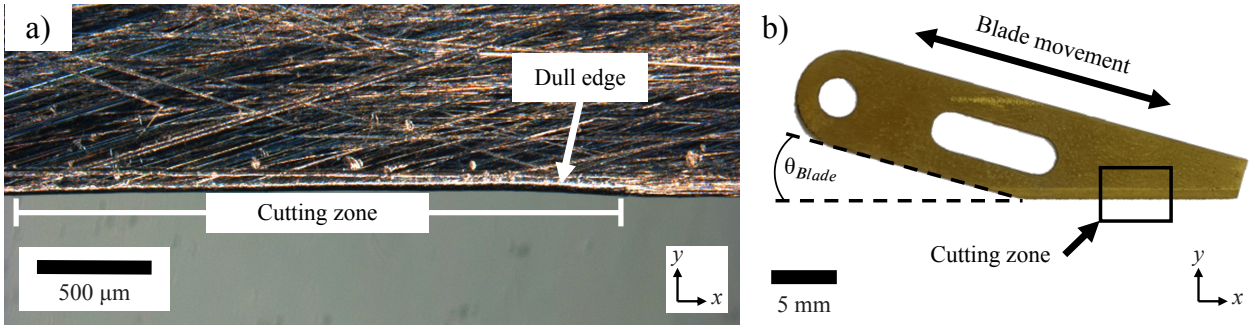

Figure 4.2 **Fiber cutting blades.** a) Optical microscope image of a used HS blade edge, after cutting carbon fibers. b) Photograph of the redesigned TiN-coated blade identifying the blade angle, the fiber cutting zone and the blade movement direction

Another issue identified was the cutting mechanism only partially cutting fiber tows after carbon fiber reinforced prints. Not previously tested for this purpose by Dyze Design, the hardened steel (HS) blade was showing excessive wear due to the carbon fibers being strongly abrasive. Figure 4.2a shows a microscope image of a worn-out blade edge, causing partially cut fiber tows. The cutting zone presents significant wear, which prevents it from reliably cutting the fibers. To remedy this issue, new blades were manufactured in high-speed steel (HSS) and coated with titanium nitride (TiN) to improve the abrasion resistance. Figure 4.2b shows a photograph of these blades. The angle between the blade edge and the movement direction (θ_{blade}) was also reduced to increase the length of the cutting zone and further distribute the wear along the edge. These improvements increased the blade lifetime enough to prevent frequent replacements, which initially were too frequent to allow the manufacturing of the larger structures presented in Chapter 5 (i.e., a vase and a sandwich panel). The replacements were also time-consuming due to the need for a recalibration after each blade change.

4.1.2 Printhead controller

The Universal Printhead Controller, made by former graduate student [91], was the most customizable among the various printhead controllers available. Table 4.2 presents a summary of the controller features already designed as well as the features that needed to be implemented. Figure 4.3a presents the printhead controller components. It was built using a Duet3D mainboard (Duet 3 6HC, Duet3D, UK). Made for standard FFF 3D printers, this board includes inputs for thermocouples and outputs made to power and control stepper motors used in FFF extruders (e.g., National Electrical Manufacturers Association (NEMA) 17 motors) and direct current (DC) motors used for cooling fans. It also features an Ethernet connection used to communicate with a computer and an RS-232 port to receive instructions from the robot controller. Because the power required for large heaters is more than the power provided by the board, it was connected to solid-state relays to control nozzle heaters using an external power source. Since it was originally made to control a single stepper motor and actuate a heater, an external variable power supply needed to be added to power the servomotor of the cutting mechanism.

Table 4.2 Universal controller features already designed and features implemented for co-extrusion

Main feature	**Pre-existing [91]**	**Newly implemented**
Thermocouple reading	Single reading	-
Nozzle heater	Single heater	-
Extruder stepper motors	Single extruder	Dual co-extruder
Cutting servomotors	-	Single cutter
Cooling fans DC motors	-	Part cooling

Figure 4.3b shows the connector backplate of the controller. It features connections for the various printhead components, to the robot and to the laboratory computer. Additional wiring needed to be made to power and control the added servomotor, an additional stepper motor (i.e., used for the co-extrusion of fibers), as well as a DC motor (i.e., used for the cooling fans). The configuration of the controller being made to control a single extruder, an additional stepper motor needed to be defined. Co-extrusion control variables needed to be implemented to manage the ratio between the fibers and the polymer matrix. The logic required to manage the cooling fan was added, and the heater was left unchanged.

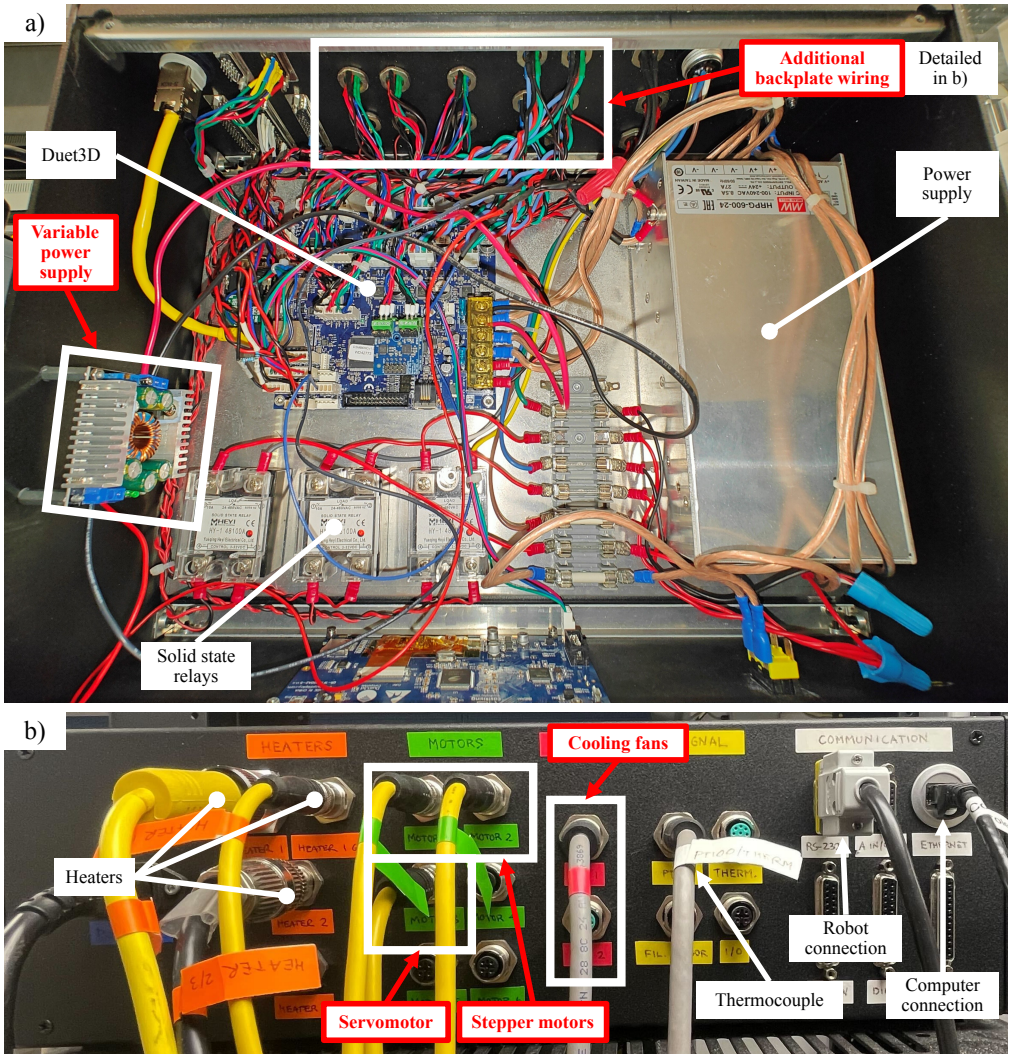

Figure 4.3 **Printhead controller components.** a) Photograph of the inside components of the controller. b) Photograph of the connector backplate of the controller. The modifications are marked in red

4.1.3 Printing workflow

The robotic printing workflow presented in Section 2.3 was adapted to the needs of this project. Mainly, an additional step was added to include cutting behaviours at the end of the infill patterns. Figure 4.4a presents the side of a part printed with aligned rectilinear infill and in a single continuous path without cutting. The absence of cuts in the sharp direction change between each extrusion path causes the fiber tows to be dragged instead of being placed properly. This dragging results in visible defects on the edge of the part. Figure 4.4b presents the same part but with added cuts between the several changes in direction of the infill pattern. While some inconsistent fiber lengths mentioned in Section 4.1.1 are

visible, the addition of cutting instructions eliminates the fiber-dragging effect and reduces the defects present at the edge of the printed part.

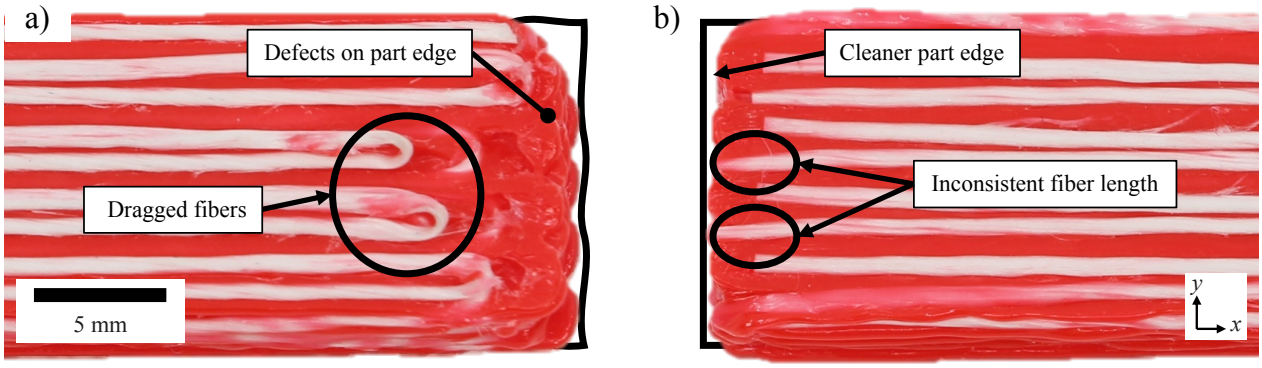

Figure 4.4 **Infill pattern fiber cutting.** a) Photograph of the side of a PLA-CGF sample printed without cutting instructions. The dragged fibers are identified, and the black contour shows the resulting defects on the part edge. b) Photograph of the side of a PLA-CGF sample printed with cutting instructions. The smoother contour shows a reduction of the edge defects

Figure 4.5 presents the adapted co-extrusion workflow. The CAD model is first exported as a triangular mesh, which is imported into the same slicing software described in Section 2.3 to create the printing path instructions. The main workflow addition is that the G-code files made using the commercial slicer are sent to the G-code post-processor, highlighted in red, which adapts them to co-extrusion manufacturing. These new G-code files are then imported into the robotic simulation software, to which macros were added to interpret the new cutting and co-extrusion instructions. The Python post-processor was also adapted to generate a *Karel* program including the new cutting and extrusion instructions to be sent to the printhead controller. The robot and printhead controllers then simultaneously send the movement and extrusion instructions when the print is launched.

Appendix A shows the graphical user interface (GUI) of the G-code post-processor and details the different steps of the G-code modification process. The software first interprets the G-code file and presents it to the user via a 3D viewer. Table 4.3 presents the user inputs used by the software. The minimum angle defines the threshold at which sharp direction changes require fiber discontinuities. Points requiring fiber discontinuities are identified, and the tool path is segmented where corresponding cuts are required. Cuts are also added systematically before every layer change, movements with no extrusion, and when changing from co-extrusion to matrix-only extrusion. Because fibers are passing through the cutting mechanism a certain distance before exiting the nozzle tip, cuts need to be made before the

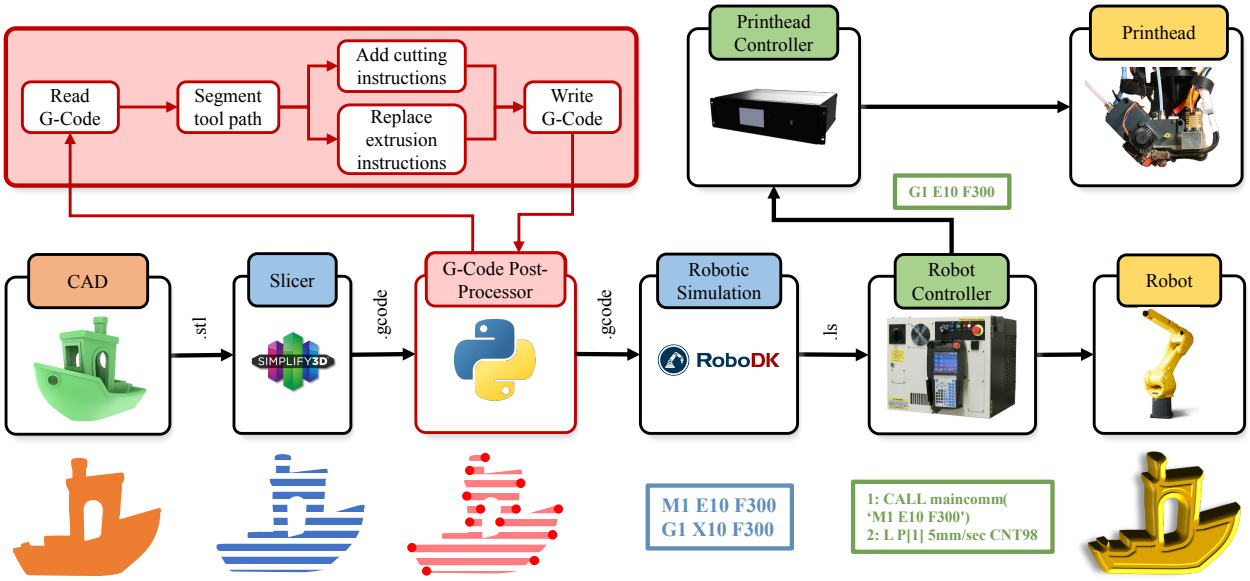

Figure 4.5 **Robotic AM infrastructure co-extrusion workflow.** The main addition from the FFF workflow is the G-code post-processor, for which details are highlighted in red

required discontinuities in order to have matching fibers and tool path endpoints. The cutting distance defines this distance and usually corresponds to the length of the heated nozzle. To avoid cutting a fiber tow multiple times before it exits the nozzle, which was found to cause clogging issues, a post-cut limit distance is defined. Smaller segments (e.g, the small lateral displacements between infill paths) are replaced by travel movements.

A new tool path including these additional points is then created, and cutting instructions are added. Since they need to be sent to the printhead controller while motion instructions are managed by the robot controller, the extrusion instructions are added as separate instructions (i.e., which isn't the case for typical FFF G-codes). An interactive 3D visualization file is created for the user to validate the result before printing, and the resulting G-code file is saved, ready to be sent to the robotic simulation software.

4.2 Preliminary printing results

4.2.1 Feedstock limitations

Although the co-extrusion printhead enables more material combinations than towpreg solutions relying on a single proprietary material feedstock, it still has limitations. To facilitate material handling and make the manufacturing process more reliable, the fiber tows used require a coating like the TPU one on the fiber tows used in this work, which are commercially

Table 4.3 Co-extrusion g-code post-processor user inputs definitions

User input	**Definition**	**Default value**
Minimum angle [°]	Smallest angle for which a fiber can be continuous. Values equal to or lower than this threshold will result in discontinuities.	90
Cutting distance [mm]	Distance before discontinuities at which cuts are made. Corresponds to the distance between the nozzle tip and the cutter.	30
Post-cut limit distance [mm]	Segments between two cuts that are shorter than this value are considered unprintable. They are converted to travel movements.	2

available as reinforcement for belt manufacturing. The preliminary tests using the printhead identified that the coating choice needs to be chemically compatible with the polymer matrix to prevent failure due to a debonding between an unmixed coating and the matrix.

It was also found that the softening temperature range of the coating needed to match the matrix required printing temperature. If the coating is too viscous at the printing temperature (i.e., the melting temperature (T_m) of the coating is much higher than the T_m of the matrix), the coating will act as a barrier preventing impregnation of the fibers by the matrix during printing, resulting in poor mechanical properties. If, however, the coating is not viscous enough (i.e., T_m of the coating is much lower than the T_m of the matrix), the fiber tow will de-bundle and lead to a clogging of the printhead, resulting in a print failure. For the results presented in this study, the TPU used for coating by our fiber provider offered a good thermal and chemical compatibility with our PLA filaments.

4.2.2 PLA-CGF demonstrators

To validate that the integration of the printhead prototype to the robotic AM infrastructure we did was working properly, initial tests were conducted using the same materials as the ones used by Dyze Design during their product development phase (i.e., neat PLA matrix reinforced with TPU-coated glass fiber tows). It also allowed for a comparison with their preliminary results and evaluated whether issues were resulting from the infrastructure integration or were inherent to the prototype design.

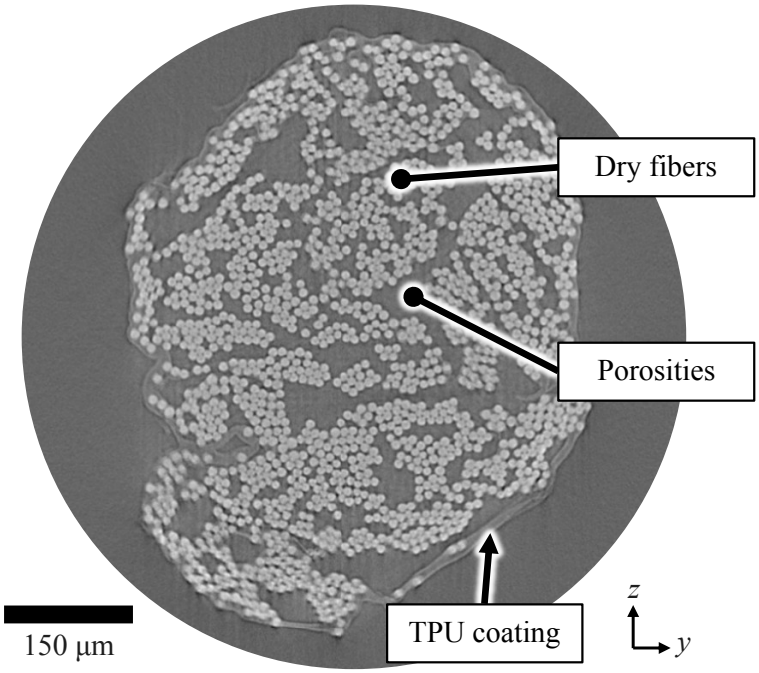

Figure 4.6 **Microtomography slice of the TPU coated continuous glass fiber tows used**

Prior to printing, the glass fiber tows were observed using microtomography imaging to assess their initial composition. Figure 4.6 presents a representative microtomography slice of the TPU-coated continuous glass fiber tows used as reinforcement. It shows the TPU coating is mainly located in the peripheral region of the tow and does not significantly impregnate the fibers. Most of the volume of the tow is composed of dry fibers and porosities. Visual inspection of the fibers also identified that several dry spots were present on the outer surface of the tows. Since TPU represents only a small fraction of the initial material, the TPU volume fraction of the manufactured composite is expected to be extremely low. The very limited impregnation observed in the raw tows also indicates that most of the impregnation observed after printing, discussed further in Chapter 5, results from the *in-situ* manufacturing process.

Two PLA-CGF demonstrators were imagined, each evaluating specific manufacturing capabilities. Figure 4.7a presents the first demonstrator, which is a single-walled hollow vase. This 60×60×100 mm (X×Y×Z) vase features inwards and outwards slopes of up to 28°, a 1.4 mm wall thickness and a radius of curvature of 10 mm, corresponding to the best quantified result found in the literature [79]. Being among the first parts printed, it was designed to be printable without the need for a cutting mechanism by continuously increasing the height of the printhead in a helicoid movement. This allowed us to adjust the extrusion ratio before

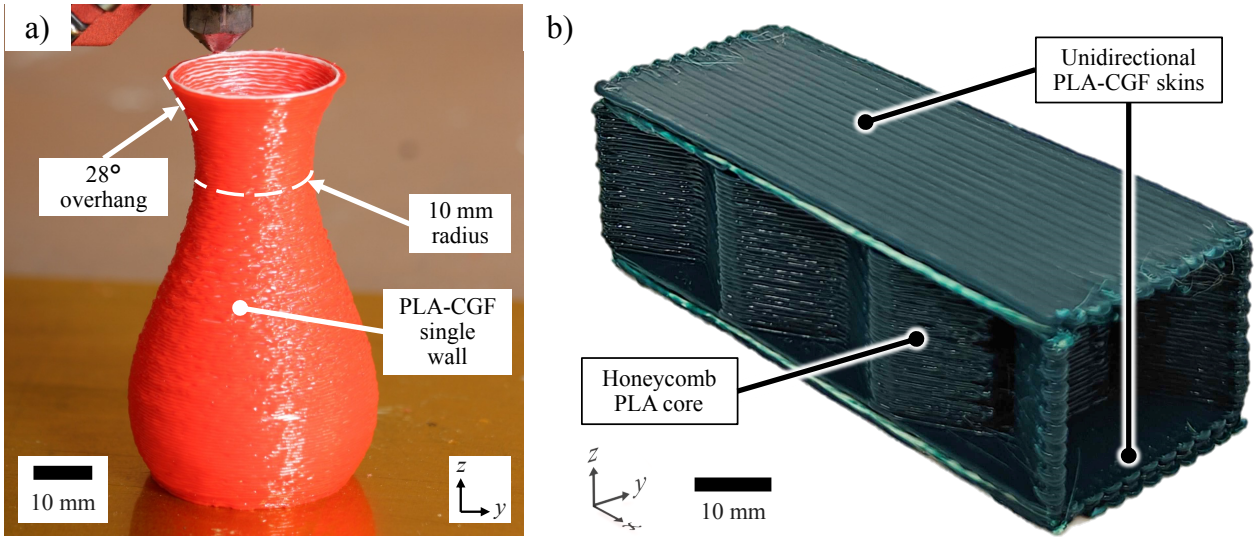

Figure 4.7 **Co-extruded PLA-CGF demonstrator parts.** a) Photograph of the co-extruded PLA-CGF single-walled vase. b) Photograph of the continuous glass fiber-reinforced sandwich panel made in a single manufacturing step. The colour change between the demonstrators is cosmetic and due to a change between two PLA matrix spools

adding the cutting behaviour.

The second demonstrator was an 80×30×24 mm sandwich panel with a honeycomb core, presented in Figure 4.7b. It was printed in a single manufacturing step, with 1.8 mm thick skins reinforced with unidirectional glass fiber tows and a core printed using neat PLA only. This verified the ability to alternate between extrusion modes as well as the reliability of the cutting mechanism. It also tested the ability to manufacture the top skin in mid-air without a supporting structure.

Other materials were then tested to demonstrate the capacity of the infrastructure to use different feedstocks (i.e., short fiber-reinforced matrix and continuous carbon fiber tows). This second material combination is used during the realization of **O2** and **O3** and is discussed in Chapter 5.

CHAPTER 5 ARTICLE 1: HIGH-PERFORMANCE AND GEOMETRICALLY COMPLEX PARTS VIA CO-EXTRUSION ADDITIVE MANUFACTURING OF MULTI-SCALE CONTINUOUS CARBON FIBER-REINFORCED THERMOPLASTIC COMPOSITES

Mathieu Verville[a], Daniel Therriault[a]

[a]Laboratory for Multiscale Mechanics (LM^2), Department of Mechanical Engineering, Polytechnique Montréal, Montréal, Québec H3T 1J4, Canada

Submitted to Composites Part B: Engineering Journal on September 22nd, 2025; Revised October 31st, 2025; Accepted for publication November 5th, 2025; Published January 28th, 2026.

Available online at: `https://doi.org/10.1016/j.compositesb.2025.113179`.

5.1 Abstract

Continuous Fiber-Reinforced Polymer Additive Manufacturing (CFRP-AM) often aims to significantly improve the mechanical properties of 3D printed parts. In this paper, we develop a CFRP-AM infrastructure able to print continuous carbon fiber-reinforced polylactic acid (PLA-SCCF) via co-extrusion (i.e., extrusion-based *in-situ* combination of the thermoplastic matrix and the continuous fibers reinforcement). This infrastructure uses a 6-axis robot to move a co-extrusion printhead over a heated printing bed, and is controlled using a custom-made slicing process. A curved thin-walled vase and a multi-material sandwich panel are made in a single manufacturing step to demonstrate the capabilities of the proposed infrastructure. Their geometrical fidelity is measured and their deviations from the reference model are both <1%. Micro-computerized tomography scans (μCT) are performed to evaluate the micro and meso-structure of printed composite flat beams. Continuous fibers represent ∼44 vol.% (∼58 wt.%) of the composite while voids and porosities represent 0.4 vol.% and 7.9 vol.%, respectively. The ultimate tensile strength (UTS) and stiffness along the principal direction (E_1) are tested for unidirectional flat beams and measured at 854 MPa and 29.5 GPa, representing 16× and 6.4× increases when compared to a part reinforced with ∼3.4 vol.% (∼4.5 wt.%) short carbon fibers only, of an average aspect ratio of ∼21. The developed co-extrusion CFRP-AM infrastructure could find applications in load-bearing applications where complex part geometries are a requirement, such as the automotive and aerospace industries.

Keywords: Additive manufacturing, Co-extrusion, Material-extrusion, Carbon fibers, Fiber-reinforced thermoplastic, Composite

5.2 Introduction

Additive Manufacturing (AM) is a group of processes that fabricates three-dimensional (3D) geometries layer-by-layer. It enables rapid prototyping by eliminating the need for expensive moulds and reducing material waste, but also allows the manufacturing of complex geometries otherwise hard to achieve using injection moulding or machining. Material-Extrusion Additive Manufacturing (MEAM) methods, mainly Fused Filament Fabrication (FFF), have become a widely used process due to its low costs, high speeds when compared to most AM methods, and its compatibility with a wide range of neat thermoplastics [9]. FFF is also compatible with short fiber-reinforced thermoplastics for improved mechanical properties compared with the neat polymers [10–14], especially the material stiffness, which can be increased up to 6.3× the values of the neat polymer [14]. Although higher than those of neat polymers, the achieved mechanical properties (e.g., tensile modulus (E) of 8.6 GPa for high-performance short carbon fiber-reinforced polyetherimide [66]) are still much lower than metals or continuous fiber-reinforced composites (e.g., E_1 of 70 GPa for aluminum 6061 [52] and 33 GPa for continuous carbon fiber-reinforced polyetheretherketone [94]). The freedom of design associated with AM also has limitations in FFF methods, mainly regarding bridging areas (i.e., unsupported sections where material is printed in mid-air). While able to manufacture these features (e.g., top skin of sandwich panels), the FFF printed results usually present associated defects in those bridging regions, such as increased porosities (e.g., reaching up to 12.7 vol.% in the top skin) [17] and visible sagging [15–17].

Continuous Fiber-Reinforced Polymer Additive Manufacturing (CFRP-AM) has been increasingly researched as a means to improve the mechanical properties of the discontinuous fiber reinforcement used in FFF [18–21]. The use of pre-consolidated continuous fiber-reinforced 3D-printing filaments has been extensively researched as a solution [22–25]. Recent efforts have focused on increasing the fiber content [26] (i.e., fiber volume factions ranging between 11 vol.% and 58 vol.%) [27], fiber impregnation [22,28–30] and voids reduction [24] to improve mechanical properties. These solutions, however, require specialized and expansive equipment (e.g., pultrusion lines) or the use of proprietary materials (e.g., Markforged continuous carbon fiber) [31, 32], significantly limiting the material selection and increasing the material costs [33]. Other *in-situ* consolidation solutions (i.e., methods combining dry continuous fibers and neat polymers during the printing process) have been researched to remedy this issue, such as co-extrusion AM [34–37]. The increased material selection is, however,

typically accompanied by limited mechanical properties when compared to pre-consolidated methods (i.e., ultimate tensile strength (UTS) ranging from 216 MPa [95] to 986 MPa [32]), mainly due to the limited impregnation and fiber content achievable using those methods (i.e., fiber volume fractions between 9 vol.% and 38 vol.% [27] for *in-situ* impregnation via simple co-extrusion, and up to 50.2 vol.% for more complex *in-situ* impregnation methods that use additional impregnation devices such as rollers and pin systems [29]).

The recent advances made towards increased mechanical properties have also come to the detriment of part complexity. The lack of *in-situ* fiber cutting mechanisms to enable travel movements or the need for complex consolidation systems currently limit most solutions to manufacturing small and 2D flat beams (i.e., constant cross-section through the thickness). The geometric characteristics of single printed beads were evaluated [79], but, to the best of our knowledge, the macroscopic geometric fidelity (i.e., the deviation between the surface of the intended geometry and the manufactured one) of complex 3D shapes has not yet been evaluated nor quantified for CFRP-AM methods. This research aims to address the limited geometric complexity of the current CFRP-AM systems while maintaining high mechanical properties. While sandwich structures and bridging properties of towpreg CFRP-AM were researched [96–98], the use of *in-situ* impregnation CFRP-AM for these structures still has to be evaluated. The apparent bending properties were measured, but the micro-structure of CFRP-AM sandwich panels has yet to be evaluated.

In this paper, we have developed a co-extrusion CFRP-AM process using non-specialized material feedstock (i.e., not proprietary or tailor-made pre-consolidated filaments) and capable of producing curved 3D parts (i.e., changing cross-section through the thickness) featuring overhangs and bridging sections comparable to FFF methods. Two demonstrators, which are a curved vase and a sandwich panel, are presented, and their geometric fidelity is quantified (i.e. deviation from the desired model). Both the strength and stiffness are measured and compared to a FFF benchmark and to published properties achieved using other CFRP-AM methods.

5.3 Materials and methods

5.3.1 Materials

The thermoplastic matrix used in this study is a 1.75 mm short carbon fiber-reinforced polylactic acid (PLA) filament (PLA-CF, Bambu Lab, China), referenced as PLA-SCF in this paper. It is co-extruded with reinforcing continuous carbon fiber Z-twisted 6k tows coated with a thin layer of thermoplastic polyurethane (TPU), at an ignition loss of 20.9

wt.%. The tows have an apparent diameter of ∼770 μm, a linear density of 520 g/1000 m and a twist of 84 tpm (CFR07-400X 1/0-80Z, Nippon Sheet Glass Co., Japan). The resulting co-extruded multiscale composite is PLA reinforced with short and continuous carbon fibers and will be referenced as PLA-SCCF in this paper.

5.3.2 AM platform using a 6-axis robot

The co-extrusion system was mounted on a 6-degree-of-freedom (6-DoF) industrial robot (FANUC M20iB/25, FANUC Canada Ltd., Canada), as presented in Figure 5.1a. A filament spool system is used to feed the matrix filament to the printhead using a 4 mm diameter polytetrafluoroethylene (PTFE) tube. A low-friction spooling system was designed using axial and radial ball bearings and mounted on the robot arm to reduce the tension in the fibers. The 3D printed parts are deposited on a 1420×760 mm heated bed located at the base of the robot and covered with a polyimide adhesive film (Kapton, Dupont, USA).

5.3.3 Continuous fibers co-extrusion AM

Figure 5.1b shows the co-extrusion system used (Co-Extrusion Prototype, Dyze Design, Canada), composed of two extrusion systems individually controlled by two stepper motors (DyzeXtruder Pro, Dyze Design, Canada). As illustrated in the schematic of the printhead presented in Figure 5.1c, the first one is equipped with metallic serrated gears and is used to push a standard 1.75 mm thermoplastic filament into the hot zone of the printing nozzle. The second extrusion system is equipped with smooth fluoroelastomer rubber gears designed to push polymer-coated continuous fiber tows in the printing nozzle without damaging them. A titanium nitride (TiN) coated blade (World Backyard, China) actuated by a servo-motor (HBL833, Kpower Technology Co., China) is placed between the fiber extruder and the printing nozzle to cut the fibers, enabling *stop-and-go* movements as well as switching between co-extrusion and mono-extrusion printing modes.

The hotend is heated to melt the thermoplastic filament, and a 304 stainless steel capillary tube (McMaster Carr., USA) is located in the middle of the melt zone to feed the continuous fiber tows up to the nozzle tip. The fibers are then mixed with the molten thermoplastic before exiting the 1.2 mm diameter printing nozzle. The TPU coating on the fiber tow is also heated in the capillary tube and exits the nozzle tip in a molten state. The co-extruded resulting composite is then deposited layer-by-layer on the 3D printing bed to manufacture the desired geometry. Figure 5.1d shows the nozzle tip where the coated fibers are mixed with the thermoplastic matrix. The rounded sides of the heated nozzle are used to apply pressure to the extruded composite while the thermoplastic is still hot, acting as consolidation

pressure, then a part cooling fan ensures shape retention and limits de-consolidation.

While printing, the fiber tows are held in tension between the previously printed, cooled-down matrix and the extrusion gears, which pull the fibers and place them on the top of the deposited beads. This leaves a matrix-rich region at the bottom [99] to be pushed on the previously deposited layer and improve impregnation. To prevent having under-impregnated fibers on the last printed layer, a 0.15 mm mono-extruded layer of matrix is added at the end to further embed the fibers inside the host matrix.

5.3.4 CFRP-AM process

Slicing G-code post-processing

A computer-aided design (CAD) software is used to model the desired 3D geometry and generate a mesh saved as a standard triangle language (.STL) file. This file is sent to a commercial slicing software (Simplify 3D, version 4.1.2) to slice the geometry into layers and generate the infill patterns according to the desired extrusion width, height and infill orientations. The resulting tool path is saved as a G-code file with instructions for the nozzle temperature, cooling fans speed and extrusion.

Since commercial software is made to generate conventional FFF G-codes, a custom post-processing tool was developed in Python to adapt the generated codes for CFRP-AM. The co-extrusion paths are first modified to add cutting instructions before every travel movement in a way that the fiber discontinuities correspond to the end-of-path locations. The extrusion distances calculated by the slicing software are then replaced by the corresponding printhead movement distances to prevent fiber damage caused by a mismatch between the extrusion and printhead movement [100]. A mixing ratio is defined as the ratio between the matrix extrusion rate and the fiber reinforcement extrusion rate and is iteratively calibrated for each set of printing parameters before being added. The resulting program is saved as a new G-code file.

Printhead and robot motion controllers

The G-code files generated using the method presented in Section 5.3.4 are converted to *Karel* programs (i.e., FANUC proprietary file format) using a robotic simulation software (RoboDK, ver. 5.4.1) by solving the inverse kinematic problem for each instruction. To be used with the robot, the resulting *Karel* program is sent to the robot motion controller (R30iB Plus, FANUC, Canada), which executes the movement instructions and send simultaneous G-code instructions to the custom printhead controller built with a Duet3D mainboard (Duet

3 6HC, Duet3D, UK). This controller interprets the G-code instructions and controls the hotend heaters, the cooling fan motors, the servo-motor actuating the cutter and the stepper motors for the two extrusion systems.

5.3.5 Printing parameters

Flat beams

Rectangular tensile testing samples of 250×15×1.35 mm and micro computerized tomography-scan (μCT) samples of 100×7×2.95 mm were printed unidirectionally at 100% infill using the same printing parameters to accurately correlate the mechanical behaviour and the microstructure. The parameters, for which a summary is presented in Table 5.1, were chosen to increase the impregnation of the fiber tows and the fiber volume content, while keeping the material easily printable [75]. The nozzle temperature was increased from 180°C by increments of 5°C, aiming to reduce the viscosity of the matrix and facilitate the impregnation mechanism. The maximum temperature achieved was 275°C. Higher temperatures rendered the TPU coating of the fiber tows too liquid, leading to an increased clogging frequency caused by the fiber tows buckling in the nozzle andT preventing reliable manufacturing. The layer height was reduced from 0.8 mm by increments of 0.05 mm, aiming to increase the consolidation pressure. The lowest layer height value identified producing a consistent and repeatable extrusion was 0.4 mm. The layer width was reduced from 1.8 mm by increments of 0.1 mm, aiming to maximize the fiber content. The lowest layer width value achieving a consistent extrusion was 1.4 mm. The cooling fan speed was increased from 0 to 100% by increments of 25%. The maximum value was found to improve the surface finish and the geometric stability by reducing sagging and partial collapsing. The print head displacement speed was increased by increments of 60 mm/min from 180 to 300 mm/min, corresponding to the fastest value allowing a consistent extrusion. The printing bed temperature was set for PLA at 60°C.

To compare the co-extruded samples with an FFF reference, similar samples were manufactured on a commercial FFF 3D printer (X1E, Bambu Lab, China) using the largest nozzle diameter available of 0.8 mm. The layer height, layer width, bed temperature and cooling fan speed used were the same as the ones presented in Table 5.1. The nozzle temperature and the printing speed were managed automatically by the printer, with the temperature ranging between 210°C and 250°C and the speed matching a maximum volumetric flow-rate of 18 mm^3/s, as recommended by the filament manufacturer [101].

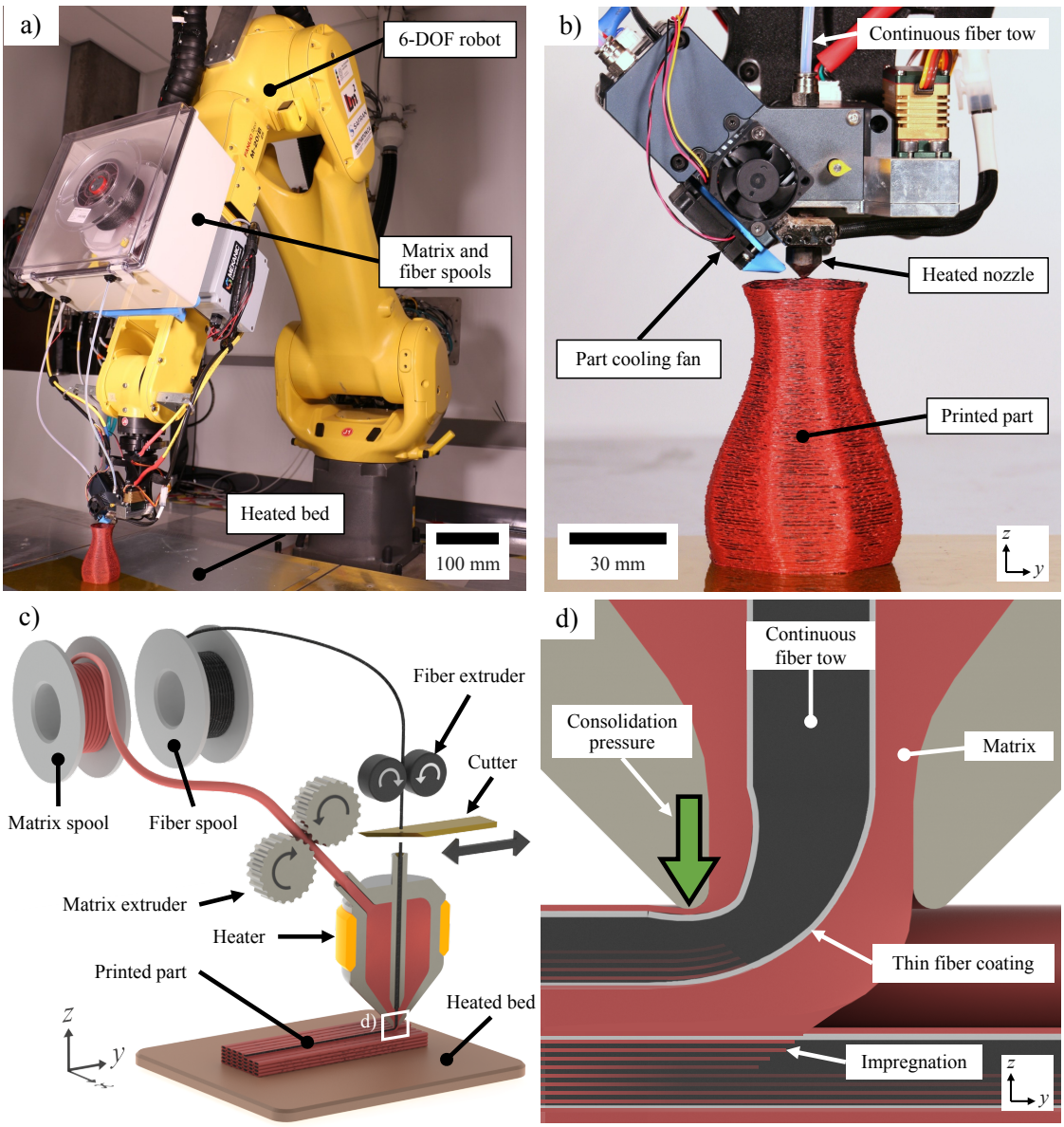

Figure 5.1 **Co-extrusion manufacturing infrastructure and printhead.** a) Photograph of the 6-DOF robot with the co-extrusion printhead and spools holder installed. b) Photograph of the co-extrusion print head printing a single-walled hollow vase. c) Schematic of the co-extrusion printhead with a thermoplastic filament extrusion system, a continuous fiber tow extrusion system, a fiber cutting mechanism, a heated co-extrusion nozzle and a heated printing bed. d) Schematic of the nozzle tip region showing the consolidation pressure and the co-extruded composite structure.

Single-walled hollow vase

For the vase, the layer height was set to 0.6 mm to increase the volumetric flow rate and reduce the printing time by ∼30%. The first two layers were printed at 0° and 90° to make

a solid base, then, the single-walled structure was sliced in vase mode, which increases the z position in a continuous helicoid pattern instead of discrete steps every layer. The other printing parameters were kept identical to the flat beams and are also found in Table 5.1.

Sandwich panel

The sandwich panel was printed using co-extrusion for the load-bearing skins and mono-extrusion for the core, reducing the printing time by ∼50% compared to a panel fully printed using co-extrusion. The mono-extruded PLA-SCF core is composed of a sinusoidal pattern with a 1.4 mm wall thickness and a 25 mm cell width. The co-extruded PLA-SCCF skins are 0.95 mm thick and printed in a unidirectional pattern. A single contour is added to serve as an anchor point for the tool paths starting in mid-air. The skins were printed using the same parameters as the tensile samples. The core was printed in PLA-SCF at a temperature of 240°C and using a higher volumetric flow rate of 1008 mm^3/min. The layer height was 0.6 mm and the layer width 1.4 mm. A printing speed of 1200 mm/min was identified as the fastest value, resulting in a consistent extrusion width. Fans' speed and bed temperature were kept identical to the flat beam printing.

5.3.6 Characterization

Optical microscope imaging

The outer surfaces of the vase and sandwich panel were observed using a digital optical microscope (Keyence VHX-7000, Keyence Corporation, Canada). Dimension measurements were made using the manufacturer's XY measurement module (VHX-H3M3, Keyence Corporation, Canada).

Optical 3D scanner

The single-walled hollow vase was scanned using an optical 3D scanner (Atos Q 12M, Zeiss, Germany). The resulting point cloud was reconstructed as a mesh and exported as an .STL file using the manufacturer's software (INSPECT Optical 3D 2025, Zeiss, Germany). The signed distances (positive or negative according to the normal of the surface) between the CAD and its scanned reconstruction (CAD to Mesh or C2M) were then computed and visualized using an open source point cloud editing software (CloudCompare, version 2.13.2).

Table 5.1 Summary of the main printing parameters used for the flat tensile beams (T), the flat μCT beams (CT), the single-walled hollow vase, and the sandwich panel skins (S) and core (C).

Printing parameter	**Flat beam**	**Vase**	**Sandwich panel**
Nozzle temperature [°C]	275	275	275 (**S**), 240 (**C**)
Bed temperature [°C]	60	60	60
Layer height [mm]	0.4	0.6	0.4 (**S**), 0.6 (**C**)
Layer width [mm]	1.4	1.4	1.4
Cooling fan speed [%]	100	100	100
Printing speed [mm/min]	300	300	300 (**S**), 1200 (**C**)
Printing time [min]	20 (**T**), 12 (**CT**)	120	195
Dimensions [mm]	250×15×1.35 (**T**), 100×7×2.95 (**CT**)	72×72×120	150×75×20

μCT-scan

Some printed flat beam samples were observed using a μCT scanner (Xradia 520 Versa, Zeiss, Canada) at an acceleration voltage of 70 kV, a power of 6 W and using 4501 projections. Two different voxel sizes of 4.8 μm and 0.708 μm were used to observe the meso-scale and the micro-scale, respectively. The sandwich panel was scanned at an acceleration voltage of 80 kV, a power of 7 W and using 2401 projections. The voxel size for the panel was 55 μm.

The 3D reconstructions were performed using the manufacturer's software (Scout-and-Scan, Zeiss, Germany) without the noise reduction filters. A scientific image processing and 3D analysis software (Dragonfly 3D World, Comet Technologies, Canada) was used to segment the reconstructed volumes into different regions of interest. The segmentation was done using a pre-trained deep learning model (Generic U-Net dl-5 ifc-64 slice-3, Comet Technologies, Canada) that was retrained on a user-painted input of our specific dataset to segment each slice. The fibers were analyzed using an open source fiber segmentation plugin (i.e., OpenFiberSeg) [102] and the angle and length of each fiber were measured. For the sandwich panel, a triangular surface mesh was extracted from the segmented regions of interest. The mesh was then compared with the CAD model, and the C2M signed distances were computed using CloudCompare.

5.3.7 Mechanical tensile testing

Samples were manufactured and tested in accordance with the ASTM D3039 standard [103]. Seven rectangular unidirectional tensile samples were printed in PLA-SCCF using the parameters described in Section 5.3.5. Garolite G-10/FR4 tabs (McMaster-Carr, USA) of 70×15×1.59 mm were cut using a round saw and sanded at a bevel angle of 5°. They were glued to the extremities of the samples with a toughened epoxy glue (3M DP460NS, 3M, USA), then cured at room temperature for 24 h.

Tensile testing was performed using an MTS Insight (Eden Prairie, USA) electromechanical testing machine with a 50 kN load cell, serrated jaws, and a 50 mm gage length extensometer (MTS 634.25F-25, China). To avoid any slipping during testing, the extensometer was attached to the top surface of the sample since it had a slightly higher surface roughness. To reduce the effects of the jaws' pressure in the measurements, a small portion of the tabs was left outside of the jaws, and the extensometer was vertically centred on the sample. The crosshead displacement rate was 2 mm/min. The stiffness was computed in the linear region between 1000 μm/m and 3000 μm/m strain values, and a secondary stiffness was computed between 13 000 μm/m and 15 000 μm/m strain values for materials exhibiting a bilinear behaviour.

To serve as a benchmark, five Type 1 dogbone samples were printed in PLA-SCF and in accordance with ASTM D638 [104]. Mechanical testing was done using the same equipment and testing parameters as the PLA-SCCF samples.

5.4 Results and discussion

5.4.1 μCT multi-scale characterization

Meso-scale segmentation

Figure 5.2a shows a representative slice of a meso-scale scan done on a PLA-SCCF rectangular beam sample, where four printed layers and the fiber tow stacking can be observed. The continuous fiber tows are easily discernible, containing most of the porosity, while the matrix-rich regions between them present very little. They are consistently distributed throughout the thickness, indicating good process repeatability in the z direction. The upper region of each fiber tow presents the strongest impregnation, corresponding to the matrix that was pushed in while printing the following layer. Inversely, the bottom region of the tows presents more porosity, with some tows containing dry zones. Of the three extruded widths visible, two seem well aligned vertically, but one presents a repeated staggered pattern leading to an

increased width and the formation of larger matrix-rich regions. Due to the repeatability of the pattern and its independence from the materials and printing parameters, we believe it is explained by the hysteresis of the robot motion system in certain joint configurations that creates a mismatch between the target position and the actual position of the tool center point (TCP). Reducing this effect by improving the robot kinematics, by using a different motion system or by using a different stacking sequence could allow a more uniform layer width and reduce the matrix-rich regions, which could lead to better transverse properties and lower anisotropy.

Figure 5.2b presents a segmentation of the reconstructed slice highlighting fiber tows (yellow), matrix-rich regions (red) and inter-layer voids (blue). With an average size of 4.33×10^{-5} mm^3, these inter-layer voids (i.e., meso-scale inter-filament defects which excludes the micro-scale porosity contained within the fiber tows) are very small compared to the frequent FFF porous diamond patterns [13, 105] and represent here only 0.42 ± 0.02 vol.% of the scanned volume. This is explained by the very high layer width to height ratio of $LW/LH = 3.5$ when compared to conventional FFF methods (i.e., typically near 2). The nozzle temperature used was also very high for the PLA matrix (i.e., 55°C above the usual FFF printing temperature of 220°C), to lower its viscosity and facilitate the gap filling while printing. Figure 5.2c shows a 3D rendering of the unidirectional continuous fiber tows (yellow) and the in-between matrix-rich regions (red). The four layers of the scanned region are also specified, and the layer thickness is uniform. The continuous tows are well aligned with the part's longitudinal direction, and their stacking pattern is continuous throughout the length, indicating good process repeatability in the printing direction. This repeatability, however, leads to the formation of continuous matrix-rich regions in the gaps of the stacking pattern, representing a continuous weak area and a potential failure zone.

Micro-scale segmentation

Since the 4.8 μm pixel size of the meso-scale scan was too large to distinguish the individual carbon fibers of $\sim$7 μm in diameter, additional micro-scale scans were performed with a smaller pixel size of 0.708 μm. Figure 5.2d presents a slice of the 3D reconstruction for a scan of the inter-tow region. These scans were segmented as shown in Figure 5.2e to highlight individual carbon fibers (yellow), porosities present within the fiber tows (grey) and the PLA matrix (red). The continuous carbon fibers ($V_{ccf,tow}$) represent 75.7 ± 0.1 vol.% of the tows, while the matrix ($V_{m,tow}$) represent 9.4 ± 0.1 vol.% and the porosities 14.9 ± 0.1 vol.%. Figure 5.2e shows that the impregnated fibers are mainly, but not exclusively, located near the perimeter of the tows. The continuous fiber tows used were coated, but not impregnated,

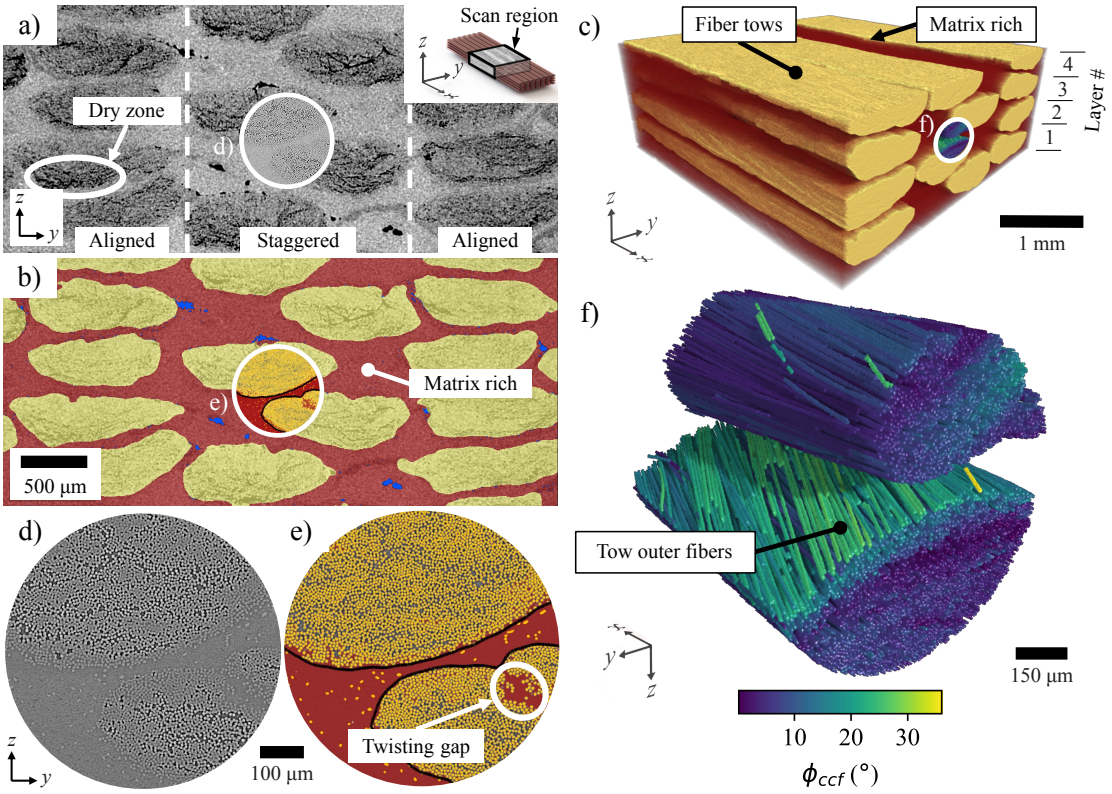

Figure 5.2 **Micro tomography imaging of a PLA-SCCF printed sample.** a) Representative slice of the meso-scale reconstruction of multiple printed layers. The inset corner indicates the section of the sample that was scanned. b) Meso-scale segmentation of multiple printed layers, differentiating fiber tows regions (yellow), matrix-rich regions (red) and inter-layer voids (blue). c) Rendered 3D reconstruction of the μCT-scan highlighting the segmented fiber tow regions (yellow) showing their unidirectional alignment. The different layers are identified on the right. d) Representative slice of the micro-scale reconstruction of the inter-tow region. e) Micro-scale segmentation of the inter-tow region identifying the matrix (red), individual fibers (yellow) and porosities (grey). Black lines are separating the fiber tows and matrix-rich regions. f) 3D rendering of the continuous fiber tow region with individual fiber deviations as a colormap, with angles shown between 0 and 35°.

with a TPU resin. Because the coating was superficial (i.e., ~30 μm thickness on the outside of the tows) and not uniform (i.e., many dry spots were observed on the outer surface of the raw material), the impregnation resin located near the perimeter is believed to be a mix of PLA and TPU. Some larger impregnation regions are also present in the gaps created by the twisting of the fiber tows. The resin in these impregnation regions is mainly PLA which was pushed in during printing in the air gaps in the raw material, resulting from the twisting in the tows. To quantify the impregnation mechanism, the degree of impregnation (DI) [106] is

defined as :

$$DI = \frac{V_{m,tow}}{1 - V_{ccf,tow}}. \tag{5.1}$$

The DI value corresponds to the inter-fiber volume occupied by matrix impregnated in the fiber tows, where a $DI = 100\%$ represent a fully impregnated tow and a $DI = 0\%$ a completely dry tow. The DI and its 95% confidence interval ($CI_{95\%}$) are calculated to be $38.7 \pm 0.5\%$ for the PLA-SCCF sample.

For each individual continuous fiber in the tow regions of the micro-scale scans, the deviation angle from the printing direction (ϕ) was computed. Figure 5.2f shows that the most angled continuous fibers (i.e., in green and yellow) are mainly located near the perimeter of the tows, indicating the most impregnated fibers are also the least aligned with the printing direction. The angle and length for each short fiber were also computed. Table 5.2 presents the average values for the continuous and short fibers. The average angle for short fibers (ϕ_{scf}) is $\sim$2.7$\times$ larger than for continuous fibers (ϕ_{ccf}), showing the continuous fibers tend to align much better with the printing direction than short fibers (e.g., with average deviations often as high as 36° for FFF parts [13]), resulting in a better control over the anisotropy.

Multi-scale composition

Table 5.2 presents the effective characteristics as well as the measured fiber characteristics. To represent more accurately the composition of the PLA-SCCF printed parts, the carbon fibers, matrix and porosity volume fractions measured from the micro-scale scans were applied to the corresponding regions in the meso-scale scan to estimate the meso-scale volume fractions. The effective continuous carbon fibers volume fraction (V_{ccf}) of 44.3 vol.% ($\sim$58 wt.%) is a 16% improvement compared to the highest values reported for simple co-extrusion *in-situ* impregnation CFRP-AM [27]. It is also closer to the values reported for towpreg based CFRP-AM (i.e., up to 58 vol.%) [18,27] and more complex *in-situ* impregnation methods (i.e., up to 50.2 vol.%) [29]. The porosities (V_p), mainly located in the fiber tows due to a limited consolidation, represent a much larger portion of the defects than inter-layer voids (V_v). This shows that the main challenge of the proposed method remains the *in-situ* impregnation mechanism. The short fiber volume fraction (V_{scf}) is low and comes from the short fibers contained in the PLA-CF filament used as a matrix. The average fiber length (l), however, is high for AM methods [13, 102], which increases their contribution. The half inter-fiber distance (R) was computed between the centroid of each fiber and the centroid of the closest neighbouring fiber. It is used for Cox's shear lag model and indicates that even for the low short fiber volume fraction (V_{scf}), they are packed closely together in the inter-tow

region. Also presented in Table 5.2, effective characteristics are computed for the PLA-SCF composite printed via FFF, which is characterized by a very high matrix volume fraction (V_m) and the absence of continuous fibers. The porosity volume fraction for the PLA-SCF is also ∼18× lower than for the PLA-SCCF composite, for which the increased value is mainly due to the continuous fiber tows.

These effective meso-scale characteristics, fiber characteristics and the degree of impregnation were used to predict the effective mechanical properties of the printed composite using a modified rule of mixture. It is applicable to obtain the mechanical properties along the longitudinal axis of the continuous fiber tows because the fibers are mainly laid in a unidirectional pattern. First, the effective fiber volume fractions ($V_{ccf,\text{eff}}$) is defined as :

$$V_{ccf,\text{eff}} = V_{ccf} \cdot DI, \tag{5.2}$$

corresponding to the fraction of fibers impregnated by the matrix.

The predicted effective stiffness along the principal direction (E_1) was then calculated to be 40 GPa for the PLA-SCCF beams by using a modified mixing law model. It is composed of a 2D transformation of Eshelby's tensor for the fiber misalignment [39], Cox's shear lag model for the short fiber contributions [42, 43], and assumes only impregnated fibers can transfer load. The stiffness along the principal direction for the continuous fibers (E_{ccf}), the short fibers (E_{scf}) and the PLA matrix (E_m) are 230 GPa (T700S, Toray, France), 230 GPa (T300, Toray, France), and 2.6 GPa [107] respectively :

$$\begin{aligned} E_1 = {} & \left(V_{ccf,\text{eff}} \cdot E_{ccf} \cdot \cos^4 \phi_{ccf}\right) + \\ & \left(V_{scf} \cdot E_{scf} \cdot \eta_l \cdot \cos^4 \phi_{scf}\right) + \\ & \left(V_m \cdot E_m\right). \end{aligned} \tag{5.3}$$

Using a fiber diameter (d_f) of 7 μm (T700S, Toray, France) and shear modulus along the principal direction (G_m) of 0.96 GPa for the PLA matrix [107], the fiber length efficiency factor (η_l) [42, 43] and shear lag parameter (β) [42, 43] are defined as :

$$\eta_l = 1 - \frac{\tanh\left(\beta \cdot l/2\right)}{\beta \cdot l/2} \quad \text{and} \quad \beta = \sqrt{\frac{8 \cdot G_m}{E_f \cdot d_f^2 \cdot \ln\left(\frac{2 \cdot R}{d_f}\right)}}, \tag{5.4}$$

The predicted effective ultimate tensile stress in the principal direction (σ_1) was calculated to be 858 MPa for the PLA-SCCF beams by using a modified mixing law. It is also composed of a 2D transformation of Eshelby tensor for the fiber misalignment [39], Cox's shear lag model

Table 5.2 Effective characteristics calculated at the meso-scale of printed PLA-SCF and PLA-SCCF rectangular beams with a $CI_{95\%}$.

Characteristic	**PLA-SCF**	**PLA-SCCF**
CCF volume fraction (V_{ccf}) [vol.%]	-	44.3 ± 0.3
CCF average deviation from printing direction angle (ϕ_{ccf}) [°]	-	7.4 ± 0.1
SCF volume fraction (V_{scf}) [vol.%]	3.4 ± 0.1	1.5 ± 0.1
SCF average deviation from printing direction angle (ϕ_{scf}) [°]	20.3 ± 1.9	20.3 ± 1.9
SCF average length (l) [μm]	148 ± 11	148 ± 11
SCF average half inter-fiber distance (R) [μm]	16.0 ± 0.7	16.0 ± 0.7
PLA matrix volume fraction (V_m) [vol.%]	96.0 ± 0.1	45.6 ± 0.4
Porosities volume fraction (V_p) [vol.%]	0.44 ± 0.06	7.9 ± 0.1
Inter-layer voids volume fraction (V_v) [vol.%]	0.42 ± 0.02	0.42 ± 0.02
Degree of impregnation of fiber tows (DI) [%]	-	38.7 ± 0.5

for the short fiber contributions [42, 43], and assumes only impregnated fibers can transfer load. The tensile strength along the principal direction for the continuous fibers (σ_{ccf}), the short fibers (σ_{scf}) and for the PLA matrix (σ_m) are 4900 MPa (T700S, Toray, France), 3530 MPa (T300, Toray, France) and 35 MPa [107], respectively :

$$\begin{aligned}\sigma_1 = &\left(V_{ccf,\text{eff}} \cdot \sigma_{ccf} \cdot \cos^2 \phi_{ccf}\right) + \\ &\left(V_{scf} \cdot \sigma_{scf} \cdot \eta_l \cdot \cos^2 \phi_{scf}\right) + \\ &\left(V_m \cdot \sigma_m\right).\end{aligned} \tag{5.5}$$

5.4.2 Mechanical properties characterization

The PLA-SCCF tensile properties were measured on the printed tensile beams using the setup shown in Figure 5.3a. The FFF benchmark PLA-SCF tensile properties were measured using the setup shown in Figure 5.3b. Figure 5.3c shows the resulting stress-strain curves, and Table 5.3 presents the tensile properties and the specific tensile properties for the two material formulations. PLA-SCF samples all exhibited brittle failure. PLA-SCCF samples mostly failed in a LWV (Lateral, <1 width from tab, Various) or AWV (Angled, <1 width from

tab, Various) mode according to ASTM D3039, with some failing in a SMV (Longitudinal splitting, Multiple areas, Various) mode, explaining the variability of the failure points.

Although PLA-SCCF samples exhibit a bilinear behaviour as opposed to PLA-SCF samples, they both exhibit a linear behaviour in the 1000 μm/m to 3000 μm/m strain region used to compute E_1. The secondary stiffness (E_1'), computed for PLA-SCCF samples after the transition point located at ~9000 μm/m, is almost twice the initial E_1 values. This difference is probably due to the fibers being able to move slightly inside the composite when loading first occurs, resulting in a lower initial value of E_1.

The $CI_{95\%}$ is also significantly larger for the PLA-SCCF samples compared to the PLA-SCF samples (i.e., it is hardly distinguishable for the PLA-SCF curves and all the failure points are superposed), showing that the co-extrusion reduces the repeatability of the mechanical properties when compared to FFF.

Figure 5.3d shows a comparison of the UTS and E_1 for PLA-SCF in red, and PLA-SCCF in blue. The full bars represent the measured results, while the hatched bars represent the modified mixing law predictions presented in Section 5.4.1. Compared to PLA-SCF samples, PLA-SCCF samples exhibit a 16.4× increase in measured UTS as well as a 6.4× increase in measured E_1. The UTS of the PLA-SCCF and the E_1 of the PLA-SCF are very close to the model predictions, showing less than 0.5% relative error in both cases. The UTS of the PLA-SCF is 27% lower than the predicted value, which we believe is explained by an absence of contribution from the stress concentrations in the modified mixing law. The E_1 of the PLA-SCCF is 26% lower than the predicted value, while the E_1' is 44% higher than the prediction. It is explained by the fact that the modified mixing law does not account for a bilinear behaviour or movement of the fibers during loading. The strength values are notoriously hard to predict for short fiber-reinforced composites because they depend on many variable factors that interact in complex and unpredictable ways [111, 112]. However, the lack of E_1 correlation between the modified rule of mixture and the measured results for CFRP composites, which is typically more easily predictable, shows that more advanced modelling methods (e.g., multi-scale finite element modelling (FEM)) should be investigated to accurately and reliably predict the stiffness of co-extruded CFRP-AM composites.

Figure 5.3e presents an Ashby diagram comparing the specific UTS and E_1 (i.e., density normalized) of different metals and polymer composites manufactured via AM. Metals manufactured using Selective Laser Melting (SLM), in green, exhibit significantly higher specific stiffnesses than FFF printed polymer-based short fiber-reinforced composites, in red, but only improve marginally on the specific strength. CFRP-AM mostly matches the specific stiffness of metallic SLM, but improves by several orders of magnitude (i.e., 2× to 8×) the specific

Table 5.3 Measured tensile properties and specific tensile properties for the PLA-SCF and PLA-SCCF samples in accordance with ASTM D638 and ASTM D3039 with a $CI_{95\%}$.

	FFF	**CFRP-AM**
Properties	**PLA-SCF**	**PLA-SCCF**
UTS [MPa]	52.1 ± 0.1	853.6 ± 45.8
Specific UTS [MPa · cm^3/g]	42.7 ± 0.1	776 ± 41.6
E_1 [GPa]	4.6 ± 0.1	29.5 ± 1.7
Specific E_1 [GPa · cm^3/g]	3.8 ± 0.1	26.8 ± 1.5
E_1' [GPa]	-	57.6 ± 6.6

UTS. The PLA-SCCF tensile results presented in this study are marked with a blue star and show the highest specific UTS, demonstrating the very good capacity of the methods to produce strong but lightweight components. The specific E_1 doesn't improve over the highest reported values (e.g., values of 63.4 GPa·cm^3/g [29] and 47 GPa·cm^3/g [32] were found), but is comparable to most studies using similar material combinations [28, 110]. However, 3D printed metals are mostly isotropic, and the strong anisotropy of CFRP-AM parts only makes them weaker in the transverse directions. Semi-isotropic layer stacking can be used to mitigate the isotropy, but the resulting properties are more limited [72]. The geometric complexity present in the published work on CFRP-AM [24, 79, 86] is also very limited when compared to both SLM and FFF.

5.4.3 Complex geometries manufacturing

Single-walled hollow vase

To demonstrate the capacity to manufacture complex geometries, a 120 mm tall vase was designed to include overhangs between ± 25°, corners of 135° and 1.4 mm thin walls, as shown on the CAD presented on Figure 5.4a. Figure 5.4b shows the vase printed in PLA-SCCF. To quantify the deviation between the desired geometry (i.e., CAD model) and the printed one, the vase was 3D scanned and the measured point cloud was compared to the CAD model. Figure 5.4c presents the scanned mesh with the colormap representing C2M signed distances. The blue regions, representing negative deviations, are mainly located on the edges of the vase. This behaviour is explained by the fibers being pulled inward when printing in vase mode. The red regions, representing positive deviations, are mainly located on the last layer. This is explained by a slight overextrusion resulting in a vase marginally taller than the CAD

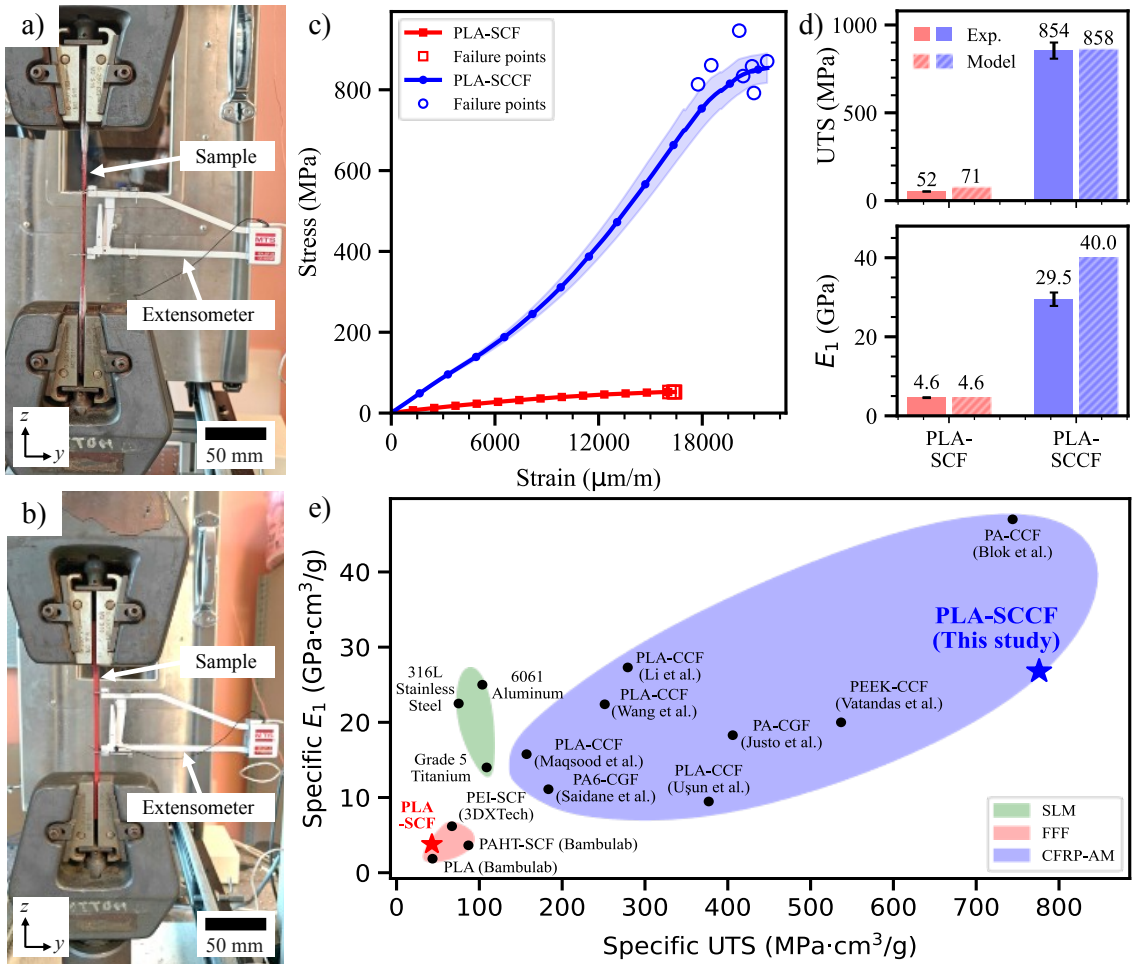

Figure 5.3 **Comparison of tensile testing results.** a) Photograph of the PLA-SCCF tensile testing setup. b) Photograph of the PLA-SCF tensile testing setup. c) Stress-strain curves for tensile tests comparing printed PLA-SCF (red) and PLA-SCCF (blue) samples. E_1 is calculated in the linear region between 1000 μm/m and 3000 μm/m. The $CI_{95\%}$ region is represented by the shadow area near the mean curves. The maximum load at failure for each sample is represented by an open symbol. d) Bar charts comparing the UTS and E_1 for printed PLA-SCF (red) and PLA-SCCF samples (blue) as well as their predictions (hatched). e) Ashby plot of SLM printable metals [52, 53, 108], FFF printable polymer composites [66, 69, 107] and CFRP-AM from the literature [22, 28, 31, 32, 72, 94, 109, 110] comparing their specific UTS and E_1. The PLA-SCF and PLA-SCCF discussed in this study are marked with red and blue stars, respectively.

reference. Figure 5.4d presents the C2M signed distances frequency curve. The average deviation is centred on -0.06 mm and the 90% confidence interval ($CI_{90\%}$), between -0.44 mm and 0.35 mm, only represents ~0.66% of the part height. This small overall deviation shows the capacity of the proposed method to print complex curvatures and thin features while maintaining good dimensional fidelity. The mostly green coloured C2M also suggest a good

capacity to produce overhangs. Figure 5.4e shows a close-up optical microscope image of the vase's lateral surface. The defects observed mainly come from the layer stacking inherent to AM methods (i.e., staircase effect), but some inconstant extrusion (i.e., fluctuating extrusion width) is also visible. The lack of real-time speed synchronization between the robot motion controller and the printhead controller causes a slight mismatch between the robot motion speed and the extrusion speed, which might explain the formation of those defects. A possible improvement would be to manage the extrusion speeds and the robot motion using a single controller.

Sandwich panel

To evaluate the capacity to manufacture bridging features, the ability to produce multi-material parts, and to more closely illustrate engineering applications using the *in-situ* impregnation approach, a sandwich panel was printed. Figure 5.5a shows the sandwich panel stacking configuration and core pattern. To demonstrate the capacity of the method to switch between extrusion modes, it was designed to be printed with a mono-extruded core (red) and co-extruded skins (black lined red). Alternating between the two modes is therefore required to print the panel in a single step. To evaluate the ability to bridge over unsupported regions up to 31 mm, the top skin is printed in mid-air without underlying support material. These features are typically very difficult to print with FFF because the molten material tends to sag and collapse on itself, often resulting in visible defects. Figure 5.5b presents the resulting sandwich panel, 3D printed in a single manufacturing step. The top skin exhibits a very good surface finish and does not present significant large holes, characteristic of bridging areas [15, 16].

Figure 5.5c*i* presents an optical microscope image of two printing paths from the top skin, each containing one continuous fiber tow (black). While the distinction between the continuous fiber tows is clear, the interface between the printed paths is hardly distinguishable. It indicates a good surface void filling after only two bridging layers, resulting in a smooth top surface. This improvement in bridging quality, when compared to FFF methods, is attributed to the presence of continuous fibers being held in tension between the anchoring contours and the nozzle tip, acting as a supporting reinforcement until the polymer matrix cools down. Figure 5.5c*ii* presents a microscope image of the core side wall. The layer thickness is uniform, indicating a consistent extrusion for the mono-extruded core.

A μCT-scan was conducted to assess the material microstructure and printing defects inside the sandwich panel. Figure 5.6a shows a μCT reconstructed slice of the sandwich panel cross section. The core walls present a uniform width of 1.35 ± 0.25 mm, showing the repeatability

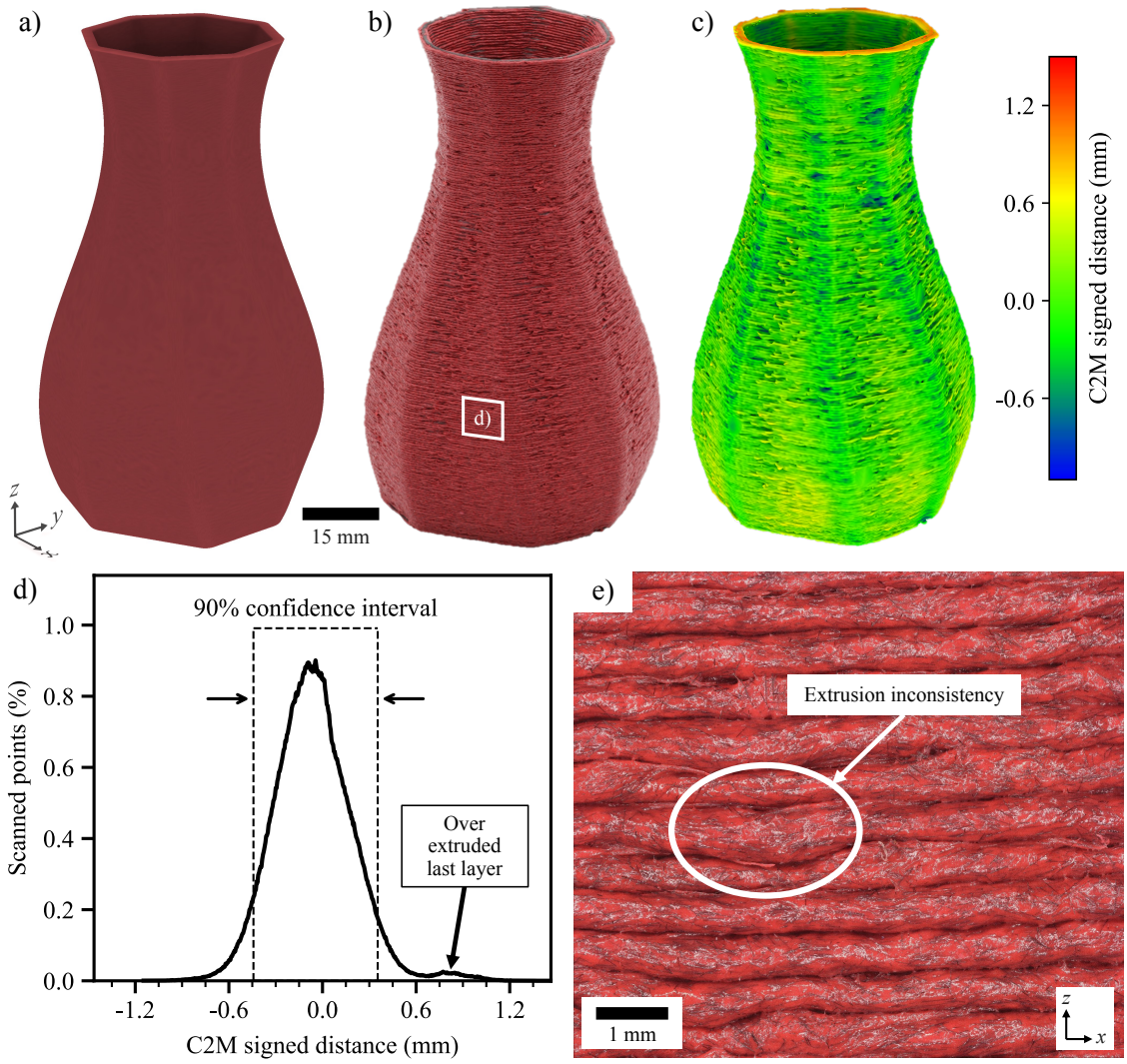

Figure 5.4 **Co-extruded single-walled hollow vase.** a) CAD rendering of the designed vase. b) Photograph of the printed PLA-SCCF single-walled hollow vase. c) Comparison of the 3D scanned surface of the vase to its CAD model. Blue and red regions represent negative (inward) and positive (outward) deviations, respectively, while green regions represent close to null deviations. d) Frequency curve of C2M signed distances of the scanned vase. The average C2M distance is centred on -0.06 mm, with a $CI_{90\%}$ between -0.44 mm and 0.35 mm. e) Optical microscope image of the vase showing the surface finish.

of the mono-extrusion throughout the thickness of the panel. The bottom skin, deposited directly on the printing bed, has a uniform thickness of 0.95 ± 0.14 mm and shows no major defects. The top skin, however, has a thickness of 0.90 ± 0.38 mm, presenting significant bridging defects manifested especially on its lower surface, and visible voids. Figure 5.6b presents a rendered 3D view (in red) and a segmentation of the inter-layer voids (in blue). Due to the bridging defects, inter-layer voids are mainly located on the top skin. Since the

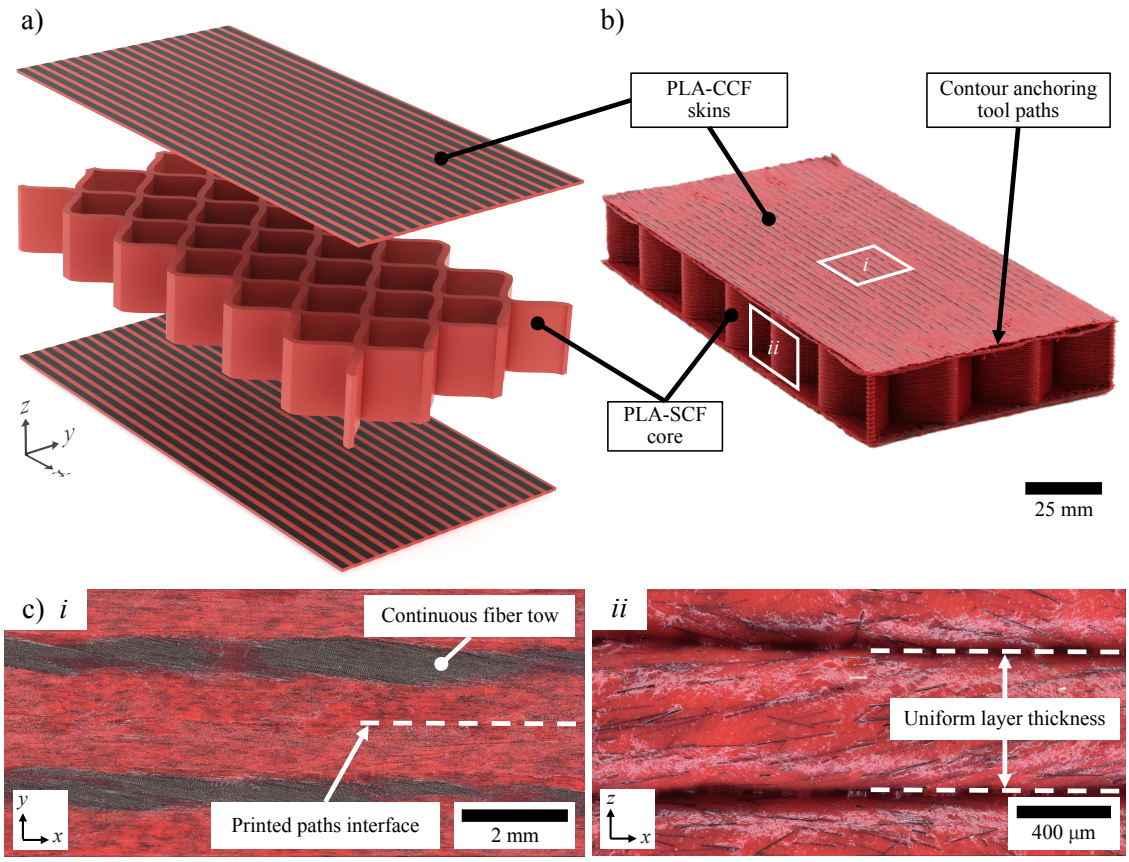

Figure 5.5 **Sandwich panel with co-extruded skins, 3D printed in a single manufacturing step.** a) Schematic of the designed sandwich panel presenting an exploded view of the core and skin regions. b) Photograph of the 3D printed sandwich panel. c) Optical microscope images of (*i*) the top surface and (*ii*) the core lateral wall showing their respective surface finish and fiber reinforcements.

top skin is extruded in mid-air, there is no consolidation pressure forcing the matrix to enter the fiber tows and fill the inter-filament voids, leading to those defects. The top skin presents 7.4 ± 0.2 vol.% of meso-scale inter-layer voids with an average size of 0.17 ± 0.06 mm^3, while the bottom one only present 0.50 ± 0.02 vol.% of meso-scale inter-layer voids with an average size of 0.013 ± 0.001 mm^3. Due to the limited resolution achieved with the scan, these values do not account for the micro-scale porosity observed in the unidirectional beams and further investigation should be conducted to estimate it. Although being 13× higher in the top skin than the bottom one, the measured meso-scale inter-layer void contents are still an improvement over the reported values for bridging using FFF in the literature (i.e., ranging between 1.9 vol.% and 9.4 vol.% for the bottom skin and between 6.2 vol.% and 12.7 vol.% for the top skin [17]).

The panel was also segmented and exported as a surface mesh, then compared to the reference CAD model. Figure 5.6c presents the mesh coloured using the C2M signed distances, where blue regions represent inward deviations and red regions outward deviations. Mainly yellow and green, the skins outer surfaces present small deviations from the reference CAD model, with the $CI_{90\%}$ between -0.06 mm and 0.19 mm. The main defects, in red, are located on the bottom surface of the top skin and are caused by the bridging. Figure 5.6d presents the C2M signed distance frequency curve for the whole panel. The overall $CI_{90\%}$ is between -0.29 mm and 0.26 mm. Representing $\sim$0.36% of the panel length, this deviation shows a high overall geometrical fidelity for the sandwich panel, even when compared to FFF methods (e.g., deviations ranging from $\pm$ 0.2 mm [17] to $\pm$ 1.45 mm [12] for sandwich panels of similar dimensions), that typically achieve significantly higher fidelity for complex geometries. These results are promising, showing the capacity to produce high-quality components of high geometrical complexity (i.e., comparable to FFF manufacturing), while also offering significantly higher mechanical properties.

5.5 Conclusion

A co-extrusion CFRP-AM system was successfully developed, enabling the fabrication of highly strong and geometrically complex components using *in-situ* impregnation of non-specialized material feedstock (i.e., TPU-coated continuous carbon fiber tows and short carbon fiber-reinforced PLA filament). Flat unidirectional PLA-SCCF samples were manufactured and tested. The UTS of 854 MPa prove to be among the best results reported for *in-situ* impregnation CFRP-AM methods. Multiple μCT-scans were performed and used to quantify the micro-structure of the composite. The fiber volume content of 44 vol.% is a 16% improvement over the reported values for *in-situ* impregnation CFRP-AM via simple co-extrusion. The relatively low degree of impregnation of 39%, however, indicates that future work should focus on the integration of *in-situ* consolidation systems, such as rollers or pin systems. Additionally, the inter-layer adhesion and shear properties were not quantified. Further testing, such as out-of-plane tensile testing (i.e., in the Z direction) and short beam shear tests, should be conducted to further understand the 3D mechanical properties of the manufactured composites. A PLA-SCCF single-walled hollow vase was printed and scanned, showing the capability of the system to manufacture overhangs within $\sim$0.66% of the part height. A multi-material sandwich panel was also made in a single manufacturing step, showcasing the capacity to achieve bridging with a good geometrical fidelity despite the skin's thickness of only 0.95 mm. The inter-layer voids, however, increased from 0.5 vol.% in the bottom skin to 7.4 vol.% in the top skin, showing the bridging negative impact on the

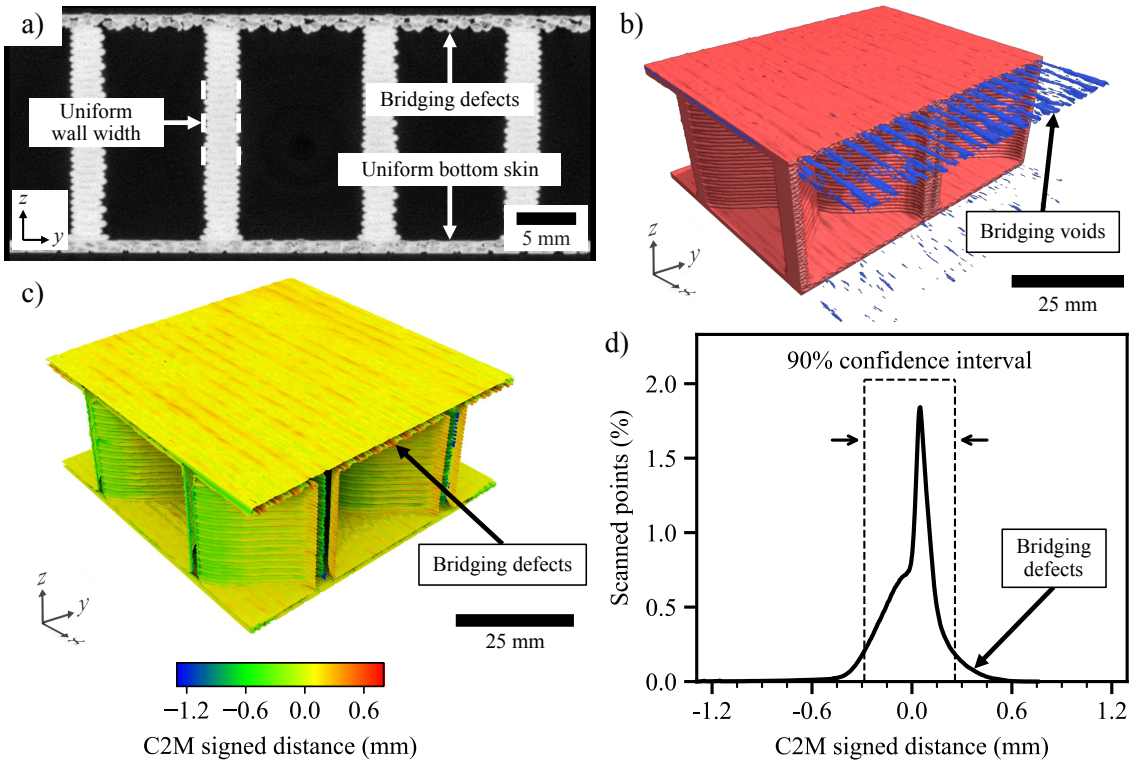

Figure 5.6 **Micro tomography imaging of the sandwich panel with co-extruded skins.** a) μCT reconstruction slice of the sandwich panel cross section. b) Rendered section of the μCT-scan 3D reconstruction (red), highlighting the segmented inter-layer voids (blue). c) Comparison of the segmented tomography scan of the sandwich panel to its CAD model. The mostly yellow surface indicates a good correlation between the scan and expected geometry. d) Frequency curve of C2M signed distances of the printed sandwich panel. The average C2M distance is centred on 0 mm, with a $CI_{90\%}$ between -0.29 mm and 0.26 mm.

microstructure.

The presented mechanical results and geometric demonstrators show promise towards using similar methods to produce complex and lightweight functional components for highly demanding applications, such as the aerospace and automotive industries. The possibility to rely on non-specialized material feedstock and make components in a single manufacturing step also contributes to reducing the costs associated with such fabrication methods. The integration of the proposed method with non-planar AM could further improve the mechanical properties by enabling true 3D tailoring of the anisotropy to the specific needs of the components [77, 92]. Leveraging the material freedom offered by this method, the use of high-temperature thermoplastics matrix materials (e.g., Polyetherketoneketone (PEKK) or Polyetherimide (PEI)) could also be investigated. It could potentially allow the use of such systems in high-temperature applications like engine casings [12]. Finally, the addition

of *in-situ* consolidation mechanism should be investigated further to improve the degree of impregnation achieved [24]. The impact of such mechanisms on the mechanical complexity achievable should also be evaluated.

CHAPTER 6 CONCLUSION AND RECOMMENDATIONS

6.1 Summary of Works

The development of a CFRP-AM infrastructure was presented, integrating a co-extrusion printhead prototype to the LM^2 robotic AM infrastructure and leveraging the use of a tailor-made robotic co-extrusion printing path generation workflow. To demonstrate the capacity to use non-specific material feedstocks, neat and short carbon fiber-reinforced PLA filaments were successfully co-extruded with continuous glass and carbon fiber tows, respectively.

Unidirectional tensile mechanical testing was then conducted for PLA-SCCF samples. The longitudinal modulus was measured at 29.5 GPa, and the strength at 854 MPa. The specific tensile strength along the fiber direction represents an $\sim$8$\times$ increase when compared to metals manufactured by SLM and a $\sim$16$\times$ increase when compared to PLA-SCF manufactured by FFF. To further understand the co-extruded PLA-SCCF composite, multi-scale μCT scans were used to quantify the micro-structure. The continuous fiber volume fraction homogenized to the meso-scale was evaluated at 44 vol.%, while the porosity and voids represented $\sim$8 vol.%.

The ability to manufacture complex geometries was demonstrated by printing two demonstrator parts. The first one is a single-walled vase featuring $\pm$ 25° overhangs, 135° corners and a 1.4 mm wall thickness. The C2M signed distances were computed between an optical scan of the printed result and the reference CAD model. The low deviation, representing only $\sim$0.7% of the part height, shows a good capacity to produce curved geometries. The second demonstrator is a sandwich panel printed in a single manufacturing step, featuring unidirectional continuous fiber reinforcements in the skins and short fiber-reinforced PLA in the core. The top skin is also printed in bridging, which is known to be a difficult feature to manufacture using extrusion-based AM methods. Despite that, the panel C2M signed distances represent $\sim$0.4% of the total length, indicating a good geometrical fidelity. The top skin of the sandwich panel also presented a lower void content than the values reported in the literature for similar parts made by FFF. This improvement is attributed to the presence of continuous fibers acting as tethers.

6.2 Limitations

Although not relying on expensive continuous fiber-reinforced towpreg filaments or large in-line impregnation systems, the proposed co-extrusion infrastructure requires the use of coated

fiber tows to facilitate material processing. The fiber coating also needs to be compatible with the polymer matrix, limiting the material combinations possible.

Furthermore, the impregnation mechanism is limited to the pressure provided by the edge of the nozzle. While unidirectional tensile testing indicates good longitudinal properties, the degree of impregnation (i.e., 39% for PLA-SCCF samples) indicates the presence of dry fibers. The micro-scale images presented in Chapter 5 also highlight the presence of matrix-rich regions caused by the hysteresis of the robot motion system, which could lead to poor transverse properties and an increased material anisotropy.

While improvements over the reported values in the literature for bridging manufacturing were identified for the top skin of the sandwich panel, the void content is 13× higher than in the bottom skin. It indicates a significant increase and shows that while improvements have been made, limitations associated with bridging are still present.

6.3 Future Research

The main research recommendations are as follows :

- Investigate the use of different coating and matrix combinations and their bonding mechanisms.
- Integrate the printhead to the robot heated enclosure [12] by adding water cooling for the electronic components, enabling high temperature CFRP-AM (e.g., polyether ether ketone (PEEK), polyetherimide (PEI) or polyetherketoneketone (PEKK) based matrix).
- Investigate the use of secondary impregnation mechanisms such as a compression roller [24] or a *in-situ* pin system [35] to increase the degree of impregnation.
- Improve the robot payload calibration or change the motion system to increase the fiber volume fraction and decrease the matrix-rich regions by reducing the staggered pattern observed.
- Perform bending mechanical testing on the sandwich panels to quantify the apparent stiffness, the adhesion between the skins and the core and to evaluate the impact of bridging on mechanical properties.
- Integrate multiple larger part cooling fans to improve the geometrical fidelity of overhang and bridging features.

- Increase the heat transfer rate of the hotend by using a longer nozzle to enable higher printing speeds.
- Test the robotic CFRP-AM infrastructure for non-planar AM.

6.4 Project significance

This work highlights the potential of CFRP-AM for producing lightweight structural components in sectors where mass reduction is critical, such as aerospace and automotive. By leveraging the high directional specific stiffness and strength of continuous fiber-reinforced thermoplastic, the proposed method enables the fabrication of parts meeting the mechanical requirements of highly demanding environments without the high density associated with metallic AM. The two demonstrators proposed to show the capacity to produce complex architectures. The process allows control of the fiber orientation at the meso-scale; the fiber placement could be optimized to match loading conditions and further improve performance-to-weight ratios beyond what isotropic materials or traditional composites can offer. The use of a 6-axis motion system also aims to facilitate the future integration of a non-planar AM approach, further controlling the fiber orientation in 3D and increasing the geometric fidelity for conformal AM applications. Finally, the compatibility of the proposed infrastructure with generic feedstock can provide a cost-effective solution and increase the design freedom. The possibility of using a recycled thermoplastic matrix also contributes to the reduction of material waste.

REFERENCES

[1] S. Wegmann, C. Rytka, M. Diaz-Rodenas, V. Werlen, C. Schneeberger, P. Ermanni, B. Caglar, C. Gomez, and V. Michaud, "A life cycle analysis of novel lightweight composite processes: Reducing the environmental footprint of automotive structures," *Journal of Cleaner Production*, vol. 330, p. 129808, Jan. 2022, publisher: Elsevier BV. [Online]. Available: https://linkinghub.elsevier.com/retrieve/pii/S0959652621039834

[2] B. Iacopo, M. Chiara, S. Michela, and V. Tommaso, "Life cycle analyses of a composite towbar realized via filament winding and comparison with traditional metallic alternatives," *Sustainable Materials and Technologies*, vol. 40, p. e00980, Jul. 2024, publisher: Elsevier BV. [Online]. Available: https://linkinghub.elsevier.com/retrieve/pii/S221499372400160X

[3] C. Mignanelli, I. Bianchi, A. Forcellese, and M. Simoncini, "Life cycle assessment of pressure vessels realized with thermoplastic and thermosetting matrix composites," *Int J Adv Manuf Technol*, vol. 135, no. 9-10, pp. 4491–4509, Dec. 2024, publisher: Springer Science and Business Media LLC. [Online]. Available: https://link.springer.com/10.1007/s00170-024-14742-x

[4] C. Maware, R. Muvunzi, T. Machingura, and I. Daniyan, "Examining the Progress in Additive Manufacturing in Supporting Lean, Green and Sustainable Manufacturing: A Systematic Review," *Applied Sciences*, vol. 14, no. 14, p. 6041, Jul. 2024, publisher: MDPI AG. [Online]. Available: https://www.mdpi.com/2076-3417/14/14/6041

[5] A. Prathyusha and G. Raghu Babu, "A review on additive manufacturing and topology optimization process for weight reduction studies in various industrial applications," *Materials Today: Proceedings*, vol. 62, pp. 109–117, 2022, publisher: Elsevier BV. [Online]. Available: https://linkinghub.elsevier.com/retrieve/pii/S2214785322010525

[6] M. Nirish and R. Rajendra, "Suitability of metal additive manufacturing processes for part topology optimization – A comparative study," *Materials Today: Proceedings*, vol. 27, pp. 1601–1607, 2020, publisher: Elsevier BV. [Online]. Available: https://linkinghub.elsevier.com/retrieve/pii/S2214785320320551

[7] B. C. Hauck, B. R. Ruprecht, and P. C. Riley, "Accurate and on-demand chemical sensors: A print-in-place ion mobility spectrometer," *Sensors and Actuators B:*

Chemical, vol. 362, p. 131791, Jul. 2022, publisher: Elsevier BV. [Online]. Available: https://linkinghub.elsevier.com/retrieve/pii/S0925400522004336

[8] G. Stano, S. M. A. I. Ovy, J. R. Edwards, M. Cianchetti, G. Percoco, and Y. Tadesse, "One-shot additive manufacturing of robotic finger with embedded sensing and actuation," *Int J Adv Manuf Technol*, vol. 124, no. 1-2, pp. 467–485, Jan. 2023, publisher: Springer Science and Business Media LLC. [Online]. Available: https://link.springer.com/10.1007/s00170-022-10556-x

[9] F. M. Mwema and E. T. Akinlabi, "Basics of Fused Deposition Modelling (FDM)," in *Fused Deposition Modeling: Strategies for Quality Enhancement*. Springer International Publishing, 2020, pp. 1–15.

[10] P. Wang, B. Zou, S. Ding, C. Huang, Z. Shi, Y. Ma, and P. Yao, "Preparation of short CF/GF reinforced PEEK composite filaments and their comprehensive properties evaluation for FDM-3D printing," *Composites Part B: Engineering*, vol. 198, p. 108175, Oct. 2020. [Online]. Available: https://linkinghub.elsevier.com/retrieve/pii/S1359836820306818

[11] X. Han, D. Yang, C. Yang, S. Spintzyk, L. Scheideler, P. Li, D. Li, J. Geis-Gerstorfer, and F. Rupp, "Carbon Fiber Reinforced PEEK Composites Based on 3D-Printing Technology for Orthopedic and Dental Applications," *JCM*, vol. 8, no. 2, p. 240, Feb. 2019. [Online]. Available: https://www.mdpi.com/2077-0383/8/2/240

[12] J. Pierre, M. Verville, G. Chenier, R. D. Farahani, N. Piccirelli, M. Lévesque, and D. Therriault, "Non-planar material-extrusion additive manufacturing of multifunctional sandwich structures using carbon-reinforced polyetheretherketone (PEEK)," *Additive Manufacturing*, vol. 84, p. 104124, Mar. 2024. [Online]. Available: https://linkinghub.elsevier.com/retrieve/pii/S2214860424001702

[13] D. Arslan, M. Mihai, D. Therriault, and M. Lévesque, "Formulation and characterization of polyetherimide composites reinforced with recycled carbon fibers and thermal black particles for fused filament fabrication," *Composites Part A: Applied Science and Manufacturing*, vol. 194, p. 108946, Jul. 2025. [Online]. Available: https://linkinghub.elsevier.com/retrieve/pii/S1359835X25002404

[14] Y. Abderrafai, A. Diouf-Lewis, F. Sosa-Rey, R. D. Farahani, N. Piccirelli, M. Lévesque, and D. Therriault, "Additive manufacturing and characterization of high temperature thermoplastic blends for potential aerospace applications,"

Composites Science and Technology, vol. 231, p. 109839, Jan. 2023. [Online]. Available: https://linkinghub.elsevier.com/retrieve/pii/S0266353822005814

[15] X. Ao, S. Lin, J. Liu, H. Xia, and J. Meng, "Modeling and self-supporting printing simulation of fuse filament fabrication," *Sci Rep*, vol. 14, no. 1, p. 16275, Jul. 2024. [Online]. Available: https://www.nature.com/articles/s41598-024-67200-9

[16] M. Fernandez-Vicente, M. Canyada, and A. Conejero, "Identifying limitations for design for manufacturing with desktop FFF 3D printers," *International Journal of Rapid Manufacturing*, 2015.

[17] D. Arslan, M. Mihai, D. Therriault, and M. Lévesque, "Flexural properties of sandwich panels fabricated by filament-extrusion of high-temperature thermoplastic composites," *Composites Science and Technology*, vol. 263, p. 111106, Apr. 2025. [Online]. Available: https://linkinghub.elsevier.com/retrieve/pii/S0266353825000740

[18] S. M. F. Kabir, K. Mathur, and A.-F. M. Seyam, "A critical review on 3D printed continuous fiber-reinforced composites: History, mechanism, materials and properties," *Composite Structures*, vol. 232, p. 111476, Jan. 2020. [Online]. Available: https://linkinghub.elsevier.com/retrieve/pii/S0263822319322706

[19] P. Zhuo, S. Li, I. A. Ashcroft, and A. I. Jones, "Material extrusion additive manufacturing of continuous fibre reinforced polymer matrix composites: A review and outlook," *Composites Part B: Engineering*, vol. 224, p. 109143, Nov. 2021. [Online]. Available: https://linkinghub.elsevier.com/retrieve/pii/S1359836821005266

[20] Y. Tao, P. Li, J. Zhang, S. Wang, S. Q. Shi, and F. Kong, "A review of fused filament fabrication of continuous natural fiber reinforced thermoplastic composites: Techniques and materials," *Polymer Composites*, p. pc.27477, Jun. 2023. [Online]. Available: https://4spepublications.onlinelibrary.wiley.com/doi/10.1002/pc.27477

[21] P. Cheng, Y. Peng, S. Li, Y. Rao, A. Le Duigou, K. Wang, and S. Ahzi, "3D printed continuous fiber reinforced composite lightweight structures: A review and outlook," *Composites Part B: Engineering*, vol. 250, p. 110450, Feb. 2023, publisher: Elsevier BV. [Online]. Available: https://linkinghub.elsevier.com/retrieve/pii/S135983682200823X

[22] A. Uşun and R. Gümrük, "The mechanical performance of the 3D printed composites produced with continuous carbon fiber reinforced filaments obtained via melt impregnation," *Additive Manufacturing*, vol. 46, p. 102112, Oct. 2021. [Online]. Available: https://linkinghub.elsevier.com/retrieve/pii/S2214860421002773

[23] Q. Hu, Y. Duan, H. Zhang, D. Liu, B. Yan, and F. Peng, "Manufacturing and 3D printing of continuous carbon fiber prepreg filament," *Journal of Materials Science*, vol. 53, no. 3, pp. 1887–1898, Feb. 2018. [Online]. Available: http://link.springer.com/10.1007/s10853-017-1624-2

[24] Z. Ouyang, L. Yang, Z. Pi, Z. Wang, C. Yan, and Y. Shi, "Robot-assisted laser additive manufacturing for high-strength/low-porosity continuous fiber-reinforced thermoplastic composites," *Composites Science and Technology*, vol. 247, p. 110397, Mar. 2024. [Online]. Available: https://linkinghub.elsevier.com/retrieve/pii/S0266353823004918

[25] Y. Zhuang, "Preparation of pre-impregnated continuous carbon fiber reinforced nylon6 filaments and the mechanical properties of 3D printed composites," *Materials Today Communications*, 2023.

[26] J.-N. Dai, "High-content continuous carbon fibers reinforced PEEK matrix composite with ultra-high mechanical and wear performance at elevated temperature," *Composite Structures*, 2022.

[27] Y. Wu, K. Wang, V. Neto, Y. Peng, R. Valente, and S. Ahzi, "Interfacial behaviors of continuous carbon fiber reinforced polymers manufactured by fused filament fabrication: A review and prospect," *International Journal of Material Forming*, vol. 15, no. 3, p. 18, May 2022. [Online]. Available: https://link.springer.com/10.1007/s12289-022-01667-7

[28] F. Wang, G. Wang, F. Ning, and Z. Zhang, "Fiber–matrix impregnation behavior during additive manufacturing of continuous carbon fiber reinforced polylactic acid composites," *Additive Manufacturing*, vol. 37, p. 101661, Jan. 2021. [Online]. Available: https://linkinghub.elsevier.com/retrieve/pii/S2214860420310332

[29] T. Liu, X. Tian, Y. Zhang, Y. Cao, and D. Li, "High-pressure interfacial impregnation by micro-screw in-situ extrusion for 3D printed continuous carbon fiber reinforced nylon composites," *Composites Part A: Applied Science and Manufacturing*, vol. 130, p. 105770, Mar. 2020. [Online]. Available: https://linkinghub.elsevier.com/retrieve/pii/S1359835X20300087

[30] M. Luo, X. Tian, J. Shang, W. Zhu, D. Li, and Y. Qin, "Impregnation and interlayer bonding behaviours of 3D-printed continuous carbon-fiber-reinforced poly-ether-ether-ketone composites," *Composites Part A: Applied Science and Manufacturing*, vol. 121, pp. 130–138, Jun. 2019. [Online]. Available: https://linkinghub.elsevier.com/retrieve/pii/S1359835X19300995

[31] E. H. Saidane, G. Arnold, P. Louis, and M.-J. Pac, "3D printed continuous glass fibre-reinforced polyamide composites: Fabrication and mechanical characterisation," *Journal of Reinforced Plastics and Composites*, vol. 41, no. 7-8, pp. 284–295, Apr. 2022. [Online]. Available: http://journals.sagepub.com/doi/10.1177/07316844211051746

[32] L. Blok, M. Longana, H. Yu, and B. Woods, "An investigation into 3D printing of fibre reinforced thermoplastic composites," *Additive Manufacturing*, vol. 22, pp. 176–186, Aug. 2018. [Online]. Available: https://linkinghub.elsevier.com/retrieve/pii/S2214860417305687

[33] Markforged, "Continuous carbon fiber - high strength 3d printing material," 2025. [Online]. Available: https://markforged.com/materials/continuous-fibers/continuous-carbon-fiber

[34] S. Terekhina, S. Egorov, T. Tarasova, I. Skornyakov, L. Guillaumat, and M. Hattali, "In-nozzle impregnation of continuous textile flax fiber/polyamide 6 composite during FFF process," *Composites Part A: Applied Science and Manufacturing*, vol. 153, p. 106725, Feb. 2022. [Online]. Available: https://linkinghub.elsevier.com/retrieve/pii/S1359835X21004401

[35] Y. An, J. H. Myung, J. Yoon, and W.-R. Yu, "Three-dimensional printing of continuous carbon fiber-reinforced polymer composites via in-situ pin-assisted melt impregnation," *Additive Manufacturing*, vol. 55, p. 102860, Jul. 2022. [Online]. Available: https://linkinghub.elsevier.com/retrieve/pii/S2214860422002597

[36] R. Matsuzaki, M. Ueda, M. Namiki, T.-K. Jeong, H. Asahara, K. Horiguchi, T. Nakamura, A. Todoroki, and Y. Hirano, "Three-dimensional printing of continuous-fiber composites by in-nozzle impregnation," *Scientific Reports*, vol. 6, no. 1, p. 23058, Mar. 2016, number: 1. [Online]. Available: https://www.nature.com/articles/srep23058

[37] H. Zhang, Z. Zhou, X. Gao, T. Fan, Y. Chen, and H. Wang, "Enhanced mechanical performance of fused filament fabrication copolyester by continuous carbon fiber in-situ reinforcement," *Journal of Applied Polymer Science*, vol. 140, no. 2, Jan. 2023. [Online]. Available: https://onlinelibrary.wiley.com/doi/10.1002/app.53296

[38] J. Hartwich, S. Slawski, and S. Duda, "Specific Strength and Modulus of Epoxy Composites with Different Reinforcing Materials," in *Lecture Notes in Networks and Systems*, vol. 1146 LNNS, Gliwice, Poland, 2025, pp. 81 – 88, iSSN: 23673370. [Online]. Available: http://dx.doi.org/10.1007/978-3-031-73161-7_8

[39] I. M. Daniel and O. Ishai, *Engineering mechanics of composite materials*, 2nd ed. New York: Oxford University Press, 2006, oCLC: ocm57285865.

[40] D. Hull and T. W. Clyne, *An introduction to composite materials*, 2nd ed., ser. Cambridge solid state science series. Cambridge: Cambridge Univ. Press, 2007.

[41] N. J. Pagano, *Exact Moduli of Anisotropic Laminates*. Dordrecht: Springer Netherlands, 1994, pp. 210–231. [Online]. Available: https://doi.org/10.1007/978-94-017-2233-9_18

[42] H. L. Cox, "The elasticity and strength of paper and other fibrous materials," *Br. J. Appl. Phys.*, vol. 3, no. 3, pp. 72–79, Mar. 1952. [Online]. Available: https://iopscience.iop.org/article/10.1088/0508-3443/3/3/302

[43] J. Yan, E. Demirci, and A. Gleadall, "Are classical fibre composite models appropriate for material extrusion additive manufacturing? A thorough evaluation of analytical models," *Additive Manufacturing*, vol. 62, p. 103371, Jan. 2023. [Online]. Available: https://linkinghub.elsevier.com/retrieve/pii/S2214860422007606

[44] T. Mori and K. Tanaka, "Average stress in matrix and average elastic energy of materials with misfitting inclusions," *Acta Metallurgica*, vol. 21, no. 5, pp. 571–574, 1973. [Online]. Available: https://www.sciencedirect.com/science/article/pii/0001616073900643

[45] J.-F. Chauvette, I. L. Hia, J. Pierre, G. Chenier, R. D. Farahani, N. Piccirelli, and D. Therriault, "Non-planar multiprocess additive manufacturing of multifunctional composites," *Advanced Materials Technologies*, vol. 8, no. 17, p. 2300399, 2023. [Online]. Available: https://advanced.onlinelibrary.wiley.com/doi/abs/10.1002/admt.202300399

[46] J.-F. Chauvette, "Non-planar multinozzle additive manufacturing of thermoset composite microscaffold networks," *Composites Part B*, 2023.

[47] Y. Liétard, "Exploiting Geometric Frustration in Coupled von Mises Trusses to Program Multifunctional Mechanical Metamaterials," *Adv. Eng. Mater.*, 2025.

[48] W. Abd-Elaziem, S. Elkatatny, A.-E. Abd-Elaziem, M. Khedr, M. A. Abd El-baky, M. A. Hassan, M. Abu-Okail, M. Mohammed, A. Järvenpää, T. Allam, and A. Hamada, "On the current research progress of metallic materials fabricated by laser powder bed fusion process: a review," *Journal of Materials Research and*

Technology, vol. 20, pp. 681–707, Sep. 2022, publisher: Elsevier BV. [Online]. Available: https://linkinghub.elsevier.com/retrieve/pii/S2238785422011243

[49] S. Singh, V. S. Sharma, and A. Sachdeva, "Progress in selective laser sintering using metallic powders: A review," *Materials Science and Technology*, vol. 32, no. 8, pp. 760–772, May 2016, publisher: SAGE Publications. [Online]. Available: https://journals.sagepub.com/doi/10.1179/1743284715Y.0000000136

[50] T. A. M. Sghaier, H. Sahlaoui, T. Mabrouki, H. Sallem, and J. Rech, "Selective Laser Melting of Stainless-Steel: A Review of Process, Microstructure, Mechanical Properties and Post-Processing treatments," *Int J Mater Form*, vol. 16, no. 4, Jul. 2023, publisher: Springer Science and Business Media LLC. [Online]. Available: https://link.springer.com/10.1007/s12289-023-01769-w

[51] Y. Song, Y. Ghafari, A. Asefnejad, and D. Toghraie, "An overview of selective laser sintering 3D printing technology for biomedical and sports device applications: Processes, materials, and applications," *Optics & Laser Technology*, vol. 171, p. 110459, Apr. 2024, publisher: Elsevier BV. [Online]. Available: https://linkinghub.elsevier.com/retrieve/pii/S003039922301352X

[52] 3DSPRO, "Aluminum 6061 3dspro," 2025. [Online]. Available: https://3dspro.com/3d-printing-materials/metal/aluminum/aluminum-6061

[53] R. Ummethala, P. S. Karamched, S. Rathinavelu, N. Singh, A. Aggarwal, K. Sun, E. Ivanov, L. Kollo, I. Okulov, J. Eckert, and K. Prashanth, "Selective laser melting of high-strength, low-modulus ti–35nb–7zr–5ta alloy," *Materialia*, vol. 14, p. 100941, 2020. [Online]. Available: https://linkinghub.elsevier.com/retrieve/pii/S2589152920303574

[54] W. E. King, A. T. Anderson, R. M. Ferencz, N. E. Hodge, C. Kamath, S. A. Khairallah, and A. M. Rubenchik, "Laser powder bed fusion additive manufacturing of metals; physics, computational, and materials challenges," *Applied Physics Reviews*, vol. 2, no. 4, p. 041304, Dec. 2015, publisher: AIP Publishing. [Online]. Available: https://pubs.aip.org/aip/apr/article/123813

[55] Forgelabs. (2025) Topology Optimization: Algorithmically generated parts. [Online]. Available: https://forgelabs.com/topology-optimization/

[56] J. Jacob, D. Pejak Simunec, A. E. Z. Kandjani, A. Trinchi, and A. Sola, "A Review of Fused Filament Fabrication of Metal Parts (Metal FFF): Current Developments and

Future Challenges," *Technologies*, vol. 12, no. 12, p. 267, Dec. 2024, publisher: MDPI AG. [Online]. Available: https://www.mdpi.com/2227-7080/12/12/267

[57] T. Alkindi, M. Alyammahi, R. A. Susantyoko, and S. Atatreh, "The effect of varying specimens' printing angles to the bed surface on the tensile strength of 3D-printed 17-4PH stainless-steels via metal FFF additive manufacturing," *MRS Communications*, vol. 11, no. 3, pp. 310–316, Jun. 2021, publisher: Springer Science and Business Media LLC. [Online]. Available: https://link.springer.com/10.1557/s43579-021-00040-0

[58] F. Léonard and S. Tammas-Williams, "Metal FFF sintering shrinkage rate measurements by X-ray computed tomography," *Nondestructive Testing and Evaluation*, vol. 37, no. 5, pp. 631–644, Sep. 2022, publisher: Informa UK Limited. [Online]. Available: https://www.tandfonline.com/doi/full/10.1080/10589759.2022.2085702

[59] B. Ray, B. Oskolkov, C. Liu, Z. Leblanc, and W. Tian, "FFF-based metal and ceramic additive manufacturing: Production scale-up from a stream of variation analysis perspective," *Manufacturing Letters*, vol. 35, pp. 811–821, Aug. 2023, publisher: Elsevier BV. [Online]. Available: https://linkinghub.elsevier.com/retrieve/pii/S2213846323001876

[60] I. Buj-Corral, F. Fenollosa-Artés, and J. Minguella-Canela, "Three-Dimensional Printing of Metallic Parts by Means of Fused Filament Fabrication (FFF)," *Metals*, vol. 14, no. 11, p. 1291, Nov. 2024, publisher: MDPI AG. [Online]. Available: https://www.mdpi.com/2075-4701/14/11/1291

[61] X. Kan, D. Yang, Z. Zhao, and J. Sun, "316L FFF binder development and debinding optimization," *Mater. Res. Express*, vol. 8, no. 11, p. 116515, Nov. 2021, publisher: IOP Publishing. [Online]. Available: https://iopscience.iop.org/article/10.1088/2053-1591/ac3b15

[62] Facfox. (2025) Comprehensive Guide to FDM 3D Printing with Metal Filaments - FacFox Docs. [Online]. Available: https://facfox.com/docs/kb/comprehensive-guide-to-fdm-3d-printing-with-metal

[63] C. Yan, L. Hao, L. Xu, and Y. Shi, "Preparation, characterisation and processing of carbon fibre/polyamide-12 composites for selective laser sintering," *Composites Science and Technology*, vol. 71, no. 16, pp. 1834–1841, Nov. 2011, publisher: Elsevier BV. [Online]. Available: https://linkinghub.elsevier.com/retrieve/pii/S0266353811003034

[64] T. Czelusniak and F. L. Amorim, "Influence of energy density on selective laser sintering of carbon fiber-reinforced PA12," *Int J Adv Manuf Technol*, vol. 111, no. 7-8, pp. 2361–2376, Dec. 2020, publisher: Springer Science and Business Media LLC. [Online]. Available: https://link.springer.com/10.1007/s00170-020-06261-2

[65] S. Zhang, H. Tang, D. Tang, T. Liu, and W. Liao, "Effect of fabrication process on the microstructure and mechanical performance of carbon fiber reinforced PEEK composites via selective laser sintering," *Composites Science and Technology*, vol. 246, p. 110396, Feb. 2024, publisher: Elsevier BV. [Online]. Available: https://linkinghub.elsevier.com/retrieve/pii/S0266353823004906

[66] 3DXTech, "CARBONX PEI 9085+CF," 2025. [Online]. Available: https://www.3dxtech.com/products/pei-cf15

[67] Forgelabs. (2025) Forge Labs | Selective Laser Sintering 3D Printing Services. [Online]. Available: https://forgelabs.ca/selective-laser-sintering-sls/

[68] M. Raths, "Gradual error detection technique for non-destructive assessment of density and tensile strength in fused filament fabrication processes," *The International Journal of Advanced Manufacturing Technology*, 2024.

[69] Bambu Lab, "CPAHT-CF Bambu Lab," 2025. [Online]. Available: https://ca.store.bambulab.com/products/paht-cf

[70] K. Saeed, A. McIlhagger, E. Harkin-Jones, C. McGarrigle, D. Dixon, M. Ali Shar, A. McMillan, and E. Archer, "Characterization of continuous carbon fibre reinforced 3D printed polymer composites with varying fibre volume fractions," *Composite Structures*, vol. 282, p. 115033, Feb. 2022. [Online]. Available: https://linkinghub.elsevier.com/retrieve/pii/S0263822321014549

[71] P. Pokorný, D. R. Delgado Sobrino, Václav, J. Petru, and R. Gołębski, "Research into Specific Mechanical Properties of Composites Produced by 3D-Printing Additive Continuous-Fiber Fabrication Technology," *Materials*, vol. 16, no. 4, p. 1459, Feb. 2023. [Online]. Available: https://www.mdpi.com/1996-1944/16/4/1459

[72] J. Justo, L. Távara, L. García-Guzmán, and F. París, "Characterization of 3D printed long fibre reinforced composites," *Composite Structures*, vol. 185, pp. 537–548, Feb. 2018. [Online]. Available: https://linkinghub.elsevier.com/retrieve/pii/S0263822317321529

[73] E. Polyzos, A. Katalagarianakis, D. Van Hemelrijck, and L. Pyl, "Delamination analysis of 3D-printed nylon reinforced with continuous carbon fibers," *Additive Manufacturing*, vol. 46, p. 102144, Oct. 2021. [Online]. Available: https://linkinghub.elsevier.com/retrieve/pii/S2214860421003080

[74] F. Lupone, E. Padovano, C. Venezia, and C. Badini, "Experimental Characterization and Modeling of 3D Printed Continuous Carbon Fibers Composites with Different Fiber Orientation Produced by FFF Process," *Polymers*, vol. 14, no. 3, p. 426, Jan. 2022, number: 3. [Online]. Available: https://www.mdpi.com/2073-4360/14/3/426

[75] S. Wang, X. Yan, B. Chang, J. Zhang, S. Liu, F. Liu, J. Shang, L.-H. Shao, S. Yin, W. Zhang, Y. Zhu, and X. Ding, "A review on modeling strategies in understanding the process mechanism of 3D printed continuous fiber-reinforced thermoplastic composites," *Journal of Manufacturing Processes*, vol. 145, pp. 46–70, Jul. 2025. [Online]. Available: https://linkinghub.elsevier.com/retrieve/pii/S1526612525003974

[76] J. Hares, P. A. Kelly, and M. A. Battley, "IN-SITU MIXING AND PRINTING OF CONTINUOUS CARBON FIBRE REINFORCED THERMOSET COMPOSITES."

[77] J. Kipping and T. Schüppstuhl, "Load-Oriented Nonplanar Additive Manufacturing Method for Optimized Continuous Carbon Fiber Parts," *Materials*, vol. 16, no. 3, p. 998, Jan. 2023, number: 3. [Online]. Available: https://www.mdpi.com/1996-1944/16/3/998

[78] S. Olcun and R. Kempers, "Thermal Characterization of Continuous Pitch Carbon Fiber 3D-Printed using a 6-Axis Robot Arm," in *2022 21st IEEE Intersociety Conference on Thermal and Thermomechanical Phenomena in Electronic Systems (iTherm)*. San Diego, CA, USA: IEEE, May 2022, pp. 1–6. [Online]. Available: https://ieeexplore.ieee.org/document/9899510/

[79] G. Zhang, Y. Wang, W. Qiu, K. Dong, and Y. Xiong, "Geometric characteristics of single bead fabricated by continuous fiber reinforced polymer composite additive manufacturing," *Materials Today: Proceedings*, vol. 70, pp. 431–437, 2022. [Online]. Available: https://linkinghub.elsevier.com/retrieve/pii/S2214785322061776

[80] N. Li, Y. Li, and S. Liu, "Rapid prototyping of continuous carbon fiber reinforced polylactic acid composites by 3D printing," *Journal of Materials Processing Technology*, vol. 238, pp. 218–225, Dec. 2016. [Online]. Available: https://linkinghub.elsevier.com/retrieve/pii/S0924013616302515

[81] S. Kuschmitz, A. Schirp, J. Busse, H. Watschke, C. Schirp, and T. Vietor, "Development and Processing of Continuous Flax and Carbon Fiber-Reinforced Thermoplastic Composites by a Modified Material Extrusion Process," *Materials*, vol. 14, no. 9, p. 2332, Apr. 2021. [Online]. Available: https://www.mdpi.com/1996-1944/14/9/2332

[82] W. Ye, H. Dou, J. Liu, Z. Li, Y. Cheng, D. Zhang, F. Yang, and S. Jing, "Additive manufacture of programmable multi-matrix continuous carbon fiber reinforced gradient composites," *Additive Manufacturing*, vol. 89, p. 104255, Jun. 2024. [Online]. Available: https://linkinghub.elsevier.com/retrieve/pii/S2214860424003014

[83] W. Ye, H. Dou, D. Zhang, F. Yang, Y. Cheng, and W. Cai, "Effects of process parameters on mechanical properties and interface of 3D printed bamboo-inspired CCFR-PLA / TPU composites," *Polymer Composites*, vol. 45, no. 1, pp. 227–242, Jan. 2024. [Online]. Available: https://4spepublications.onlinelibrary.wiley.com/doi/10.1002/pc.27770

[84] Anisoprint. (2025) Desktop Anisoprinting | Anisoprint. [Online]. Available: https://anisoprint.com/solutions/desktop/

[85] Y. Chen, "Preparation of CCF/PEEK filaments together with property evaluation for additive manufacturing," *Composite Structures*, 2022.

[86] A. Uşun, B. B. Vatandaş, and R. Gümrük, "Enhanced mechanical properties of continuous carbon fiber reinforced polyether-ether-ketone composites via infrared preheating and high fiber volume fraction," *Additive Manufacturing*, vol. 89, p. 104289, Jun. 2024. [Online]. Available: https://linkinghub.elsevier.com/retrieve/pii/S221486042400335X

[87] P.-A. Arrighi, "Anisoprint Composer A4 review: A unique carbon fiber 3D printer," 2022. [Online]. Available: https://www.aniwaa.com/review/3d-printers/review-anisoprint-composer-a4-continuous-fiber-3d-printing/

[88] Markforged, "Industrial 3D Printers: Strong Parts. Right Now | Markforged," 2025. [Online]. Available: https://markforged.com/3d-printers

[89] C. Composites, "CF3D - Continuous Composites," 2025. [Online]. Available: https://continuouscomposites.com/cf3d/

[90] S. Sieberer, M. Winklberger, C. Savandaiah, C. Kralovec, and M. Schagerl, "Experimental strength and fracture analysis of additively manufactured continuous carbon fibre reinforced lugs with load-tailored fibre placement," *Procedia Structural Integrity*, vol. 42, pp. 72–79, 2022. [Online]. Available: https://linkinghub.elsevier.com/retrieve/pii/S2452321622005650

[91] P. Gregorio, "Developing a Custom Printhead Controller to Print Large-Scale Parts Using Industrial Motion Systems," Master's thesis, Polytechnique Montréal, 2022.

[92] G. Zhang, Y. Wang, Z. Chen, X. Xu, K. Dong, and Y. Xiong, "Robot-assisted conformal additive manufacturing for continuous fibre-reinforced grid-stiffened shell structures," *Virtual and Physical Prototyping*, vol. 18, no. 1, p. e2203695, Dec. 2023. [Online]. Available: https://www.tandfonline.com/doi/full/10.1080/17452759.2023.2203695

[93] G. Fang, T. Zhang, Y. Huang, Z. Zhang, K. Masania, and C. C. L. Wang, "Exceptional Mechanical Performance by Spatial Printing with Continuous Fiber: Curved Slicing, Toolpath Generation and Physical Verification," Jan. 2024, arXiv:2311.17265 [cs]. [Online]. Available: http://arxiv.org/abs/2311.17265

[94] B. Barış Vatandaş, A. Uşun, N. Yıldız, C. Şimşek, Necati Cora, M. Aslan, and R. Gümrük, "Additive manufacturing of PEEK-based continuous fiber reinforced thermoplastic composites with high mechanical properties," *Composites Part A: Applied Science and Manufacturing*, vol. 167, p. 107434, Apr. 2023. [Online]. Available: https://linkinghub.elsevier.com/retrieve/pii/S1359835X23000106

[95] A. N. Dickson, J. N. Barry, K. A. McDonnell, and D. P. Dowling, "Fabrication of continuous carbon, glass and Kevlar fibre reinforced polymer composites using additive manufacturing," *Additive Manufacturing*, vol. 16, pp. 146–152, Aug. 2017. [Online]. Available: https://linkinghub.elsevier.com/retrieve/pii/S2214860416301889

[96] R. Guerra Silva, E. Gonzalez, A. Inostroza, and G. Morales Pavez, "Flexural Analysis of Additively Manufactured Continuous Fiber-Reinforced Honeycomb Sandwich Structures," *JMMP*, vol. 8, no. 5, p. 226, Oct. 2024.

[97] R. Guerra Silva, G. Morales Pavez, and L. F. Caminos, "Reliability challenges in additive manufacturing of continuous fiber-reinforced sandwich structures," *Manufacturing Letters*, vol. 45, pp. 112–115, Sep. 2025.

[98] X. Li, P. Qu, H. Kong, Y. Lei, A. Guo, S. Wang, Y. Wan, and J. Takahashi, "Enhanced mechanical properties of sandwich panels via integrated 3D printing of continuous fiber face sheet and TPMS core," *Thin-Walled Structures*, vol. 204, p. 112312, Nov. 2024.

[99] Z. Zhang, Y. Long, Z. Yang, K. Fu, and Y. Li, "An investigation into printing pressure of 3D printed continuous carbon fiber reinforced composites," *Composites Part A: Applied Science and Manufacturing*, vol. 162, p. 107162, Nov. 2022. [Online]. Available: https://linkinghub.elsevier.com/retrieve/pii/S1359835X2200344X

[100] L. Yang, D. Zheng, G. Jin, and G. Yang, "Fabrication and Formability of Continuous Carbon Fiber Reinforced Resin Matrix Composites Using Additive Manufacturing," *Crystals*, 2022.

[101] Bambulab, "PLA-CF bambu lab," 2025. [Online]. Available: https://ca.store.bambulab.com/products/pla-cf

[102] F. Sosa-Rey, Y. Abderrafai, A. Diouf Lewis, D. Therriault, N. Piccirelli, and M. Lévesque, "OpenFiberSeg: Open-source segmentation of individual fibers and porosity in tomographic scans of additively manufactured short fiber reinforced composites," *Composites Science and Technology*, vol. 226, p. 109497, Jul. 2022, publisher: Elsevier BV. [Online]. Available: https://linkinghub.elsevier.com/retrieve/pii/S0266353822002391

[103] D30 Committee, "Test Method for Tensile Properties of Polymer Matrix Composite Materials," 2024. [Online]. Available: http://www.astm.org/cgi-bin/resolver.cgi?D3039D3039M-17

[104] D20 Committee, "Test Method for Tensile Properties of Plastics," 2024. [Online]. Available: http://www.astm.org/cgi-bin/resolver.cgi?D638-14

[105] Y. Tao, F. Kong, Z. Li, J. Zhang, X. Zhao, Q. Yin, D. Xing, and P. Li, "A review on voids of 3D printed parts by fused filament fabrication," *Journal of Materials Research and Technology*, vol. 15, pp. 4860–4879, Nov. 2021. [Online]. Available: https://linkinghub.elsevier.com/retrieve/pii/S2238785421012448

[106] S. Sidlipura, A. Ayadi, and M. L. Deléglise, "Assessing Intra-Bundle Impregnation in Partially Impregnated Glass Fiber-Reinforced Polypropylene Composites Using a 2D Extended-Field and Multimodal Imaging Approach," *Polymers*, 2024.

[107] Bambulab, "PLA basic bambu lab," 2025. [Online]. Available: https://ca.store.bambulab.com/products/pla-basic-filament

[108] JLC3DP, "316l stainless steel," 2025. [Online]. Available: https://jlc3dp.com/help/article/316L-Stainless-Steel

[109] N. Maqsood and M. Rimašauskas, "Development and fabrication of continuous carbon fiber reinforced thermoplastic porous composite structures with different infill patterns by using additive manufacturing," *Journal of Thermoplastic Composite Materials*, vol. 36, no. 5, pp. 2050–2075, May 2023, number: 5. [Online]. Available: http://journals.sagepub.com/doi/10.1177/08927057221088468

[110] N. Li, G. Link, J. Jelonnek, M. V. Morais, and F. Henning, "Microwave additive manufacturing of continuous carbon fibers reinforced thermoplastic composites: Characterization, analysis, and properties," *Additive Manufacturing*, vol. 44, p. 102035, Aug. 2021. [Online]. Available: https://linkinghub.elsevier.com/retrieve/pii/S2214860421002001

[111] Z.-M. Huang, W.-J. Guo, H.-B. Huang, and C.-C. Zhang, "Tensile Strength Prediction of Short Fiber Reinforced Composites," *Materials*, vol. 14, no. 11, p. 2708, May 2021. [Online]. Available: https://www.mdpi.com/1996-1944/14/11/2708

[112] F. Sosa-Rey, C. Vella, A. Lingua, J. Pierre, N. Piccirelli, D. Therriault, and M. Lévesque, "Multiscale Fast Fourier Transform homogenization of additively manufactured fiber reinforced composites from component-wise description of morphology," *Composites Science and Technology*, vol. 243, p. 110261, Oct. 2023. [Online]. Available: https://linkinghub.elsevier.com/retrieve/pii/S026635382300355X

APPENDIX A CO-EXTRUSION G-CODE POST-PROCESSOR

Figure A.1a presents the GUI used to select a G-code file to modify. The user can first validate the printing path interpreted from the g-code using the 3D viewer, then choose the different user inputs to tune how the g-code is modified. The g-code is then saved, and the new g-code instructions are presented, with new features of interest highlighted (e.g., cutting instructions, layer changes). Figure A.1b shows the modified g-code 3D viewer embedded in a HyperText Markup Language (HTML) output file. It is used to visually validate the modifications before sending the program to a machine, and helps identify the source of various issues encountered.

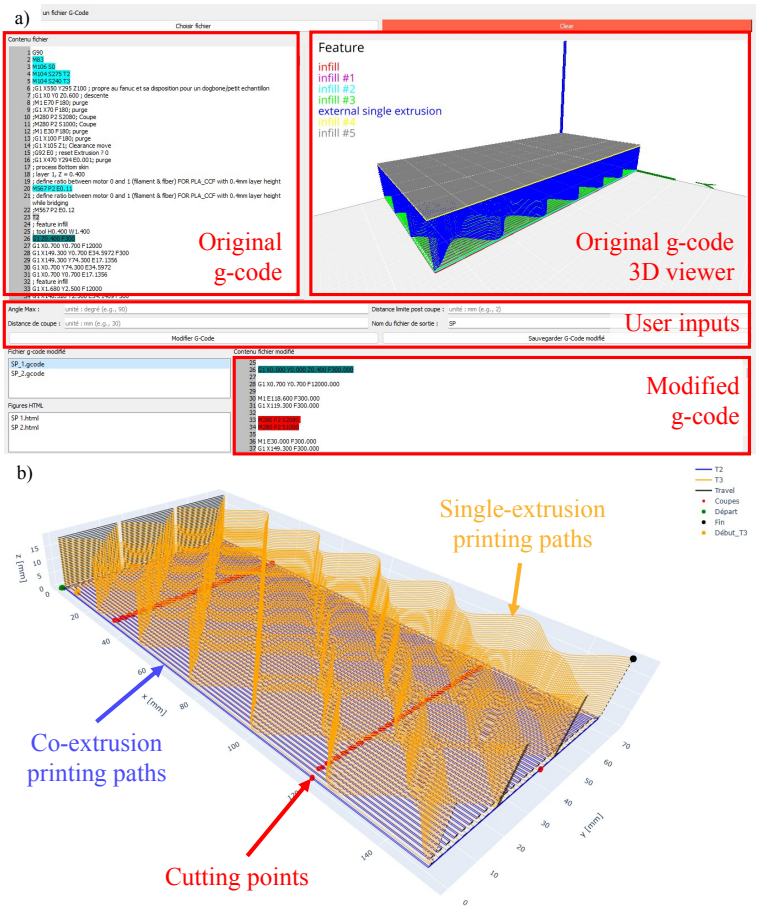

Figure A.1 **GUI of the co-extrusion g-code post processor.** a) GUI window featuring the original g-code text and 3D viewer, user inputs and modified g-code text. b) 3D viewer of the modified G-code.

Figure A.2a presents a typical FFF g-code snippet with the corresponding printing path. The G1 instructions are used as a single line combining the extrusion (E value), the XYZ movement and the feedrate (F value). Figure A.2b shows the corresponding interpreted coordinates and printing path, stored as a matrix that is easily modified.

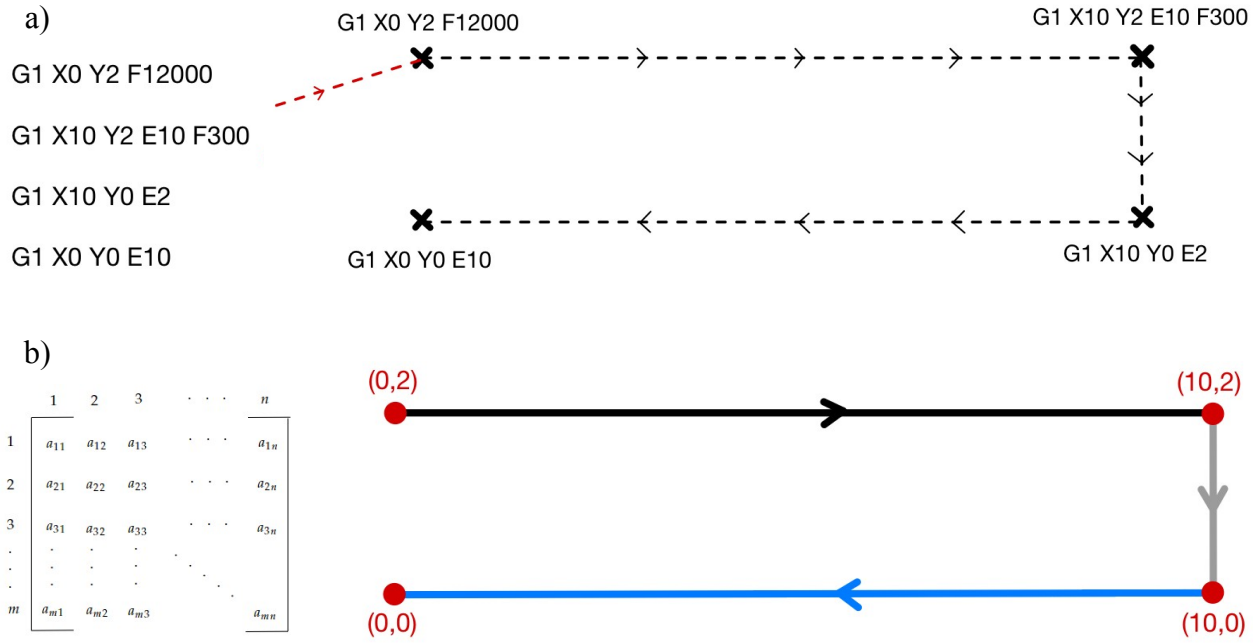

Figure A.2 **Post-processor g-code reading.** a) Original g-code instructions with corresponding printing path visual representation. b) G-code interpretation as a matrix with corresponding printing path coordinates

Figure A.3a presents the interpreted continuous printing path with various identified sections. First, a minimum angle is identified, which results in the labelling of the corresponding point as an endpoint. A new point at which the cutting instructions will be required is then added by travelling upstream on the printing path. The distance travelled corresponds to the cutting distance. Figure A.3b then shows the validation made for the following segments (i.e. between the new endpoint and the next point triggering the minimum angle condition). Since it is shorter than the post-cut limit distance, the segment is considered too short to be printed using continuous fiber reinforcements and is converted to a travel movement instead. The same algorithm is then applied to the new point, triggering the minimum angle condition. Since the previous segment is a travel movement, no cut is required. The following path, being longer than the post-cut limit distance, is kept as a new extruded segment. Figure A.3c presents the resulting discontinuous modified printing path. The first section was segmented into two individual segments separated by the newly added cutting point. The smaller segment was replaced by a travel movement, and the second longer section is left untouched.

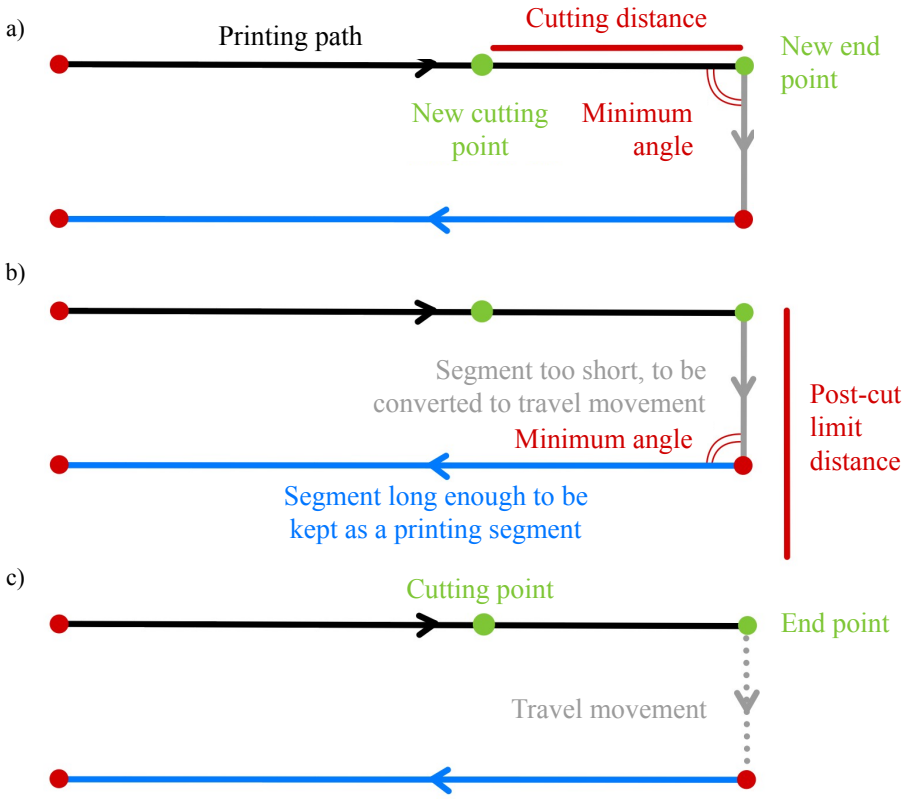

Figure A.3 **Post-processor printing path modification.** a) Original continuous printing path with identification of a new cutting point to be added. b) Validation of the limit distance for printable paths. c) Resulting discontinuous printing path with a travel movement

Figure A.4 shows the modified printing path with the different sections identified from #1 to #5. It then presents the corresponding modified G-code instructions to be written in the new G-code file. Segments #1 and #3 correspond to the original first printed segment that was cut in the middle. The new co-extrusion g-code structure features M1 instructions used to indicate the adjusted E value and the associated F value. This line will be sent from the robot controller to the printhead controller. The new G1 instructions are modified to include only the XYZ coordinates and the required feedrate that will be interpreted by the robot simulation software and converted into a *Karel* program in a later step.

The point #2 corresponds to the cutting point added to separate sections #1 and #3. The added M280 instructions indicate the sequence of two servomotor angular positions required to cut the fibers. Segment #4 corresponds to the segment shorter than the post-cut limit distance, and is therefore converted to a travel movement, corresponding to a G1 instruction following the new structure without a related M1 instruction. Segment #5 corresponds to the last segment that was not modified, but was rewritten using the new co-extrusion g-code

structure.

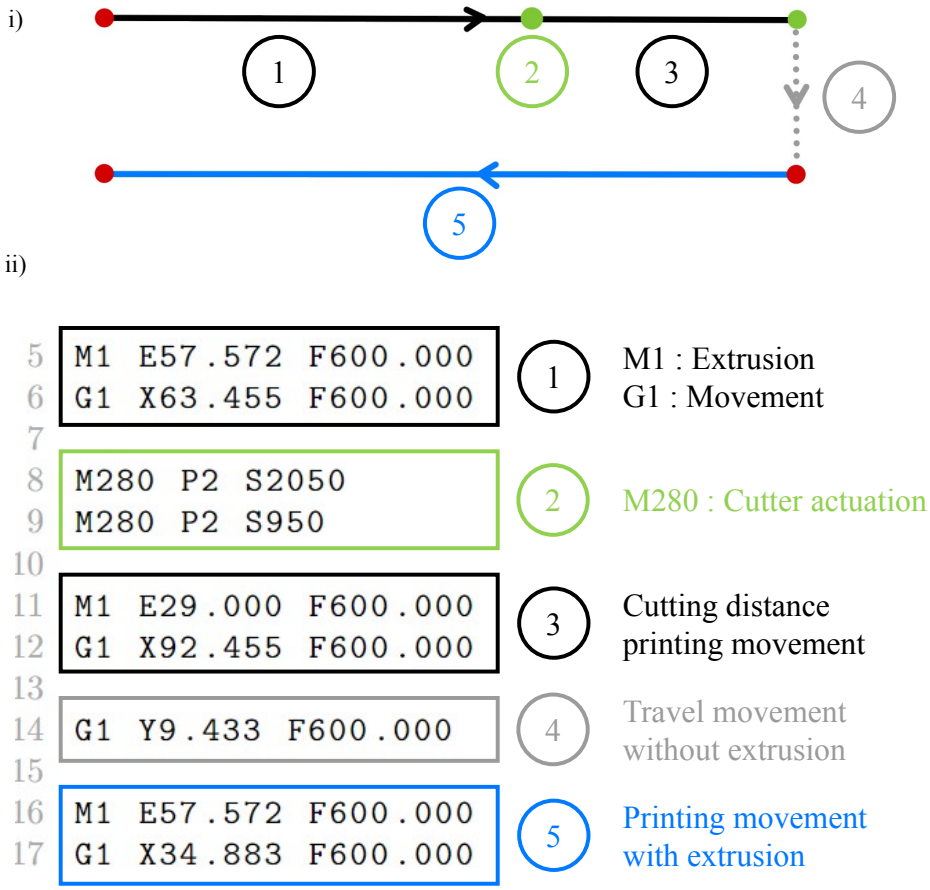

Figure A.4 **Post-processor modified g-code writing.** i) Modified discontinuous printing path with each section identified. ii) Corresponding modified g-code instructions for co-extrusion CFRP-AM